TECHNISCHE UNIVERSITÄT MÜNCHEN

Lehrstuhl für Numerische Mechanik

Micromechanical Continuum Approach for the Analysis of Biopolymer Networks

Christian J. Cyron

Vollständiger Abdruck der von der Fakultät für Maschinenwesen der Technischen Universität München zur Erlangung des akademischen Grades eines

Doktor-Ingenieurs (Dr.-Ing.)

genehmigten Dissertation.

Vorsitzender: Univ.-Prof. Dr. rer. nat. Oliver Lieleg

Prüfer der Dissertation:

1. Univ.-Prof. Dr.-Ing. Wolfgang A. Wall
2. Univ.-Prof. Dr. rer. nat. Andreas R. Bausch
3. Prof. Ignacio Romero Olleros, Ph. D.
   Universidad Politécnica de Madrid / Spanien

Die Dissertation wurde am 10. Oktober 2011 bei der Technischen Universität München eingereicht und durch die Fakultät für Maschinenwesen am 16. Dezember 2011 angenommen.

Acknowledgement

Obviously, it is impossible to express in written words the gratitude I feel for so many having helped and supported me in my work and my life, be they advisors, colleagues, friends or members of my family. But I know that all those who helped me most have a good heart. Remembering Antoine de Saint-Exupéry's sentence 'on ne voit bien qu'avec le cœur', I therefore just put here an empty page knowing that they will see their names anyway.

Munich, September 1st, 2011 Christian J. Cyron

Abstract

A detailed understanding of biopolymer networks can be considered a corner stone for future developments in many fields of modern science and engineering ranging from biophysics and biochemistry to bioengineering, biomedical engineering and material science. The small length scale and high complexity of such networks significantly hamper the application of traditional theoretical and experimental methods. As a consequence, computer simulations have attracted increasing interest in this field over the last years. As molecular dynamics simulations are often too expensive and macromechanical continuum models are not detailed enough, the development of a sufficiently detailed and at the same time efficient micromechanical simulation model has become a major target in biosciences.

In this thesis, a new micromechanical computer model for biopolymer networks is developed on the basis of continuum mechanics. Biopolymer networks consist of three essential components: filaments, crosslinker molecules connecting them by chemical bonds, and a viscous fluid into which filaments and crosslinker molecules are embedded. These three components are modeled as continua, respectively. Most attention is payed thereby to the filaments whose mechanics is generally assumed to dominate the mechanics of biopolymer networks. In opposition to that, only coarse models are employed for fluid and crosslinker molecules. On the level of single filaments, the laws of statistical mechanics have significant impact to the equations of motion. In so far proposed micromechanical models, e.g., those based on bead-spring discretizations, this is accounted for only in a purely heuristic manner. In opposition to that, in this thesis filament dynamics is discretized in a stringent mathematical way starting from first principles of Newtonian and statistical mechanics. This approach is not only theoretically more consistent and more general than previous ones, but resolves at the same time a series of numerical deficiencies of traditional models enabling an efficiency gain of approximately two orders of magnitude.

In a variety of examples, excellent agreement between the computer model developed in this thesis, experimental results, and theoretical predictions is shown for simulations of both single filaments and complete biopolymer networks. Especially, the numerical model's capacity to reproduce the viscoelastic moduli of biopolymer networks on biologically relevant length and time scales is demonstrated. Furthermore, the effect of different physical properties of crosslinker molecules on the structural polymorphism of biopolymer networks is examined. To this end, a computational study is performed which reveals for the first time the prerequisites for the formation of clusters in biopolymer networks. Such clusters have already been observed experimentally, but not yet explained theoretically.

The model developed in this thesis is the first one allowing for a micromechanical investigation into the viscoelasticity and structural polymorphism of biopolymer networks on the biologically especially relevant length scale $1\mu m - 10\mu m$ and time scale $10s - 10^3s$ at an acceptable computational cost. This gives rise to the hope that it will be a valuable tool for biophysicists, bioengineers and biomedical engineers dealing with the mechanics of cells and tissue as well as for material scientists working on the development of new bioinspired materials.

Zusammenfassung

Ein umfassendes Verständnis biopolymerer Netzwerke kann als wesentliche Grundlage für zahlreiche zukünftige wissenschaftliche und technische Entwicklungen angesehen werden, insbesondere in der Biophysik, der Biochemie, der Biotechnik, der Medizintechnik und den Materialwissenschaften. Die kleine Längenskala und hohe Komplexität solcher Netzwerke beschränken die Anwendbarkeit klassischer experimenteller und theoretischer Methoden, sodass jüngstens numerische Simulationen in diesem Gebiet rasch an Bedeutung gewonnen haben.

Da molekulardynamische Simulationen oft zu teuer sind, makromechanische Kontinuumsmodelle jedoch nicht detailliert genug, kommt der Entwicklung eines hinreichend detaillierten und gleichzeitig effizienten mikromechanischen Simulationsmodells entscheidende Bedeutung zu.

In dieser Dissertation wird ein neues mikromechanisches Computermodell für biopolymere Netzwerke auf der Basis nichtlinearer Kontinuumsmechanik entwickelt, bei dem diese Netzwerke in drei wesentliche Bestandteile unterteilt werden: Filamente, Vernetzungsmoleküle, die diese Filamente untereinander verbinden, sowie ein viskoses Fluid, in das Filamente und Vernetzungsmoleküle eingebettet sind. Alle drei werden als Kontinua modelliert, wobei die Filamente aufgrund ihrer großen Bedeutung für die Netzwerkmechanik am ausführlichsten abgehandelt werden, während für Fluid und Vernetzungsmoleküle grobe Modelle als ausreichend angesehen werden. Die Bewegungsgleichungen der Filamente werden in entscheidendem Maße von den Gesetzen der statistischen Mechanik geprägt. Klassische Polymermodelle wie z.B. das Kugel-Feder-Modell erfassen diese nur rein heuristisch. Im Gegensatz dazu wird in der vorliegenden Dissertation aus den grundlegenden Prinzipien der klassischen und statistischen Mechanik in stringenter mathematischer Weise ein Finite-Elemente-Modell abgeleitet. Dieser neuartige Ansatz unterscheidet sich von bisherigen nicht nur durch seine theoretische Konsistenz und Allgemeinheit, sondern löst gleichzeitg auch eine Reihe numerischer Probleme und verbessert die Effizient der Simulationen damit um etwa zwei Größenordnungen.

In zahlreichen Beispielen wird eine hervorragende Übereinstimmung zwischen dem in dieser Dissertation entwickelten Computermodell, Experimenten und theoretischen Vorhersagen sowohl für einzelne Filamente als auch ganze Netzwerke gezeigt. Insbesondere wird die Fähigkeit des Computermodells demonstriert, die viskoelastischen Module biopolymerer Netzwerke auf biologisch relevanten Längen- und Zeitskalen zu reproduzieren. Darüber hinaus werden die Auswirkungen verschiedener physikalischer Eigenschaften der Vernetzungsmoleküle auf die strukturelle Polymorphie der Netzwerke untersucht. Anhand einer Parameterstudie werden dabei erstmals die Voraussetzungen für die Entstehung von Clustern in biopolymeren Netzwerken zeigt. Solche Cluster wurden bislang zwar experimentell beobachtet, die theoretischen Grundlagen ihres Entstehens jedoch waren nicht bekannt.

Das in dieser Dissertation entwickelte Modell erlaubt erstmals mit der momentan verfügbaren Rechenkapazität die rechnergestützte mikromechanische Untersuchung der Viskoelastizität und strukturellen Polymorphie biopolymerer Netzwerke auf der biologisch besonders relevanten Längenskala $1\mu m - 10\mu m$ und Zeitskala $10s - 10^3 s$. Es besteht daher Grund zur Hoffnung, dass es sich in Zukunft als wertvolles Werkzeug für Biophysiker, Bioingenieure und Medizintechniker erweisen wird, deren Arbeiten in Zusammenhang stehen mit der Mechanik biologischer Zellen oder biologischen Gewebes, sowie für Materialwissenschaftler, die an der Entwicklung neuer Werkstoffe nach dem Vorbild der belebten Natur arbeiten.

Contents

Nomenclature

Mathematical Notation, Symbols & Quantities

$[\cdot]_a$	value of function under condition a
$[\cdot]_a^b$	difference between function evaluated at a and b
$[a; b]$	closed interval between a and b
$\langle . \rangle$	mean value
$\times$	cross product
$\otimes$	tensor product
$(.)^{\otimes 2}$	tensor product $(.) \otimes (.)$
$\boldsymbol{x}'(\xi, t)$	derivative with respect to curve parameter ξ
$\dot{\boldsymbol{x}}(\xi, t)$	derivative with respect to time t
$\frac{\partial \boldsymbol{x}}{\partial \xi}$	partial derivative of $\boldsymbol{x}$ with respct to ξ
$\delta(.)$	variation of $(.)$
$\delta_a(.)$	additive variation of $(.)$
δ_{xy}	Dirac-δ-function with argument $x - y$
$\chi^{i(k)}$	characteristic function defined in Eq. (3.47)
$\mathbf{1}$	identity matrix
a	some scalar value/ absolute value of vector $\boldsymbol{a}$
$\boldsymbol{a}$	vector- or matrix-valued quantity
a_i	i-th component of vector $\boldsymbol{a}$
$\boldsymbol{a}_i$	i-th column of matrix $\boldsymbol{a}$
$\boldsymbol{e}_i$	i-th cartesian basis vector of $\mathbb{R}^m$
H_2	second Hermite polynomial
$P_{3/2}$	parabolic cylinder function
$\boldsymbol{R}(\boldsymbol{\theta})$	rotation matrix corresponding to rotation vector $\boldsymbol{\theta}$
$\boldsymbol{S}(\boldsymbol{\theta})$	spin matrix corresponding to rotation vector $\boldsymbol{\theta}$
$SO(m)$	Special Orthogonal Group in m dimensions
$\boldsymbol{T}(\boldsymbol{\theta})$	inverse exponential map of $\boldsymbol{\theta}$
$\mathcal{W}$	multidimensional standard Wiener process
$\hat{\mathcal{W}}$	approximated multidimensional standard Wiener process
$\mathcal{Z}(a, b)$	vector of Gaussian random numbers with mean a and standard deviation b

General Indices & Symbols

$\Delta(.)$	(a) change of $(.)$ in one time step, (b) uncertainty or tolerance of physical parameter $(.)$ (c) $\Delta\xi$: discretization length of white noise

$\Delta_{A \to B}(.)$	change of $(.)$ by transition from A to B
$\Delta_{t_D}(.)$	change of $(.)$ over span on time t_D
$(.)_{\parallel}$	quantity or component of $(.)$ parallel to rod tangent
$(.)_{\perp}$	quantity or component of $(.)$ perpendicular to rod tangent
$(.)_{IP}$	evaluated at or related to numerical integration point IP
$(.)_c$	quantity $(.)$ evaluated at the center of rod or particle
$(.)_{cl}$	referring to a linker
$(.)_{exp}$	result from experiment
$(.)_{fil}$	referring to a filament
$(.)_{loc}$	quantity in local coordinate system defined by material frame of rod
$(.)_{off}$	referring to chemical unbinding
$(.)_{on}$	referring to chemical binding
$(.)_r$	quantity related to rotational degrees of freedom
$(.)_{sim}$	result from simulation
$(.)_t$	quantity related to translational degrees of freedom
$(.)^0$	quantity at point in time $t = 0$
$(.)^i$	quantity at point in time t^i
$(.)^{\{j\}}$	quantity in j-th iteration step
$(.)^{[k]}$	component or quantity related to node $\xi^{[k]}$

Friction and Diffusion

γ	friction coefficient of rod or particle per unit length
ζ	friction coefficient for whole rod or particle
η	viscosity of fluid
$\boldsymbol{\omega}$	rotation velocity field of fluid
D	diffusion coefficient
T	temperature of fluid
$\boldsymbol{c}$	damping matrix
k_B	Boltzmann constant
$\boldsymbol{s}$	result of damping matrix decomposition $\boldsymbol{s}\boldsymbol{s}^T = \boldsymbol{c}$
$\boldsymbol{v}$	translation velocity field of fluid

Rod-like continuum

$\boldsymbol{\theta}(\xi, t)$	rotation of cross section of continuum
$\boldsymbol{\kappa}$	curvature
ν	Poisson ratio
ξ	curve parameter of continuum
A	cross section
A_i	cross section with shear correction for i-th principal axis
E	Young's modulus
G	shear modulus

J_i	moment of inertia of area with respect to i-th principal axis
J_r	polar moment of inertia of area
L	total curve length of continuum
R	end-to-end distance
d	diameter of circular rod-like continuum
$\boldsymbol{k}$	constitutive matrix
m	number of dimensions
t	point in time
t_{max}	end point of simulation time
$\boldsymbol{x}(\xi, t)$	position vector of continuum
$\boldsymbol{f}_{bd}$	boundary force on rod at $\xi = 0$ or $\xi = L$
$\boldsymbol{f}_{el}$	spatial derivative of section force
$\boldsymbol{f}_{ext}$	deterministic external force per unit length
$\boldsymbol{f}_{PTC}$	virtual damping force for PTC
$\boldsymbol{f}_{s}$	section force
$\boldsymbol{f}_{stoch}$	stochastic force per unit length
$\bar{\boldsymbol{f}}_{stoch}$	resulting stochastic force on whole rod
$\boldsymbol{f}_{visc}$	damping force per unit length
$\boldsymbol{m}_{bd}$	boundary moment on rod at $\xi = 0$ or $\xi = L$
$\boldsymbol{m}_{el}$	spatial derivative of section moment
$\boldsymbol{m}_{ext}$	deterministic external moment per unit length
$\boldsymbol{m}_{PTC}$	virtual damping moment for PTC
$\boldsymbol{m}_{s}$	section moment
$\boldsymbol{m}_{stoch}$	stochastic moment per unit length
$\bar{\boldsymbol{m}}_{stoch}$	resulting stochastic moment on whole rod
$\boldsymbol{m}_{visc}$	damping moment per unit length

Polymer physics

ϑ	tangent correlation function
ρ_{fil}	filament concentration (total length of all filaments per volume)
τ_{bend}	time constant of filament's slowest bending mode
ϕ	angle between two filaments
F	normalized mean-square difference of end-to-end distance
G^{*}	viscoelastic storage modulus
G^{**}	viscoelastic loss modulus
L_p	persistence length
$L_{p,eff}$	effective persistence length
n_{cl}	number of linker molecules in simulation volume
$\boldsymbol{u}$	deformation field imposed to boundary of polymer network
$\mathcal{G}$	radial distribution function (RDF)
$\mathcal{M}$	subfunction in RDF
$\mathcal{N}$	normalization factor for RDF

Chemical reactions

$[.]$	molar concentration.
F	species of free binding domains on filaments
G	free energy
L	species of linkers with at least one free binding domain
LF	species of linker bound to filament binding domain
V_{react}	reaction volume of filament binding site
h_{bind}	distance between adjacent binding sites on filaments
k	second order rate constant
k_{react}	rate constant for linker in reaction volume of filament binding site
p	probability of chemical reaction

Discretization, Numerics & Simulation

$\boldsymbol{\Theta}$	rotational nodal values
λ_{PTC}	exponent for decrease of PTC damping
ψ	dihedral angle
$\xi^{[k]}$	k-th node in spatial discretization
τ_D	dihedral torsion
τ_{FS}	torsion of Frenet-Serret frame
$\tau_{stretch}$	time constant of fastest stretching mode in discretization
$\boldsymbol{C}$	discrete damping matrix
$\boldsymbol{K}_{PTC}$	contribution of PTC to total stiffness matrix
$\boldsymbol{I}$	interpolation function matrix
$\boldsymbol{W}$	weighting function matrix
$\boldsymbol{X}$	positional nodal values
c_{PTC}	scalar numerical damping factor for PTC normalized by time step size
$\hat{c}_{PTC}$	scalar numerical damping factor for PTC
e_d	displacement error
h	discretization length in space
i	index for points in time
i_{max}	number of discrete points in time greater than zero
k	index for nodes in space
k_{max}	number of nodes for discretization in space
n_{ele}	number of finite elements in spatial discretization
n_{real}	number of realizations used for computation of statistical quantities
n_{sample}	number of sample points used for computation of statistical quantities
t_{CPU}	CPU time required for simulation
w	weight of quadrature point
$\mathcal{R}^{\{j\}}$	residual in j-th iteration step

Abbreviations

BD	Brownian Dynamics
beam-I	finite beam element type I according to classification in [77]
beam-II	finite beam element type II according to classification in [77]
bp	Base Pairs
CPU	Central Processing Unit
DNA	Deoxyribonucleic Acid
FEM	Finite Element Method
HMM	Heavy meromyosin
MD	Molecular Dynamics
MM	Molecular Mechanics
MSD	Mean-square difference
NURBS	Non-Uniform Rational B-Splines
PTC	Pseudo-Transient Continuation
RDF	Radial Distribution Function
SDE	Stochastic Differential Equation
SPDE	Stochastic Partial Differential Equation
TMV	Tobacco Mosaic Virus

1 Introduction

1.1 Motivation

The mechanics of biological tissue is on both cellular and subcellular scale largely determined by the mechanics of biopolymer networks: on cellular scale, the cohesion between cells is made sure by the extracellular matrix, which is a biopolymer network consisting to a large extent of collagen fibers. On subcellular scale, the cytoskeleton, another biopolymer network mainly consisting of actin filaments, microtubules, and intermediate filaments, plays a crucial role for a variety of processes such as cell division, cell motility and mechanotransduction.

As a consequence, the mechanics of biopolymer networks has recently attracted rapidly increasing interest especially among biophysicists, bioengineers, biomedical engineers, mechanical engineers and material scientists. The great complexity and small length scale of these networks poses a great challenge for both experimental and theoretical investigation, which has given rise to the development of a variety of computational methods and models in this field. These can be divided into two main categories as illustrated in Fig. 1.1: macromechanical and micromechanical models.

In the first category, biopolymer networks are considered as macroscopic continua [76]. Their microstructure such as filament arrangement and interconnection is typically accounted for only by means of suitable nonlinear constitutive laws. By this first approach, large systems can be simulated at a low computational cost, however, at the prize that the simulation does not deliver detailed insights into processes on small length scales. This information has rather to be fed into the simulation algorithms in advance. As in life sciences simulations are often desired to provide information about exactly the very small length scales where experiments are especially difficult or even impossible, more detailed models are often required.

Hence micromechanical models resolving the network down to the level of single filaments have been developed. They can be divided into those neglecting and those accounting for the stochastic thermal forces to which filaments are subject according to the laws of statistical mechanics. If stochastic thermal forces are neglected, filaments can be simulated on the basis of deterministic Newtonian mechanics in a quasi-static [44, 49, 74] or dynamic [1] way. Obviously, this approach can give insight into some basic mechanical properties of fibrous networks. However, neglecting completely thermodynamics, it cannot model a series of biologically highly relevant processes such as the interplay between mechanics and biochemistry or the dynamic structural reorganisation in biopolymer networks, happening for example in the formation of lamellipodia in cells.

Only models grasping the statistical mechanics of biopolymer networks can capture features like these. Among such models, one can distinguish between those accounting only for the equilibrium thermodynamics of networks and those addressing also non-equilibrium effects. In the first case it is sufficient capturing some way the probability of all network configurations

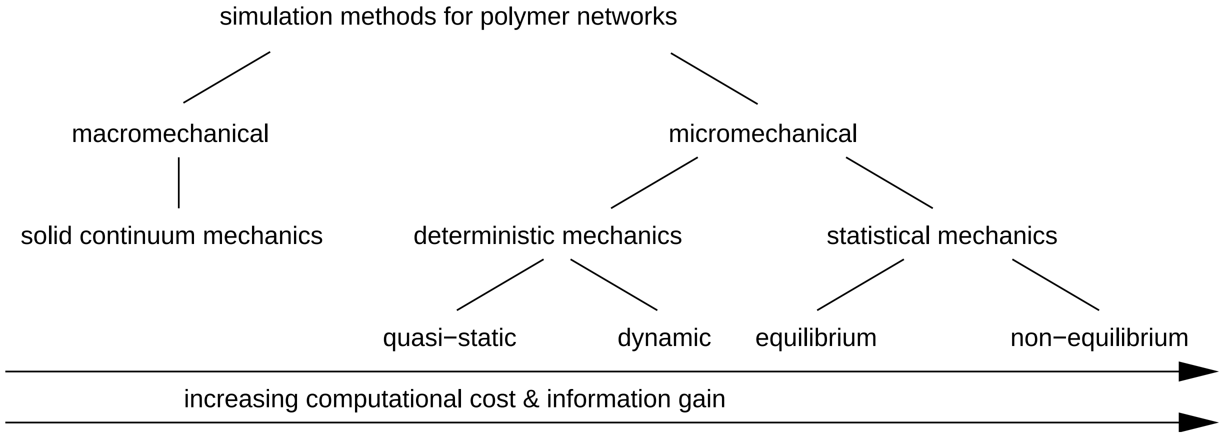

Figure 1.1: Taxonomy of methods for the simulation of biopolymer networks: from left to right the computational cost is increasing, but also the information, which can be gained by the respective computational technique.

correctly as it is done for example in Metropolis-Monte-Carlo models [7]. Transition processes and probabilities between these configurations, however, are not considered. In the second case, also the dynamical evolution of networks is captured. To this end, one typically employs methods based on the theory of Brownian dynamics and different kinds of filament discretizations such as bead-spring models [54, 55], rods-on-string-models [14] or worm-like-chain segment models [48]. Only micromechanical models including the statistical mechanics of biopolymer networks are detailed enough to answer a series of key questions in biophysics and bioengineering, such as the question which parameters govern the structural polymorphism of biopolymer networks, i.e., their self-organization into a variety of different network architectures. On the other hand, the computational cost of such models often renders studies of biopolymer networks on the desired length and time scales impossible.

Thus, this thesis is devoted to the development of a new method for the micromechanical computer simulation of biopolymer networks including the effects of statistical mechanics with a vastly increased efficiency as compared to state-of-the-art methods.

1.2 Overview

The thesis is organized as follows: in section 2, a micromechanical model of biopolymer networks based on the concepts of continuum mechanics is introduced. To this end, the networks are divided into three principal constituents: filaments, crosslinker molecules and fluid. It is pointed out that often a detailed model of the fluid is not required. Therefore detailed numerical models are developed only for the filaments in section 3, the crosslinker molecules in section 4 and their interactions in section 5. In section 6, a series of examples demonstrates the excellent agreement between these models, experimental data and theoretical predictions. Finally, in section 7 the main results of this thesis are summed up and a brief outlook is given how they can be exploited in various field of science and engineering. Parts of this thesis are taken from, derived from or also published in the articles [26, 28, 29, 30].

2 Micromechanical Continuum Model of Biopolymer Networks

Biopolymer networks are formed by three main constituents: polymer filaments, crosslinker molecules (referred to also as ’linkers’ in the following) which connect these filaments by transient chemical bonds, and a background fluid into which filaments and linkers are embedded. In Fig. 2.1, some examples of biopolymer networks consisting of actin filaments with different types and concentrations of crosslinker molecules are presented. In the pictures only the filaments are clearly visible. The background fluid is typically an aqueous solution and therefore nearly transparent. The size of the linkers on the other hand ranges on the nanometer scale so that they cannot be seen on the images in Fig. 2.1 which depict a sector of some microns edge length, respectively. The variety of completely different network architectures which can be formed by one and the same kind of filament just by the application of different linkers is remarkable.

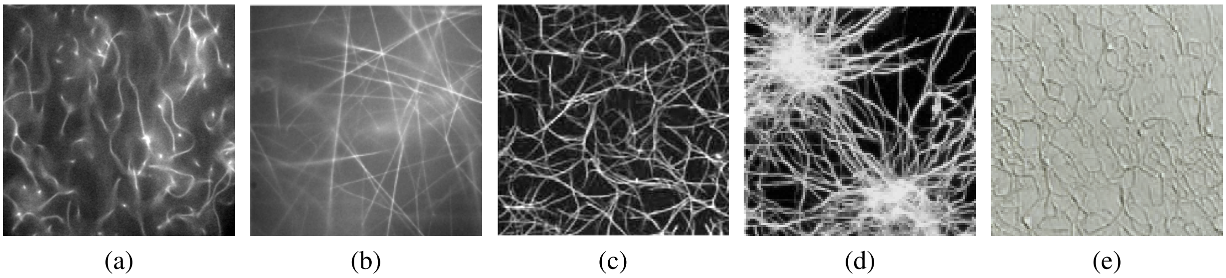
(a) (b) (c) (d) (e)

Figure 2.1: Examples for biopolymer networks in vitro: (a) network of entangled actin filaments [6], (b) actin-fascin bundle network[1], (c) actin-filamin bundle network [6], (d) actin cluster network[2], (e) actin layer[3]

The first important question is how to model the three main constituents of biopolymer networks in view of their small size. It is well-known that the behaviour of atoms as well as of any system constituted by atoms can be predicted in an accurate manner by the application of the laws of quantum mechanics to the complete system. However, the tremendous complexity of the resulting equations renders it impossible to pursue that strategy when trying to simulate systems consisting of more than just some dozens of atoms. To overcome that problem, one often resorts to molecular dynamics (MD) simulations, where effects of quantum physics are not considered explicitly, and single atoms or small packages of atoms are the smallest units. These are modeled on the basis of Newtonian mechanics, and their equations of motion typically account for potentials due to bonds between neighbouring units, non-bonded potentials as well as

---

[1] Reprinted Fig. with permission from [64]. ©2007 by the American Physical Society

[2] Reprinted Fig. with permission from [66]. ©2009 by the Royal Society of Chemistry

[3] From [94]. Reprinted with permission from AAAS.

potentials originating from coulombic forces. Although MD models are much more efficient than quantum mechanical simulations, even an MD simulation of a minor biopolymer network on a time scale relevant for cell and tissue mechanics would by far exceed the computational resources available at the moment. On the other hand, the mechanics of biopolymer networks is primarily governed by deformations on the length scale of single filaments, which are typically some micrometers long. On this length scale, it is well-known from microfluidics as well as experimental polymer physics that continuum models already apply. Linkers are typically much smaller than filaments so that modeling them accurately by similar techniques may be more difficult. However, for reasons discussed below also for linkers a continuum model is expected to be sufficient when focussing on the mechanics of whole networks rather than of single linkers. The coarse-graining step from MD models to continuum models goes along with a vast reduction of the computational cost enabling simulations even of complete biopolymer networks. Yet the essential information about micromechanical processes in the network on the level of single filaments is still kept. Thus, such a micromechanical continuum approach provides an excellent trade-off between computational cost and information gain and will be developed in detail in the following sections 2.1, 2.2 and 2.3.

2.1 Fluid

From microfluidics it is well-known that a continuum model based on the Navier-Stokes equations is suitable for fluid volumes down to the micrometer length scale relevant for biopolymer networks. Modeling the fluid in these networks, one is confronted with two major difficulties: first, on the length scale of biopolymers stochastic thermal fluctuations according to the laws of statistical mechanics affect the fluid velocity field perceptibly; second, the fluid dynamics is affected by complex fluid-structure interactions with all the filaments and linkers in the network. These two effects can be accounted for in detail only at a considerable computational cost. Therefore various simplifications are common in polymer physics (cf. [32, 43, 54, 55]): Due to the small length scale, low velocities and high viscosities, Reynolds and Mach numbers are usually small in biopolymer networks. Therefore a linearized version of the incompressible Navier-Stokes equations can be applied [43] so that the fluid velocity field can be separated into a deterministic part and a stochastic part owing to the thermal fluctuations. Because of the very small diameter and total volume fraction of filaments and linkers in the whole network (e.g., in a $4\mu M$ actin network filament diameter is $5nm$ and volume fraction 6.5%), the effect of the filament and linker motion on the deterministic part of the fluid velocity field is small. Therefore the deterministic part of the fluid velocity field is computed initially on the basis of the boundary conditions of the simulation volume only, and the drag forces and moments on filaments and linkers due to their relative motion compared to this velocity field are captured by simple friction coefficients assuming a Newtonian fluid. The stochastic part of the fluid velocity field has then never to be computed explicitly, because it causes no effective drag, but only a stochastic excitation independent on fluid, filament and linker motion. This excitation, however, can be computed immediately from the friction coefficients of filaments and linkers according to the fluctuation-dissipation theorem [32]. In general, the deterministic part of the fluid velocity field can be computed by standard methods such as the finite element or finite volume method. In practice, not even this may be necessary as often it is either zero or a simple shear flow which can be calculated analytically without any discretization. Therefore the treatment of the fluid velocity field will not be discussed in any more detail below, and it will rather be assumed to be given.

More sophisticated models for the fluid including the fluid-structure interactions in one or another way may be an interesting avenue of future research. These may either be based on a simple consideration of the Navier-Stokes equations' characteristics similar to the Oseen- or Rotne-Prager tensors well-known in polymer physics [33, 79] or on more sophisticated ideas such as presented in [15].

2.2 Filaments

Force transmission in biopolymer networks is usually assumed to occur predominatly via the filaments. These are rod-like structures typically longer than $100nm$ with a slenderness ratio typically between 10 and far above 1000. From a variety of experiments (e.g. [37, 68, 90, 92]) it is well-known that not only the fluid on that length scale can be modeled as a mechanical continuum, but that also rod-like structures such as biopolymers can be considered as mechanical continua with axial, bending and torsion stiffness so that classical beam theories such as the one of Euler and Bernoulli can be employed [46]. Thus the dynamics of filaments has not to be modeled on the basis of quantum mechanics or molecular dynamics (MD), but rather a coarse grained continuum model can be used instead of an atomistic or molecular one as illustrated in Fig. 2.2.

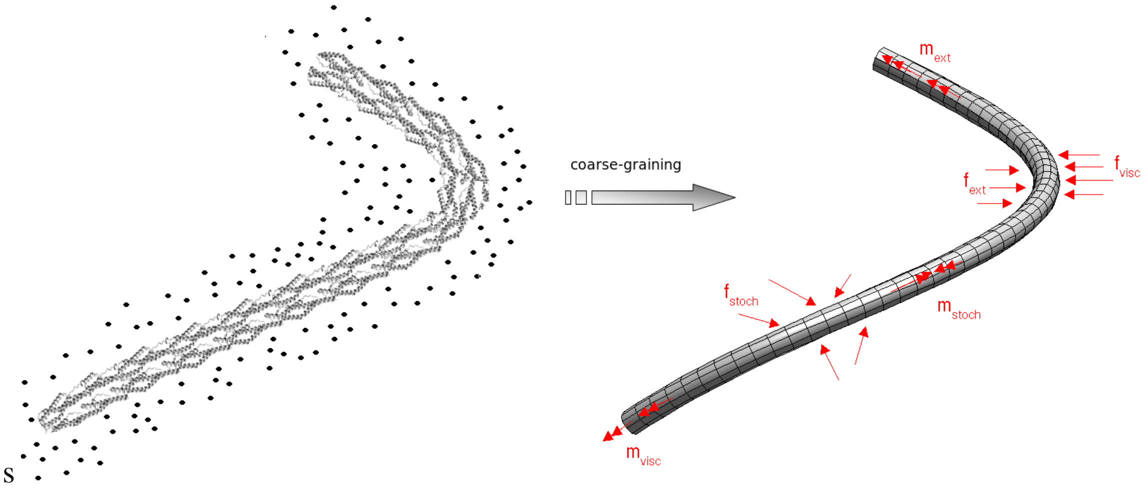

Figure 2.2: Whereas in MD simulations of a filament embedded into a fluid single atoms or small packages of atoms are simulated (left), coarse-graining allows for modeling the filament as a continuum whose interactions with its surroundings are modeled by stochastic, viscous and determnistic external loads (right).[4]

Employing a continuum model, the equation of motion of a filament, i.e. its balance of linear and angular momentum, comprises the following quantities.

---

[4] Reprinted Fig. with permission from [30]. ©2012 by John Wiley & Sons, Ltd.

First, viscous forces $\boldsymbol{f}_{visc}$ and moments $\boldsymbol{m}_{visc}$ account for the damping the filament experiences moving through the fluid. It is underlined that in the model developed in the following only such external friction is considered and not any kind of internal friction in the filaments as discussed in [31]. In polymer physics, such internal friction is typically assumed to play only a minor role, and if necessary it can be added to the approach developed below by only some minor modifications.

Second, stochastic forces $\boldsymbol{f}_{stoch}$ and moments $\boldsymbol{m}_{stoch}$ capture the stochastic excitation of the filament by the thermal fluctuations in the fluid. They are related to the viscous forces and moments by the fluctuation-dissipation theorem as already mentioned in section 2.1 and discussed in more detail below.

Third, miscellaneous deterministic interactions between a filament and either other filaments, linkers or the fluid are summed up in the determinisitic external forces $\boldsymbol{f}_{ext}$ and the moments $\boldsymbol{m}_{ext}$. These miscellaneous interactions may be long range interactions, e.g., owing to electrostatic potentials, or short range interactions, e.g., due to contact between different filaments or linkers or due to chemical bonds.

As the mass of a body scales cubically with its size, but its surface only quadratically, inertia can usually be neglected as compared to friction on the small length scale of single filaments in a polymer network so that the equation of motion is a differential equation of only first order in time. Mathematically, viscous forces and moments can typically be modeled as smooth functions, miscellaneous external forces and moments as smooth functions in case of long range interactions and as point loads in case of short range interactions. For the stochastic excitations $\boldsymbol{f}_{stoch}$ and $\boldsymbol{m}_{stoch}$, the situation is more difficult: physically, they are caused by the random thermal motion of a large number of particles in the surrounding fluid which interact with the filament for example by collisions or transient chemical bindings. Due to the tremendous number and small size of these particles as well as the approximate pairwise independence of their trajectories, the resulting stochastic excitation can be modeled by functions piecewise $\mathcal{C}^0$-continuous on intervals of the length $\Delta\xi \rightarrow 0$. Precisely, one models the stochastic excitation by so-called space-time white noise functions as discussed in more detail below. This turns the equation of motion into a stochastic partial differential equation (SPDE), which is usually referred to as Brownian equation of motion.

A key question for the simulation of biopolymer networks is how to discretize this SPDE in space and time efficiently. Despite the dominant role of Brownian dynamics (BD) in polymer physics [32], so far no mathematically consistent method for the simulation of the BD of rod-like continua has been proposed. Bead-spring and bead-rod models with explicit Euler time integration are the state of the art in computational polymer physics and well-known to capture the essential features of BD correctly. However, they are based on a merely intuitive spatial discretization of polymers. Moreover, they either require non-physical constraints entailing significant intricacies and rendering the simulation of certain phenomena such as axial extension of filaments impossible [72], or they suffer from serious performance problems when employed for the simulation of large systems [54, 55]. In structural engineering, much more efficient and mathematically well founded computational techniques have been developed since the 1980s for rod-like continua (cf. [77] for an overview). However, these techniques have been developed for deterministic differential equations and cannot be transferred straight forward to SPDEs. Therefore in section 3 a new approach for the simulation of the BD of rod-like continua is developed which combines the ideas of statistical physics underlying to bead-spring and bead-rod models with the highly efficient and mathematically stringent discretization methods from structural engineering.

2.3 Linkers

Filaments in biopolymer networks may be connected mechanically by crosslinking molecules, to which we will refer in the following also as linkers. Linkers are typically between $5nm$ (fascin, [82]) and $100nm$ (filamin, [13]) long and thus much smaller than the filaments in the networks, which are typically some microns long. They can form up to two chemical bonds with so-called binding sites on the filaments. Hence, we may distinguish between three states of linkers:

(I) free (i.e., without any chemical bond to any filament),

(II) singly bound (i.e., with one chemical bond to some filament),

(III) doubly bound (i.e., with two chemical bonds to filaments).

Free linkers are solved as particles in the fluid and not expected to take part in the force transmission in the network perceptibly. Rather they represent a pool of particles which can form chemical bonds with filaments close by and thereby change to a state of greater mechanical importance. Therefore only the position of these particles matters, because it is the basis for the decision which filaments are close enough to establish a chemical bond. Neglecting their internal structure fluctuations, they are thus modeled as point-shaped particles moving through the network stochastically according to the laws of Newtonian and statistical mechanics.

Linkers which are already bound to one filament are not supposed to perceptibly affect the network mechanics, either. Excessive amounts of such linkers may change the effective stiffness of the filament to which they are attached, but even this effect is expected to be negligible in most cases. Therefore such linkers are still modeled as point-shaped particles, but not in stochastic Brownian motion, but rather attached to a filament at a certain point. If they come close enough to another binding site they may form a second chemical bond and become doubly bound linkers.

Linkers having established chemical bonds to two filaments can be modeled as rod-like continua coupling these filaments with an effective stretching, shear, torsion and bending stiffness. As also the filaments themselves, they are subject to viscous damping and stochastic excitation from the fluid. Indeed this rough model is not expected to resolve the internal deformation of linkers accurately. However, on the basis of the data available about linkers at the moment, this seems impossible anyway: the small size of linkers significantly complicates experimental studies of their mechanical properties, and so far this lack of experimental data has been compensated only partially by data from MD simulations. Once more information will be available about linkers in the future, the here introduced linker model can be refined easily and without major implications for the filament and fluid model.

Altogether, in a computer simulation based on the above linker model, for free and singly bound linkers only the positions have to be tracked, whereas for doubly bound linkers also the force transmission they allow between filaments has to be captured. How to do so, is pointed out exactly in section 4.

2.4 Interactions

Not only fluid, filaments, and linkers have to be modeled, but rather also the interactions between them. As discussed above, the interactions between fluid and filaments can be captured by viscous and stochastic forces and moments in the equation of motion of the filaments. The same is true also for linkers, of course. Thus, only interactions between filaments and linkers remain to be discussed. In experiments so far three main types of such interactions have been observed:

(I) chemical interactions,

(II) contact interactions,

(III) long-range electrostatic interactions.

Chemical interactions lead to the formation of chemical bonds between linkers and filaments and turn thereby free linkers into singly bound ones and singly bound linkers into doubly bound ones. These bonds are in general only temporary and disaggregate after a while stochastically owing to thermal fluctuations. Such unbinding events turn doubly bound linkers into a singly bound ones and a singly bound linkers into a free ones. Contact interactions play an important role when filaments and linkers come close to each other and prevent them from overlapping. Physically, they are short-range electrostatic interactions. In addition to that, in principle also long-range electrostatic interactions may result from the fact that filaments and linkers are in general electrically charged. It is often doubted that long-range electrostatic interactions play an important role in biopolymer networks, because the charge of filaments and linkers is supposed to be shielded on long distances quite effectively by ions in the surrounding fluid. Yet the results of certain experiments [67] raise the question, whether there are not at least certain cases where long-range electrostatic interactions play a role in biopolymer networks. Discussing whether, when or to which extent this is the case, would go beyond the scope of this thesis. Thus, long-range electrostatic interactions are listed in this section as potential interaction type between filaments and linkers noting that in practice they may often or even always play only a minor role. Therefore altogether three types of interactions are in general to be modeled in simulations of biopolymer networks, and how to do so is discussed in section 5.

2.5 Summary

Biopolymer networks can be modeled on a micromechanical scale as complex systems consisting of three main constituents: a fluid, filaments and linkers. These can be modeled as continua, respectively. Often the fluid can be handled by standard methods and even without a discretization. In opposition to that, filaments, linkers and the interactions between them have to be considered explicitly in a numerical simulation. How to do so will be discussed in detail in the sections 3, 4 and 5.

3 Numerical model of the Brownian dynamics of rod-like continua

In this chapter, it is pointed out in detail how the Brownian dynamics of rod-like continua such as filaments in biopolyer networks can be modeled numerically. In general, motion and deformation of filaments in biopolymer networks in vivo occur in three dimensions. However, in certain experiments filament motion is confined to two dimensions either by a thin gap between two plates [37] or by certain proteins fixing the filaments to a plate [80]. The reason for this is that several experiments could be conducted in planar settings only so far. Moreover, also for certain processes in vivo such as the formation of lamellipodia, two dimensional deformation is assumed to play an important role. Although two dimensional filament dynamics can be simulated also by means of three dimensional computer models with suitable boundary conditions, genuinely two dimensional numerical models may be preferred in these cases due to their simplicity and much higher efficiency. Therfore we will discuss in the following both the two and three dimensional case explicitly whereever they differ from each other.

3.1 Equation of motion

A rod-like structure (referred to below simply as 'rod') of length L in $m_t \in \{2;3\}$ dimensions can be modeled as a one-dimensional Cosserat continuum embedded into $\mathbb{R}^{m_t}$. To this end, we assume that the geometry of the structure can be modeled at a certain point in time by some curve in space, the neutral line, to each point of which some plain cross section is assigned (see Fig. 3.1). For simplicity, we assume in the following that the cross sections at all points of the neutral line are congruent. Let $\xi \in [0;L]$ be the curve parameter of the neutral line. Then this line can be described in the time interval $[0;t_{max}]$ by the function

$$\boldsymbol{x} : [0;L] \times [0;t_{max}] \rightarrow \mathbb{R}^{m_t}, \quad (\xi,t) \mapsto \boldsymbol{x}(\xi,t), \tag{3.1}$$

To uniquely characterize the orientation of the cross section at each curve point, we define the rotation field

$$\boldsymbol{\theta} : [0;L] \times [0;t_{max}] \rightarrow \mathbb{R}^{m_r}, \quad (\xi,t) \mapsto \boldsymbol{\theta}(\xi,t), \tag{3.2}$$

with $m_r = \binom{m_t}{2}$ for $m_t \in \{2;3\}$. As briefly explained also in appendix A.1, the rotation $\boldsymbol{\theta}(\xi,t)$ is only for $m_t = 2$ a vector, whereas for $m_t = 3$ it is just a pseudo-vector. In either case, it corresponds to a spin matrix $\boldsymbol{S}(\boldsymbol{\theta}(\xi,t))$ and an orthonormal triad $\boldsymbol{R}(\boldsymbol{\theta}(\xi,t))$ whose columns $\boldsymbol{R}_i(\boldsymbol{\theta}(\xi,t))$ represent the principal axes of the cross section at $\boldsymbol{x}(\xi,t)$.

Thus, (3.1) and (3.2) together uniquely characterize the cross section position and orientation in space. As a consequence, the motion and deformation of the polymer in time is completely

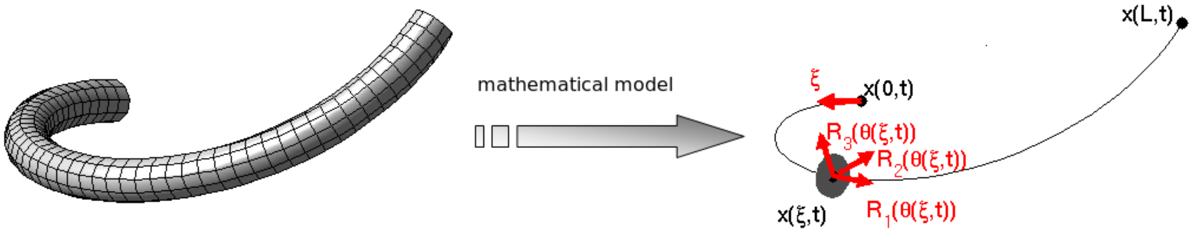

Figure 3.1: To model the mechanics of a rod-like continuum of length L at time t mathematically, a curve $\boldsymbol{x}(\xi, t)$ with curve parameter $\xi \in [0; L]$ is defined, the neutral line. To each point $\boldsymbol{x}(\xi, t)$ of the neutral line a cross section (illustrated by a circular disc) is assigned whose orientation in space is given by the column vectors $\boldsymbol{R}_i(\boldsymbol{\theta}(\xi, t))$ of a triad $\boldsymbol{R}(\boldsymbol{\theta}(\xi, t))$.[5]

described by the two functions $\boldsymbol{x}$ and $\boldsymbol{\theta}$. Let the stress-free initial configuration of the polymer at time $t = 0$ be given by

$$\boldsymbol{x}^0 : [0; L] \to \mathbb{R}^{m_t}, \quad \xi \mapsto \boldsymbol{x}^0(\xi) = \boldsymbol{x}(\xi, 0), \tag{3.3}$$

$$\boldsymbol{\theta}^0 : [0; L] \to \mathbb{R}^{m_r}, \quad \xi \mapsto \boldsymbol{\theta}^0(\xi) = \boldsymbol{\theta}(\xi, 0). \tag{3.4}$$

Then with proper boundary conditions at $\xi = 0$ and $\xi = L$ the functions $\boldsymbol{x}$ and $\boldsymbol{\theta}$ can be computed from the balance of linear and angular momentum, i.e. from

$$\boldsymbol{f}_{el}(\boldsymbol{x}, \boldsymbol{\theta}, \xi, t) + \boldsymbol{f}_{visc}(\boldsymbol{x}, \boldsymbol{\theta}, \xi, t) = \boldsymbol{f}_{ext}(\boldsymbol{x}, \xi, t) + \boldsymbol{f}_{stoch}(\boldsymbol{x}, \boldsymbol{\theta}, \xi, t), \tag{3.5a}$$

$$\boldsymbol{m}_{el}(\boldsymbol{x}, \boldsymbol{\theta}, \xi, t) + \boldsymbol{m}_{visc}(\boldsymbol{x}, \boldsymbol{\theta}, \xi, t) = \boldsymbol{m}_{ext}(\boldsymbol{x}, \xi, t) + \boldsymbol{m}_{stoch}(\boldsymbol{x}, \boldsymbol{\theta}, \xi, t) + \boldsymbol{x}'(\xi, t) \times \boldsymbol{f}_s(\boldsymbol{x}, \boldsymbol{\theta}, \xi, t). \tag{3.5b}$$

Here $\boldsymbol{f}_{visc}$, $\boldsymbol{m}_{visc}$, $\boldsymbol{f}_{stoch}$, $\boldsymbol{m}_{stoch}$, $\boldsymbol{f}_{ext}$, $\boldsymbol{m}_{ext}$ are the viscous, stochastic and deterministic external force and moment loads per unit length already introduced in section 2. The tangent of the neutral line is denoted by $\boldsymbol{x}'(\xi, t) := \partial \boldsymbol{x}(\xi, t)/\partial \xi$. The elastic section force $\boldsymbol{f}_s$ and the elastic section moment $\boldsymbol{m}_s$ are, as usual for one-dimensional continua, defined as the integral and resulting moment of the internal stresses. The derivatives of the section force and moment with respect to ξ are $\boldsymbol{f}_{el}$ and $\boldsymbol{m}_{el}$, respectively. Note that $\boldsymbol{f}_{el}$, $\boldsymbol{f}_{visc}$, $\boldsymbol{f}_{stoch}$ and $\boldsymbol{f}_{ext}$ are forces per unit length, and $\boldsymbol{m}_{el}$, $\boldsymbol{m}_{visc}$, $\boldsymbol{m}_{stoch}$ and $\boldsymbol{m}_{ext}$ moments per unit length. Thus all these quantities are what is in structural mechanics referred to as line loads or distributed loads. In the following, we generally denote a derivative in time by a dot (for example $\dot{\boldsymbol{x}}(\xi, t)$) and a derivative with respect to the curve parameter ξ by a prime (for example $\boldsymbol{x}'(\xi, t)$). Quantities referring to the direction

---

[5] Reprinted Fig. with permission from [30]. ©2012 by John Wiley & Sons, Ltd.

parallel and orthogonal to the neutral line of the rod will be marked in the following by the lower indices $(.)_{\|}$ and $(.)_{\perp}$, respectively. Similarly, quantities with respect to translational and rotational degrees of freedom will be denoted by the indices $(.)_t$ and $(.)_r$, respectively. To simplify notation, we will drop in the following the arguments of functions, whenever it is apparent that we refer to some specific function value rather than to a function itself. Especially, we will often write $\boldsymbol{\theta}$ or $\boldsymbol{x}$ instead of $\boldsymbol{x}(\xi, t)$ or $\boldsymbol{\theta}(\xi, t)$. The symbols $\boldsymbol{S}$ and $\boldsymbol{R}$ will be reserved for spin and rotation matrices exclusively.

3.1.1 Elastic forces and moments

As already mentioned in section 2, single-molecule experiments have successfully demonstrated that on a micrometer scale rods can still be modeled as continua with stretching, bending and torsion stiffness employing the linear strain measures common for beams in structural engineering. Thus the elastic forces and moments in these structures can be determined similarly as in macroscopic structural mechanics. In principle, they can be calculated on the basis of any nonlinear beam theory, especially on the basis of the Euler-Bernoulli and Reissner theory. In the following, we will denote by E and G the beam's Young's and shear modulus. In BD simulations, special attention has to be payed to the definition of the geometric quantities J_r, J_i, A, and A_i. These quantitities are defined in BD simulations not only as polar moment of intertia, moment of inertia of area with respect to the i-th principal axis, cross section and shear corrected cross section with respect to the i-th principal axis, but rather as these quantities multiplied by some 'ionic correction factor'. The reason for this is that the mechanical structures considered in BD simulations are typically charged and therefore coated by a cloud of ions. The precise way these ionic effects are to be accounted for depends on the geometry of the structures and the solvent they are embedded in. Indeed there may be cases where the ionic motion has to be factored into the external load vectors $\boldsymbol{f}_{ext}$ and $\boldsymbol{m}_{ext}$ in some way or where it has even to be accounted for by some additional simulation. However, a series of experiments has shown (e.g. [2, 12]) that in many cases of practical relevance the ionic effects are small and can be accounted for similarly to the shear correction factor by 'ionic correction factors' changing the effective bending, torsion, stretching and shear stiffness compared to the values one would get from a classical continuum mechanical calculation. These ionic correction factors may be determined for a certain combination of mechanical structure and fluid either experimentally or by some additional computer simulation. In the following we will assume that all ionic effects can be accounted for by a proper correction factor and that this factor or rather J_r, J_i, A, and A_i are known prior to the simulation.

It is underlined that only the computation of $\boldsymbol{f}_s$, $\boldsymbol{m}_s$, $\boldsymbol{f}_{el}$ and $\boldsymbol{m}_{el}$ in (3.5) directly depends on the beam model employed, whereas all other quantities in the equation of motion can be computed independently. As a consequence, the BD framework presented in the sections below can be combined with any beam model for the elasticity and thus especially also with any finite beam element. For the examples presented in section 6, finite elements on the basis of Reissner's theory are used, and in the following two subsections the computation of the elastic quantities according to this theory is pointed out precisely both in three and two dimensions.

3.1.1.1 Reissner beam equations in three dimensions

According to [23, 50, 77], the Reissner beam equations read in three dimensions

$$\boldsymbol{f}_{el} = \frac{\partial}{\partial \xi} \left\{ \boldsymbol{R}(\boldsymbol{\theta}) \boldsymbol{k}_t \left[\boldsymbol{R}(\boldsymbol{\theta})^T \boldsymbol{x}' - \boldsymbol{R}(\boldsymbol{\theta}^0)^T \boldsymbol{x}'^0 \right] \right\} \tag{3.6}$$

$$\boldsymbol{k}_t = \begin{pmatrix} EA & 0 & 0 \\ 0 & GA_2 & 0 \\ 0 & 0 & GA_3 \end{pmatrix} \tag{3.7}$$

$$\boldsymbol{m}_{el} = \frac{\partial}{\partial \xi} \left\{ \boldsymbol{R}(\boldsymbol{\theta}) \boldsymbol{k}_r \left[\boldsymbol{\kappa}_{loc} - \boldsymbol{\kappa}_{loc}{}^0 \right] \right\}, \tag{3.8}$$

$$\boldsymbol{S}(\boldsymbol{\kappa}_{loc}) = \boldsymbol{R}(\boldsymbol{\theta})^T \boldsymbol{R}'(\boldsymbol{\theta}) \tag{3.9a}$$

$$\boldsymbol{S}(\boldsymbol{\kappa}^0_{loc}) = \boldsymbol{R}(\boldsymbol{\theta}^0)^T \boldsymbol{R}'(\boldsymbol{\theta}^0) \tag{3.9b}$$

$$\boldsymbol{k}_r = \begin{pmatrix} GJ_r & 0 & 0 \\ 0 & EJ_2 & 0 \\ 0 & 0 & EJ_3 \end{pmatrix}, \tag{3.10}$$

where $\boldsymbol{\kappa}_{loc}$ and $\boldsymbol{\kappa}^0_{loc}$ are the curvature vectors in the local coordinate system attached to the cross section triad in the current and reference configuration, respectively. They are defined implicitly by their spin matrices $\boldsymbol{S}(\boldsymbol{\kappa}_{loc})$ and $\boldsymbol{S}(\boldsymbol{\kappa}^0_{loc})$ in (3.9). Some explanations about the rotation matrices $\boldsymbol{R}$ and spin matrices $\boldsymbol{S}$ are given in appendix A.1. The local curvature vectors can be imagined geometrically as follows: their i-th component is the angle increment per increment in the parameter space by which the triad $\boldsymbol{R}$ rotates around its i-th axis when proceeding along the continuum. Thus the first component of the local curvature vector corrsponds to the mechanical torsion, its second and third component to the bending curvature around the second and third principal axis of the cross section, respectively.

Applying the above equations to BD simulations of biopolymer networks assumes that torsion of polymers on micrometer length scale can be dealt with similarly as in macroscopic problems of structural engineering. This is in accordance with experiments such as the those presented in [90, 96]. Despite such experimental evidence, there are even recent examples, such as [54], where torsion of polymers is modeled in BD simulations as known from MD simulations, i.e., by the dihedral torsion. In appendix B.2 it is shown that this is equivalent to the assumption of a continuum whose torsion potential depends on the torsion of the Frenet-Serret-frame of its neutral line. This is not only in opposition to experimental findings, but additionally goes along with a severe numerical problem: the Frenet-Serret-torsion (and similarly the dihedral angle, its discrete counterpart) exhibits a singularity at straight segments of the rod. In MD simulations, the application of the dihedral angle can be justified especially for peptides by atomistic considerations, and these can also help fixing the singularity problem by the definition of a suitable torsion potential [11]. For continuous rods neither is possible. There obviously a Cosserat continuum has to be used to account for torsion in a correct and numerically stable way. This reveals a favorable property of the application of nonlinear finite beam elements in BD simulations: they naturally account for torsion in a proper way, whereas classical BD simulation methods such as bead-spring- and bead-rod-models do not capture torsion at all by default and do so only at the cost of intricate extensions [4, 16, 17]. Such extensions are often not only used for the sake of torsion, but also to capture anisotropic bending stiffnesses, e.g., of DNA [4]. Again, capturing such an anisotropy is not possible by classical bead-spring-models by default owing to their lack of material triads, but it is naturally possible by finite beam elements.

3.1.1.2 Reissner beam equations in two dimensions

In two dimensions the rotation $\boldsymbol{\theta}$ becomes an additive scalar, which enables significant simplifications as compared to the three dimensional case. According to [21], the elastic forces and moments in a two dimensional Reissner beam are given by

$$\boldsymbol{f}_{el} = \frac{\partial}{\partial \xi} \left\{ \boldsymbol{R}(\boldsymbol{\theta}) \boldsymbol{k}_t \left[\boldsymbol{R}(\boldsymbol{\theta})^T \boldsymbol{x}' - \boldsymbol{R}(\boldsymbol{\theta}^0)^T \boldsymbol{x}'^0 \right] \right\} \tag{3.11}$$

$$\boldsymbol{k}_t = \begin{pmatrix} EA & 0 \\ 0 & GA_2 \end{pmatrix} \tag{3.12}$$

$$\boldsymbol{m}_{el} = \frac{\partial}{\partial \xi} \left\{ \boldsymbol{k}_r \left(\boldsymbol{\theta}' - \boldsymbol{\theta}'^0 \right) \right\}, \tag{3.13}$$

$$\boldsymbol{k}_r = EJ_2. \tag{3.14}$$

3.1.2 Viscous forces and moments

For the reasons discussed in section 2.1, a linear relationship between the viscous forces and moments on the one hand and the velocity of the filaments relative to the background fluid on the other hand can be assumed. Thus, the viscous damping force and moment are given in general by

$$\boldsymbol{f}_{visc} = \boldsymbol{c}_t \left[\dot{\boldsymbol{x}} - \boldsymbol{v}(\boldsymbol{x}) \right], \tag{3.15a}$$

$$\boldsymbol{m}_{visc} = \boldsymbol{c}_r \left[\dot{\boldsymbol{\theta}} - \boldsymbol{\omega}(\boldsymbol{x}) \right]. \tag{3.15b}$$

Here $\boldsymbol{v}$ and $\boldsymbol{\omega}$ are the translational and rotational velocity field of the background fluid, and $\boldsymbol{c}_t$ and $\boldsymbol{c}_r$ are matrix-valued functions depending in general on ξ and t as well as on $\boldsymbol{x}$ and $\boldsymbol{\theta}$ and their derivatives. The damping coefficients forming the elements of $\boldsymbol{c}_t$ and $\boldsymbol{c}_r$ can be computed in various ways. In practice, the curvatures of filaments in biopolymer networks and their velocities relative to the background fluid often remain moderate so that their damping coefficients can be set in good approximation equal to the ones of straight cylindric rods of length L and diameter d moving through a resting fluid. In the following sections, we will point out, how to compute under this assumption the damping matrices $\boldsymbol{c}_t$ and $\boldsymbol{c}_r$ in three and two dimensions, respectively.

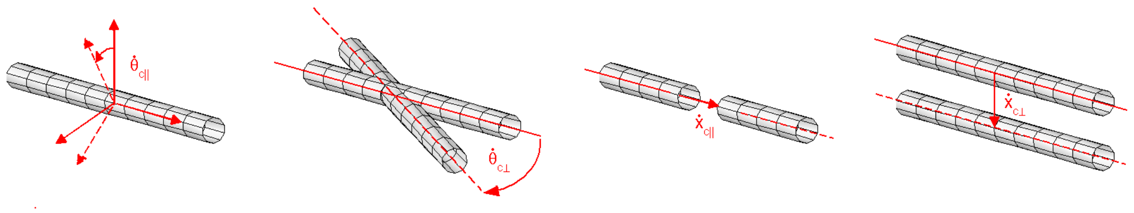

(a) (b) (c) (d)

Figure 3.2: Different velocity components for motion of a rigid rod in $\mathbb{R}^3$

3.1.2.1 Damping matrices for rigid, straight rods

In $\mathbb{R}^3$, any motion of a rigid straight rod can be described uniquely by four different velocity components at the rod center as illustrated in Fig. 3.2: translation velocity $\dot{\boldsymbol{x}}_{c\perp}$ perpendicular to the rod axis, translation velocity $\dot{\boldsymbol{x}}_{c\|}$ parallel to the rod axis, rotation velocity $\dot{\boldsymbol{\theta}}_{c\perp}$ perpendicular to the rod axis, and rotation velocity $\dot{\boldsymbol{\theta}}_{c\|}$ around the rod axis. In a Newtonian fluid, these four velocities cause resulting damping forces and moments directly proportional to the velocities and pointing in the opposite direction. The proportionality factors between the velocities and these damping forces and moments are denoted by $\zeta_{t\perp}$, $\zeta_{t\|}$, $\zeta_{r\perp}$, and $\zeta_{r\|}$, respectively. On the other hand, the resulting damping forces and moments on a rod with the above described velocities can be expressed also in terms of the viscous forces $\boldsymbol{f}_{visc}$ and moments $\boldsymbol{m}_{visc}$ per unit length from (3.15), which gives

$$\zeta_{t\perp}\dot{\boldsymbol{x}}_{c\perp} = \left[\int_0^L \boldsymbol{f}_{visc} d\xi\right]_{\dot{\boldsymbol{\theta}}=\boldsymbol{0},\dot{\boldsymbol{x}}=\dot{\boldsymbol{x}}_{c\perp}}, \tag{3.16a}$$

$$\zeta_{t\|}\dot{\boldsymbol{x}}_{c\|} = \left[\int_0^L \boldsymbol{f}_{visc} d\xi\right]_{\dot{\boldsymbol{\theta}}=\boldsymbol{0},\dot{\boldsymbol{x}}=\dot{\boldsymbol{x}}_{c\|}}. \tag{3.16b}$$

$$\zeta_{r\perp}\dot{\boldsymbol{\theta}}_{c\perp} = \left[\int_0^L \left(\boldsymbol{m}_{visc} + (\boldsymbol{x}(\xi) - \boldsymbol{x}_c)\times\boldsymbol{f}_{visc}\right) d\xi\right]_{\dot{\boldsymbol{\theta}}=\dot{\boldsymbol{\theta}}_{c\perp},\dot{\boldsymbol{x}}=(\boldsymbol{x}(\xi)-\boldsymbol{x}_c)\times\dot{\boldsymbol{\theta}}_{\perp}}, \tag{3.16c}$$

$$\zeta_{r\|}\dot{\boldsymbol{\theta}}_{c\|} = \left[\int_0^L \boldsymbol{m}_{visc} d\xi\right]_{\dot{\boldsymbol{\theta}}=\dot{\boldsymbol{\theta}}_{c\|},\dot{\boldsymbol{x}}=\boldsymbol{0}}, \tag{3.16d}$$

Realizing that the integrands in (3.16a) and (3.16b) are constant over ξ, these two equations can be rewritten as

$$\zeta_{t\perp}\dot{\boldsymbol{x}}_{c\perp} = L\boldsymbol{c}_t\dot{\boldsymbol{x}}_{c\perp}, \tag{3.17a}$$

$$\zeta_{t\|}\dot{\boldsymbol{x}}_{c\|} = L\boldsymbol{c}_t\dot{\boldsymbol{x}}_{c\|}. \tag{3.17b}$$

Noting that $\dot{\boldsymbol{x}}_{c\perp}$ and $\dot{\boldsymbol{x}}_{c\|}$ point parallel or orthogonal to the rod axis, it is obvious that the eigenvectors of $\boldsymbol{c}_t$ are the three columns of the material triad $\boldsymbol{R}$ attached to the rod and the related eigenvalues are $\zeta_{t||}/L$ and $\zeta_{t\perp}/L$, which immediately provides the unique solution for $\boldsymbol{c}_t$. Together with this result the same argumentation leads to the solution also for $\boldsymbol{c}_r$, and one has in three dimensions

$$\boldsymbol{c}_t = \boldsymbol{R}(\boldsymbol{\theta}) \begin{pmatrix} \gamma_{t||} & 0 & 0 \\ 0 & \gamma_{t\perp} & 0 \\ 0 & 0 & \gamma_{t\perp} \end{pmatrix} \boldsymbol{R}(\boldsymbol{\theta})^T =: \boldsymbol{R}(\boldsymbol{\theta}) \boldsymbol{c}_{t,loc} \boldsymbol{R}(\boldsymbol{\theta})^T \tag{3.18a}$$

$$\boldsymbol{c}_r = \boldsymbol{R}(\boldsymbol{\theta}) \begin{pmatrix} \gamma_{r||} & 0 & 0 \\ 0 & \gamma_{r\perp} & 0 \\ 0 & 0 & \gamma_{r\perp} \end{pmatrix} \boldsymbol{R}(\boldsymbol{\theta})^T =: \boldsymbol{R}(\boldsymbol{\theta}) \boldsymbol{c}_{r,loc} \boldsymbol{R}(\boldsymbol{\theta})^T, \tag{3.18b}$$

and in two dimensions

$$\boldsymbol{c}_t := \boldsymbol{R}(\boldsymbol{\theta}) \boldsymbol{c}_{r,loc} \boldsymbol{R}(\boldsymbol{\theta})^T = \boldsymbol{R}(\boldsymbol{\theta}) \begin{pmatrix} \gamma_{t||} & 0 \\ 0 & \gamma_{t\perp} \end{pmatrix} \boldsymbol{R}(\boldsymbol{\theta})^T, \tag{3.19a}$$

$$\boldsymbol{c}_r := \gamma_{r\perp} \tag{3.19b}$$

with

$$\gamma_{t\perp} = \zeta_{t\perp}/L, \tag{3.20a}$$

$$\gamma_{t||} = \zeta_{t||}/L. \tag{3.20b}$$

$$\gamma_{r\perp} = \zeta_{r\perp}/L - \zeta_{t\perp}L/12, \tag{3.20c}$$

$$\gamma_{r||} = \zeta_{r||}/L, \tag{3.20d}$$

It is underlined that ζ denotes here effective friction coefficients for the whole rod, whereas γ denotes friction coefficients per unit length. For a rigid straight rod, the first column of the rotation matrix is equivalent to the unit tangent vector of the rod, i.e., $\boldsymbol{R}_1 = \boldsymbol{x}'$. Elementary calculus reveals that therefore $\boldsymbol{c}_t$ can be written both in two and three dimensions equivalently as

$$\boldsymbol{c}_t = \boldsymbol{1}\gamma_{t\perp} + (\gamma_{t||} - \gamma_{t\perp}) \boldsymbol{x}' \otimes \boldsymbol{x}'. \tag{3.21}$$

It is underlined that (3.18a) and (3.19a) are equivalent to (3.21) only for the rigid rod considered in this section. In case of shear deformation, both ways of expressing the friction tensor distinguish in general. However, for biopolymers shear is not expected to play a major role owing to their high slenderness ratio. Indeed several of the examples presented in section 6 were tested with both expressions for the friction tensor, and no perceptible difference in the physically interesting quantities was found.

3.1.2.2 Computation of damping coefficients

With (3.15), (3.18), (3.19), (3.20) and (3.21), the viscous quantities in (3.5) can be computed immediately once one knows the damping constants. In the following, we will discuss three of the numerous possible ways to determine them.

Computation by means of formulae: In the literature formulae for the computation of the friction coefficients of stiff rods can be looked up. For example, Table 6.2 in [46] indicates

$$\zeta_{t\perp} = \frac{4\pi\eta L}{\ln(L/d) + 0.84}, \tag{3.22a}$$

$$\zeta_{t\|} = \frac{2\pi\eta L}{\ln(L/d) - 0.2}, \tag{3.22b}$$

$$\zeta_{r\perp} = \frac{\pi\eta L/3}{\ln(L/d) - 0.66}. \tag{3.22c}$$

$$\zeta_{r\|} = \pi\eta d^2 L, \tag{3.22d}$$

These formulae can be applied if the viscosity η of the surrounding fluid as well as the length L and diameter d of the rods are known. By (3.20), (3.18), (3.19) and (3.21), they allow for the immediate computation of the damping matrices in a certain configuration.

Computation by means of diffusion coefficients Sometimes, only diffusion coefficients (cf. B.1 for further reading) are known, e.g., from experiments, and the damping matrices have to be computed in accordance with them. Typically, three diffusion coefficients are known for a certain structure, the translational diffusion coefficient D_t, the orthogonal rotational diffusion coefficient $D_{r\perp}$ and the axial rotational diffusion coefficient $D_{r\|}$, which provide three equations (see (B.11)) for the computation of the four damping coefficients. A fourth equation follows from a consideration of the relation between $\zeta_{r\perp}$ and $\zeta_{t\perp}$. To this end, one assumes that there is no difference between the hydrodynamic interactions caused by a rotation and translation orthogonal to the rod axis. Then $\zeta_{t\perp}/L$ should be the friction coefficient per unit length for any length segment of the rod moving through the fluid perpendicularly to the rod axis. A pure rotation $\dot{\boldsymbol{\theta}}_\perp$ of the rod orthogonal to its axis and about its center, however, is equivalent to a motion of each point on the rod orthognoal to the rod axis and with a velocity proportional to the lever between this point and the center. Therefore it is possible to express the resulting damping moment by

$$\zeta_{r\perp}\dot{\boldsymbol{\theta}}_\perp = \int_0^L \zeta_{t\perp}/L\dot{\boldsymbol{\theta}}_\perp(\xi - L/2)d\xi = \frac{L^2\zeta_{t\perp}\dot{\boldsymbol{\theta}}_\perp}{12}, \tag{3.23}$$

which immediately gives

$$\zeta_{r\perp} = \frac{L^2\zeta_{t\perp}}{12}. \tag{3.24}$$

This relation, which was gained just by the neglection of the difference between the hydrodynamic interactions caused by translations and rotations perpendicular to the rod axis, provides an additional equation to (B.11), enabling finally the computation of the damping coefficients from the diffusion coefficients in $m_t \in \{2; 3\}$ dimensions by

$$\zeta_{t\perp} = \frac{12k_B T}{L^2 D_{r\perp}}, \tag{3.25a}$$

$$\zeta_{t\|} = \frac{k_B T}{m_t D_t - L^2(m_t - 1)D_{r\perp}/12}, \tag{3.25b}$$

$$\zeta_{r\perp} = \frac{k_B T}{D_{r\perp}}. \tag{3.25c}$$

$$\zeta_{r\|} = \frac{k_B T}{D_{r\|}}. \tag{3.25d}$$

Computation by means of simplified formulae: The formulae (3.22) require detailed information about length and diameter of the structure. Sometimes such information is not available (especially for the diameter), but yet at least a rough estimate for the damping coefficients is necessary to run simulations. In this case, often a simplified version of (3.22) is employed [14, 42] where the correction terms for different hydrodynamic phenomena are omitted, which gives

$$\zeta_{t\perp} = 4\pi\eta L, \tag{3.26a}$$

$$\zeta_{t\|} = 2\pi\eta L, \tag{3.26b}$$

$$\zeta_{r\perp} = \pi\eta L^3/3, \tag{3.26c}$$

$$\zeta_{r\|} = \pi\eta d^2 L. \tag{3.26d}$$

Using (3.26), perceptible deviations between simulated and real filament dynamics may arise. However, for the simulation of a variety of static quantities and probability distributions important in polymer physics, this deficiency does not matter at all, and using (3.26) usually allows for computer simulations on the basis of very limited knowledge, but yet with parameters close enough to the real ones in order not to miss important key phenomena.

3.1.3 External forces and moments

Only little can be stated in general about the external forces and moments, as these functions may vary from application to application. Usually, they depend only on the position $\boldsymbol{x}(\xi, t)$ and the tangent $\boldsymbol{x}'(\xi, t)$ and do not entail any significant mathematical or practical problems so that we will skip any further discussion of these terms and assume that they can be handled by standard techniques. In practice, external loads may be for example electrostatic forces or contact forces owing to interactions of a filament with other filaments, linkers or also itself.

3.1.4 Stochastic forces and moments

The stochastic forces and moments acting on the rod originate from interactions such as collisions with particles in the surrounding fluid. Owing to the stochastic nature of these particles' motion, they can be modeled as stochastic loads per unit length summing up the excitation exerted by all surrounding particles. As the motion of these particles has no preferred direction, the mean value of the stochastic load is zero. Since it is furthermore assumed to happen on much a faster time and much a smaller length scale than relevant for the dynamics of the rod, the correlation length of the stochastic loads both in space and time is assumed to be zero. The stochastic excitation results from the superposition of interactions with numerous particles. The set of all particles can be subdivided into subsets of identical particles. For each of these subsets, the way its particles interact with the rod follows the same probability distribution. As a consequence of the law of large numbers, the stochastic loads are therefore Gaussian random variables. Gaussian random variables are uniquely characterized by their first and second moment. Since the mean value of the stochastic loads is known to be zero, only their variance remains to be determined. To this end, one has to recall that the laws of statistical mechanics imply that each degree of freedom of a system immersed into a thermal bath of temperature T has the average energy $k_BT/2$, where k_B is the Boltzmann constant. Thus the mean absolute value of the stochastic loads (and thereby their variance) can be calculated from the requirement that they have to deform the rod so that the average elastic energy stored in each eigenmode is $k_BT/2$. Lengthy derivations [32] reveal the so-called fluctuation-dissipation theorem (cf. appendix B.1.1), which characterizes the stochastic forces and moments by

$$\langle \boldsymbol{f}_{stoch} \rangle = 0, \tag{3.27a}$$

$$\langle \boldsymbol{f}_{stoch}(t,\xi) \otimes \boldsymbol{f}_{stoch}(t^*,\xi^*) \rangle = 2k_BT\boldsymbol{c}_t\delta_{tt^*}\delta_{\xi\xi^*}, \tag{3.27b}$$

$$\langle \boldsymbol{m}_{stoch} \rangle = 0, \tag{3.28a}$$

$$\langle \boldsymbol{m}_{stoch}(t,\xi) \otimes \boldsymbol{m}_{stoch}(t^*,\xi^*) \rangle = 2k_BT\boldsymbol{c}_r\delta_{tt^*}\delta_{\xi\xi^*}, \tag{3.28b}$$

where t, t^* and ξ, ξ^* represent in general different points in time and space, respectively, and δ_{tt^*} is the Dirac-function with argument $t - t^*$. Mean values are denoted by $\langle . \rangle$. As can be seen in the above equations, the fluctuation-dissipation theorem states a relation between the damping tensors governing the friction and the mean amplitudes of the stochastic loads. This aspect underlines the common origin of both quantities in the interactions of the rod with surrounding particles.

Due to the δ-correlation, a Fourier transform of $\boldsymbol{f}_{stoch}$ and $\boldsymbol{m}_{stoch}$ in space and time is a constant function, i.e., all frequencies are equally represented. Therefore, $\boldsymbol{f}_{stoch}$ and $\boldsymbol{m}_{stoch}$ are so-called white-noise excitations (cf. appendix A.2) and can thus be expressed in terms of generalized derivatives of the multidimensional standard Wiener processes $\boldsymbol{\mathcal{W}}_t(\xi,t)$, $\boldsymbol{\mathcal{W}}_r(\xi,t)$ by

$$\boldsymbol{f}_{stoch} = \sqrt{2k_BT}\boldsymbol{s}_t\frac{\partial^2\boldsymbol{\mathcal{W}}_t(\xi,t)}{\partial\xi\partial t} \tag{3.29a}$$

$$\boldsymbol{m}_{stoch} = \sqrt{2k_BT}\boldsymbol{s}_r\frac{\partial^2\boldsymbol{\mathcal{W}}_r(\xi,t)}{\partial\xi\partial t}. \tag{3.29b}$$

Here, $\boldsymbol{s}_t$ and $\boldsymbol{s}_r$ are some matrices satisfying $\boldsymbol{s}_t\boldsymbol{s}_t^T = \boldsymbol{c}_t$ and $\boldsymbol{s}_r\boldsymbol{s}_r^T = \boldsymbol{c}_r$. In appendix A.4, a decomposition into such matrices is provided for all damping matrices discussed in this thesis.

3.1.5 Weak form of the equation of motion

For the derivation of numerical methods, it is useful writing (3.5) in the weighted-residual form. To this end, we multiply the linear and angular momentum balance in (3.5) with weighting functions W_t and W_r and integrate in space, which gives

$$\int_0^L W_t \boldsymbol{f}_{el} d\xi + \int_0^L W_t \boldsymbol{f}_{visc} d\xi = \int_0^L W_t \boldsymbol{f}_{ext} d\xi + \int_0^L W_t \boldsymbol{f}_{stoch} d\xi, \tag{3.30a}$$

$$\int_0^L W_r \boldsymbol{m}_{el} d\xi + \int_0^L W_r \boldsymbol{m}_{visc} d\xi = \int_0^L W_r \boldsymbol{m}_{ext} d\xi + \int_0^L W_r \boldsymbol{m}_{stoch} d\xi + \int_0^L W_r \boldsymbol{x}' \times \boldsymbol{f}_s d\xi. \tag{3.30b}$$

The application of Gauss' divergence theorem to (3.30) leads to the weak form

$$\int_0^L \left(-W_t' \boldsymbol{f}_s + W_t \boldsymbol{f}_{visc}\right) d\xi = \int_0^L \left(W_t \boldsymbol{f}_{stoch} + W_t \boldsymbol{f}_{ext}\right) d\xi + \left[W_t \boldsymbol{f}_{bd}\right]_0^L, \tag{3.31a}$$

$$\int_0^L \left(-W_r' \boldsymbol{m}_s + W_r \boldsymbol{m}_{visc}\right) d\xi = \int_0^L \left(W_r \boldsymbol{m}_{stoch} + W_r \boldsymbol{x}' \times \boldsymbol{f}_s + W_r \boldsymbol{m}_{ext}\right) d\xi + \left[W_r \boldsymbol{m}_{bd}\right]_0^L, \tag{3.31b}$$

where $[\ldots]_0^L$ denotes the difference between the function in brackets evaluated at $\xi = L$ and at $\xi = 0$, respectively, and $\boldsymbol{f}_{bd}(\xi)$ and $\boldsymbol{m}_{bd}(\xi)$ the external boundary forces and moments at $\xi = 0$ and $\xi = L$. For deterministic partial differential equations, it is well-known that the strong form is satisfied if and only if the weak form is satisfied for all weightings functions out of a sufficiently large function space. It is underlined that the situation here is different as (3.5) is an SPDE owing to the space-time white noise in (3.29), and mathematical statements for deterministic partial differential equations are not necessarily true also for SPDEs. However, the equivalence of strong and weak form can be proven also for SPDEs under fairly general conditions [10] so that for the development of a finite element approach to the BD of rod-like continua we can take the weak form (3.31) as a convenient basis.

3.2 Discretization

3.2.1 General framework

The SPDE (3.5) can be discretized by finite elements in space and a backward Euler scheme in time. To this end, we consider only the $i_{max} + 1$ discrete points in time $t^i = i\Delta t$ with $i \in \{0, 1, 2, \ldots, i_{max}\}$, $\Delta t = t_{max}/i_{max}$. Quantities at the point in time t^i will be denoted in the following by an upper index i. Let the parameter space $[0; L]$ be discretized by k_{max} nodes $\xi^{[k]}$, $k \in \{1, 2, \ldots, k_{max}\}$ with the uniform discretization length $h = L/(k_{max} - 1)$. To each node $\xi^{[k]}$ we assign at the point in time t^i the two vectors $\boldsymbol{X}^{i[k]}, \boldsymbol{\Theta}^{i[k]} \in \mathbb{R}^{m_r}$, which denote the approximated position in the physical space and orientation of the beam cross section at these nodes, respectively. For the translational degrees of freedom, a standard isoparametric interpolation is applied, where the interpolation function attributed to $\xi^{[k]}$ is denoted by $I_x^{[k]}$. Defining the matrix

$$\boldsymbol{I}_t(\xi) = \underbrace{\left[\begin{array}{ccc|c|ccc} I_x^{[1]}(\xi) & \cdots & 0 & \cdots & I_x^{[k_{max}]}(\xi) & \cdots & 0 \\ \vdots & \ddots & \vdots & \cdots & \vdots & \ddots & \vdots \\ 0 & \cdots & I_x^{[1]}(\xi) & \cdots & 0 & \cdots & I_x^{[k_{max}]}(\xi) \end{array}\right]}_{m_t \times (m_t k_{max})}, \tag{3.32}$$

consisting of k_{max} $m_t \times m_t$-diagonal-blocks and furthermore the two vectors

$$\boldsymbol{X}^i = \left[(\boldsymbol{X}^{i[1]})^T \cdots (\boldsymbol{X}^{i[k_{max}]})^T\right]^T, \tag{3.33a}$$

$$\boldsymbol{\Theta}^i = \left[(\boldsymbol{\Theta}^{i[1]})^T \cdots (\boldsymbol{\Theta}^{i[k_{max}]})^T\right]^T, \tag{3.33b}$$

the function $\boldsymbol{x}$ can be approximated at t^i by the interpolation

$$\boldsymbol{x}^i(\xi) \approx \boldsymbol{I}_t(\xi)\boldsymbol{X}^i. \tag{3.34}$$

Whereas in two dimensions rotation variables can be handled similarly easily as position variables, the situation in three dimensions is much more difficult. A series of articles has been published in the last decades on how rotations in three dimensions can be interpolated. In [77] four principal ideas were distinguished how to perform the interpolation of the rotation variables. Although these four concepts are clearly different from each other and also from the way rotations are usually dealt with in two dimensions, they yet have in common two essential points both with each other and with commonly used concepts for the two dimensional case:

(I) At any point ξ, an approximation $\boldsymbol{\theta}^i$ of the rotation field $\boldsymbol{\theta}$ at t^i can be computed from the nodal rotation values $\boldsymbol{\Theta}^i$ if $\boldsymbol{\theta}^{i-1}$ and $\boldsymbol{\Theta}^{i-1}$ are known for t^{i-1}.

(II) The variation $\delta\boldsymbol{\theta}^i$ of the approximated rotation variable field can be related to the variation $\delta\boldsymbol{\Theta}^i$ of the nodal rotation values by an $m_r \times (m_r k_{max})$ interpolation function matrix $\boldsymbol{I}_r(\xi)$, which in analogy to (3.34) allows for writing

$$\delta\boldsymbol{\theta}^i(\xi) = \boldsymbol{I}_r(\xi, \boldsymbol{\theta}, \boldsymbol{x})\delta\boldsymbol{\Theta}^i. \tag{3.35}$$

In the following, we will abstain from any detailed discussion of different beam element formulations in two and three dimensions and rather resort only to the above two properties (I) and (II) shared by all beam elements known to the author. For a finite element formulation, we have to be able to compute the residual of the discretized weak form of the equation of motion on the basis of known nodal values and – in case that an implicit time integration scheme is used – to compute the variation of this residual with respect to the nodal degrees of freedom. For the computation of the residual we will exploit (I), whereas (II) is required only for the computation of the variation of the residual as pointed out in appendix A.5.

To compute the residual, first a backward Euler scheme is applied to approximate the translational velocity field $\dot{\boldsymbol{x}}$ at t^i by

$$\dot{\boldsymbol{x}}^i(\xi) \approx \frac{\boldsymbol{x}^i(\xi) - \boldsymbol{x}^{i-1}(\xi)}{\Delta t} \approx \boldsymbol{I}_t(\xi)\frac{\boldsymbol{X}^i - \boldsymbol{X}^{i-1}}{\Delta t}, \tag{3.36}$$

and of the rotational velocity field by

$$\dot{\boldsymbol{\theta}}^i(\xi) \approx \frac{\Delta\boldsymbol{\theta}^i(\xi)}{\Delta t}. \tag{3.37}$$

with

$$\Delta\boldsymbol{R}^i\left(\Delta\boldsymbol{\theta}^i\right) = \boldsymbol{R}\left(\boldsymbol{\theta}^i\right) \cdot \boldsymbol{R}\left(\boldsymbol{\theta}^{i-1}\right)^{-1}. \tag{3.38}$$

Here the rotation matrix corresponding to $\Delta\boldsymbol{\theta}^i$ is denoted by $\Delta\boldsymbol{R}^i$. The definition of the angular velocity by (3.37) and (3.38) is valid in both two and three dimensions, however, in two dimensions these equations can be simplified owing to the additivity of the rotation variables to $\dot{\boldsymbol{\theta}}^i \approx \left(\boldsymbol{\theta}^i - \boldsymbol{\theta}^{i-1}\right)/\Delta t$. Note that (3.34) and (I) guarantee that all quantities in (3.36) and (3.37) can be computed on the basis of the current nodal values and the information from the last time step. The unknown nodal values $\boldsymbol{X}^i$ and $\boldsymbol{\Theta}^i$ in a finite element scheme are determined by means of $(m_t + m_r)k_{max}$ linearly independent equations gained from (3.30) by using k_{max} different weighting functions $W_t^{[1]}, \dots, W_t^{[k_{max}]}$ and $W_r^{[1]}, \dots, W_r^{[k_{max}]}$, respectively. In practice $W_t^{[k]}$, $W_r^{[k]}$ are typically chosen equal to the translation interpolation function $I^{[k]}$, which itself is typically chosen to be a Lagrange polynomial function. In the following we will assume that all weighting functions as well the interpolation function matrix $\boldsymbol{I}_t(\xi)$ do not depend on the current configuration of the beam, whereas for the rotation interpolation function matrix $\boldsymbol{I}_r(\xi, \boldsymbol{\theta}, \boldsymbol{x})$ we explicitly allow such a dependence. Defining

$$\boldsymbol{W}_t(\xi) = \underbrace{\left[\begin{array}{ccc|c|ccc} W_t^{[1]}(\xi) & \cdots & 0 & \cdots & W_t^{[k_{max}]}(\xi) & \cdots & 0 \\ \vdots & \ddots & \vdots & \cdots & \vdots & \ddots & \vdots \\ 0 & \cdots & W_t^{[1]}(\xi) & \cdots & 0 & \cdots & W_t^{[k_{max}]}(\xi) \end{array}\right]^T}_{m_t \times (m_t k_{max})}, \tag{3.39}$$

$$\boldsymbol{W}_r(\xi) = \underbrace{\left[\begin{array}{ccc|c|ccc} W_r^{[1]}(\xi) & \cdots & 0 & \cdots & W_r^{[k_{max}]}(\xi) & \cdots & 0 \\ \vdots & \ddots & \vdots & \cdots & \vdots & \ddots & \vdots \\ 0 & \cdots & W_r^{[1]}(\xi) & \cdots & 0 & \cdots & W_r^{[k_{max}]}(\xi) \end{array}\right]^T}_{m_r \times (m_r k_{max})}, \tag{3.40}$$

$$\begin{aligned}
\boldsymbol{F}^i_{el} &= -\int_0^L \boldsymbol{W}_t'\boldsymbol{f}^i_s d\xi, & \boldsymbol{F}^i_{visc} &= \int_0^L \boldsymbol{W}_t\boldsymbol{f}^i_{visc} d\xi, \\
\boldsymbol{F}^i_{stoch} &= \int_0^L \boldsymbol{W}_t\boldsymbol{f}^i_{stoch} d\xi, & \boldsymbol{F}^i_{ext} &= \int_0^L \boldsymbol{W}_t\boldsymbol{f}^i_{ext} d\xi + \left[\boldsymbol{W}_t\boldsymbol{f}^i_{bd}\right]_0^L, \\
\boldsymbol{M}^i_{el} &= -\int_0^L \boldsymbol{W}_r'\boldsymbol{m}^i_s d\xi, & \boldsymbol{M}^i_{visc} &= \int_0^L \boldsymbol{W}_r\boldsymbol{m}^i_{visc} d\xi, \\
\boldsymbol{M}^i_{stoch} &= \int_0^L \boldsymbol{W}_r\boldsymbol{m}^i_{stoch} d\xi & \boldsymbol{M}^i_{ext} &= \int_0^L \boldsymbol{W}_r\boldsymbol{m}^i_{ext} d\xi + \left[\boldsymbol{W}_r\boldsymbol{m}^i_{bd}\right]_0^L, \\
\boldsymbol{M}^i_q &= \int_0^L \boldsymbol{W}_r(\boldsymbol{x}^i)'\times\boldsymbol{f}^i_s d\xi,
\end{aligned} \tag{3.41}$$

the resulting equation system can be written as

$$\boldsymbol{F}^i_{el} + \boldsymbol{F}^i_{visc} = \boldsymbol{F}^i_{ext} + \boldsymbol{F}^i_{stoch}, \tag{3.42a}$$

$$\boldsymbol{M}^i_{el} + \boldsymbol{M}^i_{visc} = \boldsymbol{M}^i_{ext} + \boldsymbol{M}^i_{stoch} + \boldsymbol{M}^i_q. \tag{3.42b}$$

Note that the forces and moments in (3.41) are evaluated just on the basis of approximations of $\boldsymbol{x}^i$, $\boldsymbol{\theta}^i$, $\dot{\boldsymbol{x}}^i$, $\dot{\boldsymbol{\theta}}^i$, which can always be computed by (3.34), (3.36), (3.37) and (I).

The computation of the discrete elastic and external forces and moments $\boldsymbol{F}^i_{el}$, $\boldsymbol{M}^i_q$, $\boldsymbol{M}^i_{el}$, $\boldsymbol{F}^i_{ext}$ and $\boldsymbol{M}^i_{ext}$ can be performed in a standard fashion dependent on the beam element formulation chosen so that we will not discuss it any further. Rather we will focus on the viscous and stochastic forces and moments, which make the difference between Brownian dynamics and ordinary macroscopic structural dynamics simulations.

3.2.2 Discrete viscous force and moment vectors

With (3.15a), (3.41) and (3.36), the discrete viscous force vector in (3.42) becomes

$$\boldsymbol{F}^i_{visc} = \int_0^L \boldsymbol{W}_t\boldsymbol{f}^i_{visc} d\xi = \int_0^L \boldsymbol{W}_t\boldsymbol{c}^i_t\boldsymbol{I}_t d\xi \frac{\boldsymbol{X}^i - \boldsymbol{X}^{i-1}}{\Delta t} =: \boldsymbol{C}^i_t \frac{\boldsymbol{X}^i - \boldsymbol{X}^{i-1}}{\Delta t}, \tag{3.43}$$

where $\boldsymbol{C}^i_t$ is the discrete translational damping matrix at t^i. Similarly, for the viscous damping moment we get

$$\boldsymbol{M}^i_{visc} = \int_0^L \boldsymbol{W}_r\boldsymbol{m}^i_{visc} d\xi = \int_0^L \boldsymbol{W}_r\boldsymbol{c}^i_r \frac{\Delta\boldsymbol{\theta}^i}{\Delta t} d\xi. \tag{3.44}$$

Note that $\boldsymbol{m}_{visc}$ and hence also $\boldsymbol{M}^i_{visc}$ are zero in two dimensions if (3.25) or (3.26) are employed as then $\gamma_{r\perp} = 0$.

3.2.3 Discrete stochastic force and moment vectors

3.2.3.1 Computation

The discrete stochastic force vector is given by

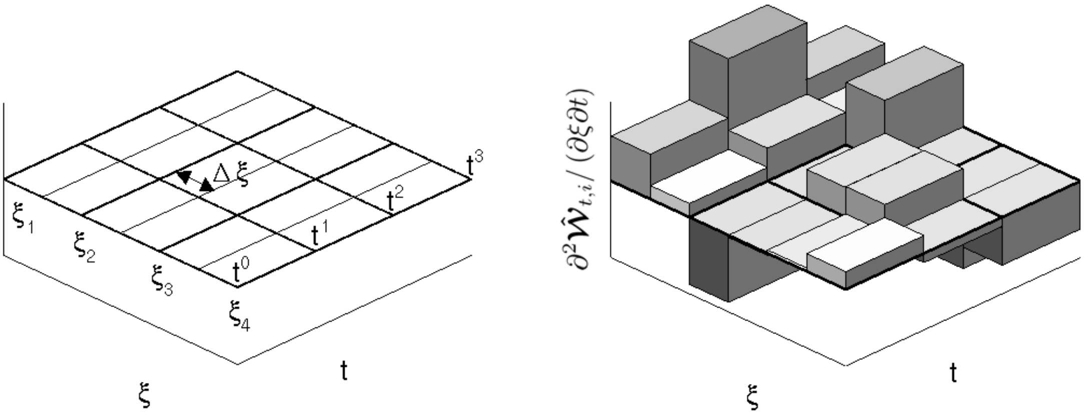

Figure 3.3: Subdivision of domain into rectangles of length $\Delta\xi$ in space and Δt in time (left); i-th component of white noise approximation $\hat{\mathcal{W}}_t$ constant on these rectangles, respectively (right)[6]

$$\boldsymbol{F}^i_{stoch} = \int_0^L \boldsymbol{W}_t \boldsymbol{f}^i_{stoch} d\xi = \sqrt{2k_BT} \int_0^L \boldsymbol{W}_t \boldsymbol{s}^i_t \frac{\partial^2 \mathcal{W}_t(\xi, t^i)}{\partial\xi\partial t} d\xi. \tag{3.45}$$

As this is a stochastic integral, the rules of deterministic calculus and especially the common rules of numerical quadrature cannot be applied in general. In practice, it is convenient replacing for its computation the space-time white noise by an approximation with mathematically more convenient properties. According to Lemma 2.3 of [3] and section 4.2 of [91], under fairly general conditions the order of magnitude of the error of a numerical method does not change if the white noise in (3.45) is replaced by the approximation

$$\frac{\partial^2 \hat{\mathcal{W}}_t(\xi, t)}{\partial\xi\partial t} = \sum_i \sum_k \frac{\chi^{i(k)}(\xi, t)}{\Delta t \Delta\xi} \int_{t^i}^{t^{i+1}} \int_{\xi^k}^{\xi^{k+1}} d\mathcal{W}_t(\xi, t), \tag{3.46}$$

with the characteristic function

$$\chi^{i(k)}(\xi, t) = \begin{cases} 1 & \text{if } \xi \in [k\Delta\xi; (k+1)\Delta\xi[\text{ and } t \in [t^i; t^{i+1}[\\ 0 & \text{else} \end{cases} \tag{3.47}$$

and $0 < \Delta\xi \leq h$, $0 \leq k \leq L/\Delta\xi - 1$, $0 \leq i \leq i_{max} - 1$. This white noise approximation is a random process piecewise constant on the rectangular subdomains $[t^i; t^{i+1}[\times [k\Delta\xi; (k+1)\Delta\xi[$. There it is given by random numbers with zero mean value and variance $\frac{1}{\Delta t \Delta\xi}$. Fig. 3.3 illustrates the case that $\Delta\xi$, which is the discretization length for the white noise, equals exactly half the finite element discretization length h .

In recent mathematical literature, often $\Delta\xi = h$ is chosen [3, 91]. However, for reasons discussesd below, we employ another $\Delta\xi$ here. We choose a finite $\Delta\xi$ which is small enough so that the following equations are true with a negligible numerical error:

---

[6] Reprinted Fig. with permission (and minor changes in notation) from [29]. ©2010 by the American Physical Society

$$\sum_k \left(\boldsymbol{W}_t \boldsymbol{s}_t^i\right)_{\xi=k\Delta\xi} \Delta\xi \approx \int_0^L \boldsymbol{W}_t(\xi)\boldsymbol{s}_t^i(\xi)d\xi. \tag{3.48a}$$

$$\sum_k \left(\boldsymbol{W}_t \boldsymbol{c}_t^i \boldsymbol{I}_t\right)_{\xi=k\Delta\xi} \Delta\xi \approx \int_0^L \boldsymbol{W}_t(\xi)\boldsymbol{c}_t^i(\xi)\boldsymbol{I}_t(\xi)d\xi. \tag{3.48b}$$

Denoting by $(.)^{\otimes 2}$ the tensor product of a vector $(.)$ with itself, an immediate consequence of (3.48) is

$$\begin{aligned}
&\langle \boldsymbol{F}_{stoch} \otimes \boldsymbol{F}_{stoch} \rangle = \left\langle \boldsymbol{F}_{stoch}^{\otimes 2} \right\rangle = 2k_B T \left\langle \left(\int_0^L \boldsymbol{W}_t \boldsymbol{s}_t \frac{\partial^2 \hat{\boldsymbol{\mathcal{W}}}_t}{\partial\xi\partial t} d\xi \right)^{\otimes 2} \right\rangle \approx \\
&2k_B T \left\langle \left(\sum_k \boldsymbol{W}_t(k\Delta\xi)\boldsymbol{s}_t(k\Delta\xi) \frac{\partial^2 \hat{\boldsymbol{\mathcal{W}}}_t(k\Delta\xi)}{\partial\xi\partial t} \Delta\xi \right)^{\otimes 2} \right\rangle = \\
&\frac{2k_B T}{\Delta t} \sum_k \boldsymbol{W}_t(k\Delta\xi)\boldsymbol{s}_t(k\Delta\xi)\boldsymbol{s}_t^T(k\Delta\xi)\boldsymbol{W}_t^T(k\Delta\xi)\Delta\xi \approx \\
&\frac{2k_B T}{\Delta t} \int_0^L \boldsymbol{W}_t \boldsymbol{s}_t \boldsymbol{s}_t^T \boldsymbol{W}_t^T d\xi = \frac{2k_B T}{\Delta t} \int_0^L \boldsymbol{W}_t \boldsymbol{c}_t \boldsymbol{W}_t^T d\xi.
\end{aligned} \tag{3.49}$$

In this derivation, we applied the pairwise independence of values of $\frac{\partial^2 \hat{\boldsymbol{\mathcal{W}}}_t}{\partial\xi\partial t}$ on distinct space intervals of length $\Delta\xi$ and the relation $\left\langle \frac{\partial^2 \hat{\boldsymbol{\mathcal{W}}}_t}{\partial\xi\partial t} \otimes \frac{\partial^2 \hat{\boldsymbol{\mathcal{W}}}_t}{\partial\xi\partial t} \right\rangle = \frac{1}{\Delta t \Delta\xi}\boldsymbol{1}$. The discrete stochastic force vector is a vector of Gaussian random numbers and thus uniquely characterized by its zero mean value and the covariance matrix (3.49). An elementary calculation analogous to the one shown in (3.49) reveals that

$$\boldsymbol{F}_{stoch}^i \approx \sum_{IP} \sqrt{\frac{2k_B T w_{IP}}{\Delta t}} \boldsymbol{W}_t(\xi_{IP})\boldsymbol{s}_t^i(\xi_{IP})\boldsymbol{\mathcal{Z}}_{IP}(0,1) \tag{3.50}$$

satisfies these properties if $\boldsymbol{\mathcal{Z}}_{IP}(0,1)$ is a vector of Gaussian random numbers with zero mean and unit variance and ξ_{IP} and w_{IP} denote the integration points and weights of some numerical quadrature method sufficient for the quadrature of the integrand in the end of (3.49) with negligible error. For example, ξ_{IP} and w_{IP} may be the integration points and weights of ordinary Gauss quadrature as typically employed in finite element programs. Thus, despite the significant mathematical complexity of the stochastic integral in (3.45), in practice it can be handled almost the same way and at the same computational cost as ordinary deterministic integrals arising in finite element computations. It is underlined that in (3.50) the spatial discretization length $\Delta\xi$ of the white noise appears no longer so that in fact it has never to be specified explicitly, but rather it just has to be assumed to be small enough to satisy (3.48).

The stochastic moment vector can be computed similarly to the stochastic force vector by

$$\boldsymbol{M}_{stoch}^i = \int_0^L \boldsymbol{W}_r \boldsymbol{m}_{stoch}^i d\xi = \sqrt{2k_B T} \int_0^L \boldsymbol{W}_r \boldsymbol{s}_r^i \frac{\partial^2 \boldsymbol{\mathcal{W}}_r(\xi,t)}{\partial\xi\partial t} d\xi, \tag{3.51}$$

and in practice it may be evaluated conveniently by

$$\boldsymbol{M}^i_{stoch} \approx \sum_{IP} \sqrt{\frac{2k_B T w_{IP}}{\Delta t}} \boldsymbol{W}_r(\xi_{IP}) \boldsymbol{s}^i_r(\xi_{IP}) \boldsymbol{\mathcal{Z}}_{IP}(0,1). \tag{3.52}$$

Note that $\boldsymbol{m}_{stoch}$ and hence also $\boldsymbol{M}^i_{stoch}$ are zero in two dimensions if (3.25) or (3.26) are employed as then $\gamma_{r\perp} = 0$.

3.2.3.2 Important properties

Having pointed out how to compute the discrete stochastic force and moment vectors in practice, it seems worth shedding light on some of their properties. The friction model introduced in section 3.1.2 was derived from the requirement that friction of a rigid, straight rod should be captured correctly. An important question is therefore whether and when a finite element method complying with this requirement captures also diffusion of such a structure correctly. To answer this question, we consider a rod and define $\bar{m}_{stoch\perp}$ as the total stochastic moment orthogonal to the rod-axis following from the discrete stochastic force and moment vectors, $\bar{m}_{stoch\|}$ as its counterpart parallel to the rod-axis, $\bar{f}_{stoch\|}$ as its force counterpart parallel to the rod axis and $\bar{f}_{stoch\perp}$ as its force counterpart orthogonal to the rod axis. Note that these variables are defined as scalar values. Furthermore, we assume that the weighting functions $W_t^{[k]}$ and $W_r^{[k]}$ in the weighting function matrices satisfy a partition of unity property, which is the case if, e.g., ordinary Lagrange polynomials are used. Since during free diffusion stochastic and viscous forces and moments are in equilibrium, we can write then the mean square of the rotation increment $\Delta\theta_{c\|}$ around the rod axis in one time step as

$$\left\langle \Delta^2\theta_{c\|} \right\rangle = \frac{\left\langle \bar{m}^2_{stoch\|} \right\rangle \Delta^2 t}{\zeta^2_{r\|}} = \frac{\Delta^2 t \left\langle \left| \int_0^L \sqrt{2k_B T \gamma_{r\|}} \frac{\partial^2 \hat{\mathcal{W}}_{r\|}}{\partial\xi\partial t} d\xi \right|^2 \right\rangle}{\zeta^2_{r\|}} =$$

$$= \frac{2k_B T \gamma_{r\|} \Delta^2 t}{\zeta^2_{r\|}} \left\langle \left(\int_0^L \frac{\partial^2 \hat{\mathcal{W}}_{r\|}}{\partial\xi\partial t} d\xi \right)^2 \right\rangle = \frac{2k_B T \gamma_{r\|} \Delta^2 t}{\zeta^2_{r\|}} \frac{L}{\Delta t} = \frac{2k_B T \Delta t}{\zeta_{r\|}} \tag{3.53}$$

where $\hat{\mathcal{W}}_{r\|}$ is a piece-wise constant approximation to the scalar component of the Wiener process $\boldsymbol{\mathcal{W}}_r$ in direction of the rod axis. Note that in the penultimate transformation step, the same idea was applied as in the transformations in (3.49), but that to this end not even property (3.48) was required as the integrand was just the white noise itself. Comparison of (3.53) with (B.10) and (B.11) reveals that diffusion around the rod axis is captured correctly by the finite element model regardless of the discretization length h. Similarly, one calculates for the expected square translation at the rod center

$$\left\langle \Delta^2 x_c \right\rangle = \left\langle \Delta^2 x_{c\|} \right\rangle + \left\langle \Delta^2 x_{c\perp} \right\rangle = \frac{\left\langle \bar{f}^2_{stoch\|} \right\rangle \Delta^2 t}{\zeta^2_{\|}} + \frac{\left\langle \bar{f}^2_{stoch\perp} \right\rangle \Delta^2 t}{\zeta^2_{\perp}} = 2k_B T \Delta t \left(\frac{1}{\zeta_{t\|}} + \frac{m_t - 1}{\zeta_{t\perp}} \right). \tag{3.54}$$

Here we applied the same steps as in (3.53), but separately parallel and perpendicular to the rod axis and in view of the fact that $(m_t - 1)$ independent stochastic components are acting perpendicular to the rod axis. Comparison of (3.54) with (B.10) and (B.11) reveals that also translational diffusion of a rod is captured correctly. The situation is slightly more difficult in case of the orthogonal rotational diffusion for which we can write

$$
\begin{aligned}
\left\langle \Delta^2 \theta_{c\perp} \right\rangle = \frac{\langle \bar{m}^2_{stoch\perp} \rangle \, \Delta^2 t}{\zeta^2_{r\perp}} = \frac{(m_t - 1)\Delta^2 t \left\langle \left| \int_0^L \sqrt{2k_B T \gamma_{r\perp}} \frac{\partial^2 \hat{\mathcal{W}}_{r\perp}}{\partial \xi \partial t} d\xi \right|^2 \right\rangle}{\zeta^2_{r\perp}} + \\
+ \frac{(m_t - 1)\Delta^2 t \left\langle \left| \int_0^L \sqrt{2k_B T \gamma_{t\perp}} \, |\boldsymbol{x}(\xi) - \boldsymbol{x}_c| \, \frac{\partial^2 \hat{\mathcal{W}}_{t\perp}}{\partial \xi \partial t} d\xi \right|^2 \right\rangle}{\zeta^2_{r\perp}} = \\
= 2k_B T \Delta t (m_t - 1) \left(\frac{L\gamma_{r\perp}}{\zeta^2_{r\perp}} + \frac{L^3 \gamma_{t\perp}/12}{\zeta^2_{r\perp}} \right) = \frac{2k_B T \Delta t (m_t - 1)}{\zeta_{r\perp}}.
\end{aligned}
\tag{3.55}
$$

Here $\hat{\mathcal{W}}_{r\perp}$ and $\hat{\mathcal{W}}_{t\perp}$ are the components of the Wiener processes $\mathcal{W}_r$ and $\mathcal{W}_t$ in one direction orthogonal to the rod axis. As there are $(m_t - 1)$ independent such components, the total expected square angle increment $\Delta^2\theta_{c\perp}$ orthogonal to the rod axis is $(m_t - 1)$ times the increment caused by only one such component. In the last transformation step, (3.24) was employed. With (B.10) and (B.11), (3.55) reveals that also orthogonal rotational diffusion is captured correctly by the finite element approach developed above. The significant difference between (3.55) on the one hand and (3.53) and (3.54) on the other hand is that in (3.55) one of the integrands is not only the white noise itself, but contains also the factor $|\boldsymbol{x}(\xi) - \boldsymbol{x}_c|$. In view of the isoparametric geometry interpolation, $|\boldsymbol{x}(\xi) - \boldsymbol{x}_c|$ can be considered in a simulation as a polynomial function of the same order as the interpolation functions $I_t^{[k]}$. Therefore the penultimate step in (3.55), which is analogous to what was done already in (3.49), requires a similar condition to the white noise discretization length as stated in (3.48). It can be conducted if and only if $\Delta\xi$ is chosen small enough for an almost exact Newton-Cotes integration of functions of the type I_t^2. As typically $W_t^{[k]} = I_t^{[k]}$ is chosen, this is guaranteed already by condition (3.48b). For $\Delta\xi = h$, however, which is suggested in many recent articles such as [3, 91], it is not satisfied in general. This means that for $\Delta\xi = h$, only translational and parallel rotational diffusion is captured correctly, but in general not orthogonal rotational diffusion. In opposition to that, the choice of $\Delta\xi$ proposed above, i.e., such that (3.48) is satisfied, makes sure that all types of translational and rotational diffusion are captured correctly.

The above proposed choice for $\Delta\xi$ has also another interesting property. Comparing (3.49) with the definition of $\boldsymbol{C}_t$ in (3.43) reveals that in case of $\boldsymbol{W}_x = \boldsymbol{I}_t$ the following discrete version of the fluctuation dissipation theorem is satisfied:

$$
\langle \boldsymbol{F}_{stoch} \otimes \boldsymbol{F}_{stoch} \rangle = \frac{2k_B T}{\Delta t} \boldsymbol{C}_t. \tag{3.56}
$$

The fact that only with a special white noise approximation and a special choice of weighting and interpolation functions such a discrete fluctuation dissipation theorem is satisfied, is especially interesting, because according to [3, 91] also numerical methods not satisfying such an equation are expected to converge to the correct solution as the discretization is refined in space and time. The satisfaction of an equation such as (3.56) is thus not mandatory for numerical methods in the field of BD - unlike often implicitly assumed in articles in the field of computational physics. However, as the satisfaction of (3.53), (3.54), and (3.55) on the one hand and of (3.56) on the other hand are closely connected to each other by condition (3.48), the satisfaction of such a discrete fluctuation-dissipation theorem may anyway be considered a favorable property giving rise to the hope for a good performance of a numerical method.

3.3 Discussion of Mathematical Background

In section 3.2, a finite element approach in space combined with a backward Euler scheme in time was introduced for the discretization of the SPDE (3.5). This discretization was introduced straight forward without discussing in detail the mathematical foundation of such a course of action. In the following two subsections, we will shed light on the mathematical background behind this discretization method.

3.3.1 Itō-Stratonovich-dilemma

It has long been known among physicists that diffusion processes can be modeled by stochastic differential equations (SDEs). Yet there has been considerable confusion since the late 1960s about the so-called Itō-Stratonovich-dilemma, which was debated even recently in several articles, e.g. [59, 60, 61]. As the understanding of this dilemma is crucial for the development of time integration schemes for BD simulations, we will briefly collect the most important facts about that dilemma and present them in a modern mathematical setting.

As pointed out in appendix A.3, the crucial difficulty of SDEs is their missing uniqueness without the definition of an integral convention. Decades ago this ambiguousness of stochastic integrals made people discuss whether the Itō or the Stratonovic convention is the right one for modeling BD in a physically correct manner. However, as shown in (A.20) Itō and Stratonovich equations can be transformed into each other by adding a correction to the drift term so that it is not a proper question asking which convention is the right one for modeling BD in general. Rather the proper question is: which convention has to be used to make an SPDE without any additional noise-induced drift term such as (3.5) model physics correctly. It has been pointed out several times and verified also experimentally in [60] that to this end the time derivative of the Wiener process in (3.5) has to be interpreted according to the right point convention (cf. appendix A.3) in case of a constant temperature T, which is assumed in this thesis. It is underlined that otherwise one may have to employ other conventions such as the Itō convention in case of constant friction tensors and a space dependent temperature field [70, 81]. At the first glance, one may wonder why not the Stratonovich convention has to be applied in these two cases although it is often considered the 'most physical' one. Precisely, according to the Wong-Zakai-theorem, it applies to any SDE derived from a deterministic one by simply considering the zero correlation time limit of the exciting forces. According to the argumentation in section 3.1.4, such a limit is underlying also to the model of the stochastic loads in (3.5). However, the actual starting point for the systematic derivation of (3.5) is an equation of motion with finite correlation time for the thermal excitation and a term capturing the small, but yet finite inertia of the rod [81]. From there, (3.5) is derived by considering the limit when both the time constant of the fast time scale of inertia and the correlation time of the thermal loads go to zero. This double limit process is not covered by the Wong-Zakai-theorem, and therefore the Stratonovich convention does not automatically apply to (3.5), but indeed rather the right-point convention does.

3.3.2 Discretization in time

The development of time integration schemes for SDEs is theoretically much more involved than for deterministic partial differential equations and still a field of vivid research [78, 87]. Owing to the complications of stochastic Taylor expansion as compared to deterministic Taylor expansion [57], especially higher order time integration schemes usually involve some intricate stochastic approximations and often go along with considerable computational effort. Furthermore, the limiting factor for time step size in the simulation of biopolymer networks is usually not the accuracy of the discretization in time, but rather the stiffness of the SPDEs, which drastically limits the time step size for explicit time integration schemes, and in practice also for implicit ones (cf. section 3.4.3). Therefore in the following, just simple one-step-θ time integration schemes will be discussed.

From the discussion in section 3.3.1 and appendix A.3, it follows immediately that interpreting (3.5) as a right-point SDE and applying a backward Euler scheme is most natural for BD simulations as this way any noise-induced drift term can be avoided. Indeed the application of any other one-step-θ scheme to (3.5) requires either a noise-induced drift term [40] or other special means such as a friction model with zero noise-induced drift term [33] or the evaluation of damping and noise terms at different points in time [40]. In addition to that, a backward Euler scheme exhibits favorable numerical stability properties important especially in view of the high stiffness of (3.5), which is caused by the high slenderness ratio of biopolymers going along with soft bending modes and stiff stretching modes.

Despite the obvious advantages of implicit time integration schemes for BD simulations, so far they are not used much for the simulation of biopolymers. Although a first implicit time integration scheme for BD simulations was already proposed in the late 1980’s by Fixman [35], such schemes have only rarely been applied so far. Actually, to the author’s experience a large number of researchers working on simulations for biopolymers is not even aware of the existence of such time integration schemes, but just always uses explicit Euler schemes. One important reason why implicit time integration schemes have not been propagated more resolutely so far is probably that they are more difficult to program than explicit Euler schemes and therefore avoided by those relying on completely self-written simulation codes, especially if simulated systems are small enough so that the computational cost with explicit Euler schemes is still acceptable. Another argument which may have delayed the propagation of implicit time integration schemes in BD simulations is of more theoretical nature: as discussed in chapter 9.8 of [57], fully implicit time integration schemes for SDEs, i.e., those where also the noise term is handled implicitly, are not unconditionally stable. This means that for example a fully implicit backward Euler scheme exhibits occasional instabilities even for a linear SDE and an arbitrarily small time step size. To understand this phenomenon, one should recall that implicit time integration requires the solution of an equation system. Numerical stability can be made sure thereby if and only if the solution is unique. To guarantee uniqueness, one usually needs to prove certain bounds never to be violated by certain quantities in the equation system, at least in the limit of small time steps. However, for the space-time white noise and therefore for the entries of the stochastic force and moment vectors no proper upper bounds can be found as even in the limit of arbitrarily small time steps there is a finite albeit perhaps only small probability that the space-time white noise surpasses any finite boundary. Consequently, a time integration scheme based on a simple implicit evaluation of the stochastic term is never unconditionally stable. This theoretical objection may be the second reason which has impeded the propagation of implicit time integration schemes for BD simulations. In practice, however, it typically does not matter for the simulation of biopolymers: although for a fully implicit Euler scheme no unconditional stability can be proven in a mathematically rigorous sense, the de-facto probability of such an instability can in practice be – depending on the numerical parameters – negligibly small. The discussion in chapter 9.8 of [57] reveals that the instability is caused by a singularity which causes problems in simulations only owing to the finite capacity of numerical software to deal with very small quantities. The computation of the exact probability for such problems is therefore not possible in general, because it is affected not only by machine precision itself, but also the algorithms used, e.g., for the solution of equation systems. However, according to [57] the thumb rule is: the smaller the amplitude of the white noise compared to the other terms in the system, the smaller the probability of instability. Stiffness of biopolymers is typically very high as compared to their stochastic excitation, which drastically limits the danger of numerical instability. Indeed in none of the numerous examples discussed in section 6, any stability problems of the fully implicit backward Euler scheme owing to their above discussed theoretical deficiency were ever observed. Thus this method represents a simple, efficient and stable time integration scheme for BD simulation of biopolymers, which actually often surpasses the performance of explicit Euler schemes in this field by far as will be demonstrated in section 6.

3.3.3 Discretization in space

The difficulties of stochastic time integration and the Itō-Stratonovich-dilemma have been discussed in a broader community of scientists already since the 1960s, often driven by the application of ordinary SDEs in mathematical models of diffusion processes. In opposition to that, the development of numerical methods for SPDEs is much a younger field, and only in the late 1990s first finite element methods for SPDEs were presented. The finite element approach for the BD of rod-like continua developed in the previous sections is based on the ideas presented in [3, 91]. However, it is emphasized that the proofs presented there cannot yet be considered a complete and rigorous mathematical foundation for this method for especially two reasons. First, (3.5) is a fully nonlinear SPDE, whereas the discussion in [3, 91] is limited to linear and semi-nonlinear SPDEs, respectively. To the author's knowledge no rigorous mathematical statements about the numerical analysis of general fully nonlinear SPDEs have been published so far. Second, we perform our discretization without paying major attention to the precise composition of the white-noise term hidden in the stochastic loads in the SPDE (3.5). However, it is underlined that the most general case discussed in [3, 91] is the one of a white-noise term depending on the values of the unknown function, but not on the values of its derivatives. As a consequence, only the friction model in (3.18) and (3.19) is covered by [3, 91], whereas the application of the alternative friction model (3.21) is justified only in a heuristic manner: careful numerical studies have not revealed any perceptible difference between the results of either model.

3.4 Implementation

This section is devoted to the implementation of the above simulation method for the BD of rod-like continua. In section 3.4.1, general requirements for the algorithms used are discussed and in section 3.4.2 and 3.4.3 it is shown how these requirements can be met in the two main parts of a simulation code, the finite element discretization in space and the time-stepping algorithm.

3.4.1 General requirements for algorithms

In order to understand the special requirements algorithms for BD simulations of rods have to satisfy, one has to remember three important properties of the SPDE to be solved in such simulations which are

(I) stochasticity,

(II) high stiffness,

(III) high nonlinearity.

The stochasticity is an obvious consequence of the white noise terms. The high stiffness simply originates from the large ratio between bending and stretching eigenfrequencies of thin rods resulting from the fact that the moment of inertia of area scales quartically with the rod radius and the cross section only quadratically. The least obvious one of the above three properties is the high nonlinearity. It can be understood immediately by a simple example: let a thin rod with two fixed ends be deformed from its straight initial configuration into a slightly curved one by a point force at the rod center perpendicular to the rod axis. In the straight initial configuration the rod's stiffness towards this deformation is determined by its bending stiffness only. However, with increasing displacement its axial stiffness increasingly contributes to the total stiffness towards this deformation. As discussed above, the axial stiffness is much larger than the bending stiffness so that its contribution changes the total stiffness significantly already for comparatively small deformations resulting in a highly nonlinear behaviour of the rod.

The above three properties of the SPDE to be solved result in three main requirements for the algorithms applied in BD simulations

(RI) high efficiency,

(RII) high stability for large numbers of time steps,

(RIII) high robustness to nonlinearities,

These requirements can be understood as follows: the total number of time steps in BD simulations of rods is typically very high for three reasons. First, time step size is typically small owing to the high stiffness of the underlying SPDE. This stiffness reduces the time step size not only for explicit time integration schemes, but usually also for implicit time integration schemes because standard methods for the solution of nonlinear equation systems, such as the Newton-Raphson method, have problems with the high nonlinearity of the equation system resulting in the end from the high stiffness of the differential equation. Second, time step size is typically smaller for SPDEs than for deterministic differential equations, because the order of strong convergence of time integration schemes for SPDEs is usually lower than the one for deterministic differential equations [57]. In case of a backward Euler scheme for example, the order of strong convergence is only a half, which again tends to reduce time step size and increase the total number of time steps. The third reason why the number of time steps in BD simulations is unusually high is the stochasticity of these simulations which increases the simulated span on time required in order to gain meaningful information about the simulated processes. Altogether the high number of time steps in BD simulations gives rise to the above requirements (RI) and (RII). Finally, (RIII) is just a natural consequence of (III).

3.4.2 Discretization in space

In principle, the above introduced simulation method is general enough to allow for a spatial discretization with any kind of nonlinear finite beam element. Yet, not all element formulations equally meet the requirements formulated in section 3.4.1. A comprehensive comparison between all two and three dimensional beam elements proposed so far in the literature would go far beyond the scope of this section. However, in the following we will briefly report strengthes and weaknesses of two element formulations in two and three dimensions, respectively.

In two dimensions, the Timoshenko and Reissner beam elements described in [21] were tested. Both were found to perform excellently in BD simulations with respect to the requirements (RI), (RII) and (RIII) discussed in section 3.4.1. No general problems or major difficulties were found during implementation and application of these elements to BD simulations.

In three dimensions, the non-additivity of the rotation variables complicates the situation. These variables are often stored as unit quaternions, and first of all it seems worth mentinoning that in this case the quaternions should be renormalized to unit absolute value in each time step in order to make sure that the quaternions do not loose this property after a large number of time steps. In [77], four types of nonlinear three dimensional beam elements are distinguished. Two of these types were tested in the examples described in section 6: the formulation proposed in section 17.2 of [22], which is a representative of type I in [77], and the one described in [23, 50], which is a representative of type II in [77]. The first formulation was found to be faster than the second one, but at the same time to suffer from a problem with the computation of curvature. In this thesis, beam elements of type I and II of the classification in [77] will be referred to in the following just as beam-I elements and beam-II elements. In beam-I elements, not the nodal rotation variables themselves are interpolated at the integration points in the element, but rather only the rotation increments. Mathemacially, this is much easier and faster, but it does not allow for an explicit computation of the curvature in a certain configuration. Rather curvature at a certain point in time has to be computed separately by an incremental update from the curvature in the preceeding time step. If simulations are conducted over a large number of time steps, this involves the risk that curvature and nodal rotation variables become inconsistent to each other. This effect was found in numerical experiments to be especially pronounced in case of freely fluctuating structures, where spinning motion of the structure about its own axis is limited only by the rotational damping coefficient $\gamma_{r\|}$. In such cases, beam-I elements were basically inapplicable in simulations over a large number of time steps. In opposition to that, beam-II elements, which can be implemented without any incremental curvature update, is found to be completely robust towards an increasing number of time steps. However, on the other hand the computational cost of the latter element formulation was found to be higher (cf. section 6.2.2) owing to the more sophisticated rotation interpolation. Thus in cases where the incremental curvature update does obviously not entail any numerical problems, beam-I elements may be preferred whereas in all other cases one should rely on other formulations such as beam-II elements.

3.4.3 Discretization in time

The extreme stiffness observed for SPDEs describing the Brownian motion of polymers often makes implicit time integration preferable over explicit time integration. For implicit time integration, one has to solve a nonlinear system of equations in each time step. In two dimensions, this is easily possible by means of Newton-Raphson iterations for either of the two beam element formulations mentioned in section (3.4.2). In three dimensions, however, Newton-Raphson iterations exhibit great problems. Ordinary Newton-Raphson iterations diverge sometimes already for a very small time step size. This problem was encountered only if rotations of the rods about their own axis are limited just by their axial damping and not, e.g., by some Dirichlet boundary condition. No detailed mathematical survey of the reasons for this problem has been conducted so far, however, the fact that increasing axial stiffness of the rod significantly exacerbates the problem leads to the following hypothesis: increasing axial stiffness makes the problem increasingly nonlinear. Iterative methods such as Newton-Raphson iterations which rely on linearizations, are therefore expected to explore more often configurations far from equilibrium entailing subsequent large iteration steps. In Reissner beam elements, position and rotation variables are intrinsically tied together so that large iteration steps always involve the risk of large changes of the rotation variables. Obviously, the size of reasonable steps is limited for the rotation variables by their 2π-periodicity, and it is plausible that the cricitcal step size is exceeded first and especially for the degree of freedom with the smallest damping, i.e., the rotations of the rod about its own axis. Thus increasing the axial stiffness increases the probability of too large iteration steps in the rotation variables especially if axial rotations are not tightly limited, e.g., by a Dirichlet condition. This results in an increased probability for numerical failure. So far, this hypothesis has not yet been verified rigorously. However, its plausibility was checked designing a remedy for the stability problems of Newton-Raphson iterations in three dimensions: if the hypothesis is correct, the problems of Newton-Raphson iterations have at least to diminish if during the iteration steps an artificial numerical damping is imposed to rotations of the rod. Indeed numerical experiments revealed that this is the case, which can be exploited the following way: during the iteration steps an artificial damping is imposed which decreases to zero over the iteration steps, as the system comes closer to equilibrium and the size of the steps decreases so that also the risk of numerical failure decreases. Thus, one can increase numerical stability also for large time steps and yet obtain in the end of each time step the correct solution. This strategy is known in the literature as pseudo-transient continuation (PTC): in [36] it was shown that the time step size can often be increased in problems of nonlinear elasticity if artificial diagonal entries are added to the tangent stiffness matrix in each step of the iterative solution of the nonlinear system of equations. The absolute value of these entries is decreased to zero over the iteration steps so that finally yet the exact solution can be achieved. PTC as outlined in [36] is suitable for translational degrees of freedom only. Thus its application to BD simulations with nonlinear beam elements first requires a generalization to rotational degrees of freedom accounting for the non-additivity of finite rotations. Performing such a generalization on a purely mathematical basis is intricate so that we rather resort to the physical intuition.

The contribution of a lumped mass or damping matrix to the tangent stiffness matrix consists of diagonal elements only. Thus the artificial diagonal entries applied in [36] can be physically interpreted as the consequence of some virtual damping force. Therefore a generalization of PTC for nonlinear beam elements may be performed by computing the tangent stiffness matrix in the j-th iteration step of the i-th time step as if there were some additional virtual damping force $\boldsymbol{f}_{PTC}^{i\{j\}}$ and moment $\boldsymbol{m}_{PTC}^{i\{j\}}$ in (3.5a) and (3.5b) with

$$\boldsymbol{f}_{PTC}^{i\{j\}} = \hat{c}_{PTC,t}^{i\{j\}} \dot{\boldsymbol{x}}^{i\{j\}} \tag{3.57a}$$

$$\boldsymbol{m}_{PTC}^{i\{j\}} = \hat{c}_{PTC,r}^{i\{j\}} \dot{\boldsymbol{\theta}}^{i\{j\}}. \tag{3.57b}$$

In general, the upper index $(.)^{i\{j\}}$ denotes in this thesis a quantity evaluated in the j-th iteration step of the i-th time step. The scalar values $\hat{c}_{PTC,t}^{i\{j\}}$ and $\hat{c}_{PTC,r}^{i\{j\}}$ are decreasing over the iteration steps to zero so that in the end the artificial stiffness added by the PTC method is zero. One could generalize (3.57) by replacing them by matrices, which would allow for an anisotropic artifical damping. However, different trials in this direction have not resulted so far in any perceptible improvement. Therefore this modification is not persued in the following, although it might be worth some more efforts in the future. Let $\Delta\boldsymbol{\theta}^{i\{j\}}$ be the rotation between the rotation $\boldsymbol{\theta}^{i-1}$ at the end of the last time step and the rotation $\boldsymbol{\theta}^{i\{j\}}$ in the j-th iteration step of the current time step (cf. (3.37)). Then virtual damping forces and moments as in (3.57) would go along in the j-th iteration step of the i-th time step with artificial translational and rotational stiffness matrices

$$\boldsymbol{K}_{PTC,t}^{i\{j\}} = \int_0^L \boldsymbol{W}_t c_{PTC,t}^{i\{j\}} \boldsymbol{I}_t d\xi, \tag{3.58a}$$

$$\boldsymbol{K}_{PTC,r}^{i\{j\}} = \int_0^L \boldsymbol{W}_r c_{PTC,r}^{i\{j\}} \boldsymbol{T}(\Delta\boldsymbol{\theta}^{i\{j\}}) \boldsymbol{I}_r d\xi. \tag{3.58b}$$

Here we substituted $c_{PTC,t}^{i\{j\}} := \hat{c}_{PTC,t}^{i\{j\}}/\Delta t$ and $c_{PTC,r}^{i\{j\}} := \hat{c}_{PTC,r}^{i\{j\}}/\Delta t$ and $\boldsymbol{T}$ is the inverse exponential map defined in (A.8). In our generalized PTC, $\boldsymbol{f}_{PTC}^{i\{j\}}$ and $\boldsymbol{m}_{PTC}^{i\{j\}}$ are not considered in the computation of the discrete force vectors; they are purely virtual quantities used just for the derivation of (3.58). However, the matrices $\boldsymbol{K}_{PTC,t}^{i\{j\}}$ and $\boldsymbol{K}_{PTC,r}^{i\{j\}}$ are assembled to the translational and rotational degrees of freedom in the tangent stiffness matrix, respectively. The numerical evaluation is performed by nodal integration resulting for the artificial translational damping into diagonal entries as already introduced in [36]. In opposition to that, $\boldsymbol{K}_{PTC,r}^{i\{j\}}$ is just a block-diagonal matrix as $\boldsymbol{T}(\Delta\boldsymbol{\theta}^{i\{j\}})$ is in general a dense matrix.

The decrease of the PTC damping values over the iteration steps can be computed similarly as already suggested in [36], i.e., by

$$c_{PTC,t}^{i\{j\}} = \left(\frac{\mathcal{R}^{i\{j\}}}{\mathcal{R}^{i\{j\}}} \right)^{\lambda_{PTC}} c_{PTC,t}^{i\{j\}} \tag{3.59a}$$

$$c_{PTC,r}^{i\{j\}} = \left(\frac{\mathcal{R}^{i\{j\}}}{\mathcal{R}^{i\{j\}}} \right)^{\lambda_{PTC}} c_{PTC,r}^{i\{j\}} \tag{3.59b}$$

with $j = \{2, 3, 4, \ldots\}$, some value $\lambda_{PTC} \in \mathbb{R}^+$ and the residual L_2-norm $\mathcal{R}^{i\{j\}}$ of the system of equations (3.42) in the j-th iteration step of the i-th time step. To additionally accelerate the method, $c_{PTC,t}^{i\{j\}}$ and $c_{PTC,r}^{i\{j\}}$ are set to zero as soon as $\mathcal{R}^{i\{j\}}$ has decreased to one percent of the predictor residual norm $\mathcal{R}^{i\{0\}}$. In [36] no systematic way has been proposed how to determine the PTC damping values in the first iteration step of each time step. In practice, it is convenient to choose in each time step the same values $c_{PTC,t}^{i\{1\}}$ and $c_{PTC,r}^{i\{1\}}$ in the first iteration step, respectively. These constant start values can be adjusted heuristically in the beginning of each simulation.

The above PTC scheme was found to improve efficiency of simulations in three dimensions outstandingly. For example, in simulations of actin bipolymers, it enabled a by several orders of magnitude larger time step size. Thus it is used in all three dimensions examples presented in section 6.

3.5 Summary

Section 3 can be summed up as follows: in a finite element approach to the BD of polymers, polymer elasticity can be dealt with in almost the same way as the elasticity of macroscopic beams and rods in structural engineering; the only difference is in fact that stiffness parameters such as bending stiffness should be modified in BD simulations by some ionic correction factor. In fact, there are only two major points where the simulation of micromechanical and macromechanical rods differ significantly: these are time integration and evaluation of the load vectors. For time integration, one has to consider in BD simulations that the equation of motion is only of first order in time due to the negligible inertia of polymers. Furthermore, only a backward Euler scheme can be applied straight forward for time integration. Other one-step-θ schemes in general require the computation of a noise induced drift term. In the evaluation of the load vectors, special attention has to be payed to the stochastic loads in BD simulations. However, whereas these stochastic loads are difficult to deal with theoretically, practically, they can be evaluated almost the same way as deterministic loads with a numerical quadrature scheme very similar to ordinary Gauss integration. This way, their calculation causes no significant additional computational cost. Furthermore, existing finite element codes can therefore be upgraded easily in order to account also for the Brownian dynamics of polymers. In many cases, to this end, only the computation of the viscous and stochastic force and moment vectors have to be programmed in addition to the already existing parts of the code.

4 Numerical Model of Linkers

4.1 General

For setting up a numerical model of linkers, some initial definitions are helpful. First of all, the distance between the two binding domains of a linker is assumed to range in the interval $[R_{cl} - \Delta R_{cl}; R_{cl} + \Delta R_{cl}]$. Here R_{cl} is the characteristic distance between the two binding domains and ΔR_{cl} a tolerance accounting for the fact that the actual distance between the binding domains may vary over time, e.g., owing to minor thermal fluctuations of the linker position, orientation and configuration. Values of R_{cl} are presented in Table 4.1 for several linkers common in biopolymer networks.

Crosslinker type	HMM	α-actinin	filamin	fascin	espin
R_{cl}	$40nm$	$40nm$	$98nm$	$5nm$	$5nm$
reference	[86]	[71]	[13]	[82]	[82]

Table 4.1: Biologically especially relevant crosslinker molecules, the characteristic distance R_{cl} they bridge, and references to more detailed information in the literature

The position of the point in the middle between the two binding domains is denoted by $\boldsymbol{x}_{cl,c}$. In general, the lower index $(.)_{cl}$ is reserved in this thesis to mark properties of linkers. Then linkers can be modeled in computer simulations depending on their current state as follows.

4.2 Free linkers

As discussed in section 2.3, for a free linker it is enough to keep track of its position in space so that it can be modeled as a point-like particle with position $\boldsymbol{x}_{cl,c}$ and friction coefficient ζ_{cl}. In general its equation of motion is then given by

$$\boldsymbol{f}_{visc,cl}(\boldsymbol{x}_{cl,c}, \dot{\boldsymbol{x}}_{cl,c}, t) = \boldsymbol{f}_{ext,cl}(\boldsymbol{x}_{cl,c}, t) + \boldsymbol{f}_{stoch,cl}(\boldsymbol{x}_{cl,c}, t), \tag{4.1}$$

where $\boldsymbol{f}_{visc,cl}$ is the viscous force the linker experiences moving through the background fluid, $\boldsymbol{f}_{ext,cl}$ is the sum of external deterministic forces the linker is subject to, e.g., as a consequence of force fields, and $\boldsymbol{f}_{stoch,cl}$ is the stochastic thermal force exerted by the thermal bath into which it is embedded. In a Newton-fluid, the viscous force is simply given by

$$\boldsymbol{f}_{visc,cl} = \zeta_{cl} \dot{\boldsymbol{x}}_{cl,c}, \tag{4.2}$$

and the stochastic force is then according to the fluctuation-dissipation theorem

$$\boldsymbol{f}_{stoch,cl} = \sqrt{2k_BT\zeta_{cl}}\dot{\boldsymbol{\mathcal{W}}}_{\boldsymbol{cl}}(t) \tag{4.3}$$

with the standard Wiener process $\boldsymbol{\mathcal{W}}_{cl}(t)$. For the computation of the position $\boldsymbol{x}_{cl,c}$, a simple backward Euler scheme can be applied to (4.1) in general. In the special case of a constant friction coefficient and negligible external deterministic forces, the position increment in a time step is just the respective increment of the Wiener process $\boldsymbol{\mathcal{W}}_{cl}(t)$ times a constant factor.

4.3 Singly bound linkers

The contribution of singly bound linkers to the polymer network is usually negligible so that it is enough keeping track of their position. Their position, however, is in opposition to the one of free linkers not governend by stochastic, thermal motion, but rather by the motion of the filament they are bound to. Thus we do not compute the position of singly bound linkers explicitly, but simply assume that they follow the binding site to which they are bound without affecting the dynamics of the filament on which this binding site is situated.

4.4 Doubly bound linkers

Doubly bound linkers form elastic and often rather stiff connections between two filament binding sites. Anyway, an extensional stiffness has to be attributed to this mechanical connection. Depending on whether experiments suggest either a finite or a negligible bending and torsion stiffness, doubly bound linkers are therefore represented by either finite beam elements or simple truss elements. The reference length of these elements may be set equal to the distance between the two filament binding sites connected by the linker at the point in time when the connection is established. In addition to that, so-called active linkers (motor proteins) may have an additional characteristic property which is the force or moment they can actively exert on the filaments they connect in order to shift or turn them against each other. This property of active linkers is well-known to play a key role in the rearrangement of the cytoskeleton during cell migration so that active linkers in general play an important role in cell biology. A variety of fundamental properties of biopolymer networks, however, can already be studied only by means of passive linkers. Therefore the focus of this thesis is limited for simplicity on the latter ones, leaving the issue of active linkers for future work.

4.5 Discussion

Using the above linker model in computer simulations, an important question is how to determine the numerical parameters such as the characteristic binding length R_{cl} or the stiffness of the linkers. There are in principle two ways how to determine these quantities: experimentally (e.g. [73]) or by MD simulations (e.g., [39, 58]). The considerable difficulties of single-molecule experiments on the one hand and the fast-growing power of computational methods on the other hand gives rise to the expectation that data gained by MD simulations will be especially relevant in the future.

Finally, it seems worth comparing the above linker model to previously published models. So far, mainly two linker models have been studied in the literature: in the first model [1, 49, 74] all filaments are connected by a linker as soon as they get close enough to each other. Motion and position of unbound linkers are not simulated explicitly. The number of linkers can be limited by some upper bound or left unlimited. In the second model [54, 55], also free and singly bound linkers are simulated.

The first way of modeling linkers can obviously not account for linker diffusion. As long as a certain maximal number of links has not yet been exceeded, linkers are just assumed to be available wherever filaments come close enough to each other to be connected. In reality, however, the motion and therefore also availability of linkers at a certain point in space is governed and also limited by thermal diffusion forces, kinematic constraints, which, e.g., prevent linkers from intersecting with filaments or other linkers, and sometimes also electrostatic potentials. In certain cases, one may not be interested in a detailed simulation of the interplay between these factors and then the first linker model is completely sufficient. However, a variety of highly important physical effects cannot be studied at all with this model: for example surveying the non-equilibrium thermodynamics of polymer networks usually requires a fairly accurate model of the dynamics of all main constituents of the network, especially of both the filaments and the linkers. Kinematic constraints delaying or even suppressing the motion of linkers may crucially affect the way filaments can interact with each other so that the computer simulation of non-equilibrium thermodynamics is in general impossible using the first linker model. In addition to that, also certain equilibrium effects go beyond the scope of that model: for example the attractive potential of filament binding sites necessary to make sure a certain number of crosslinks in the network can be determined by a computer simulation of that network only if the competition between linker binding energy and linker diffusion is simulated explicitly.

The linker model introduced in section 4 is obviously of the second type and offers therefore a powerful basis for the simulation of both equilibrium and non-equilibrium processes.

5 Numerical Model of Interactions between Filaments and Linkers

5.1 Chemical interactions

Filaments and linkers may interact with each other by chemical bonds which transmit forces and moments. In the following, we will assume that such bonds arise only between one filament and one linker, respectively. Direct chemical bonds between two filaments or two linkers will not be discussed as in biopolymer networks such bonds are typically assumed either not to arise at all or not to matter. It is emphasized, however, that the quantitative considerations below about bonds between one filament and one linker can be directly applied also to chemical bonds between two filaments or two linkers if this required in some special case in the future.

To form a chemical bond, a linker L and a free filament binding site F have to be sufficiently close to each other, i.e., the linker has to be within the so-called reaction volume V_{react} of the binding site. Once this is the case, both molecules can form a bond if they reach a proper relative position and orientation. In a very short time interval Δt, where the probability of multiple binding and unbinding events is negligible, this can be modeled by a Poisson process with a so-called on-rate $k_{react,on}$, and the probability for binding can be computed by

$$p_{on} = 1 - \exp\left(-k_{react,on}\Delta t\right). \tag{5.1}$$

Similarly, unbinding of a linker already bound to a filament happens with an off-rate $k_{react,off}$ and the probability

$$p_{off} = 1 - \exp\left(-k_{react,off}\Delta t\right). \tag{5.2}$$

In computer simulations based on the method introduced in the preceeding sections, filament and linker positions are known at each point in time. Thus for a numerical model of chemical interactions between filaments and linkers, one just has to define the position of the binding sites on the filaments and their respective reaction volume.

In principle, a binding site may be any point on the filament. In reality, binding sites are usually periodically distributed over filaments with a characteristic distance h_{bind}. If filaments are discretized with finite elements, the simplest way of modeling binding sites is setting the finite element discretization length h equal to h_{bind} and defining the finite element nodes as the binding sites of the filament. This allows for modeling doubly bound linkers just as finite beam or truss elements connecting two already existing nodes in the filament discretization. Indeed this simple model is employed in all the examples discussed in section 6.2. An avenue of future research may be the development of method allowing for chemical binding sites at arbirary points on the finite elements used for the mechanical discretization, for example by means of

Lagrange multipliers. This would allow for choosing h and h_{bind} independently and therefore for significant efficiency gains in many cases, because the distance between chemical binding sites on filaments is in practice often much smaller than the mechanical discretization length required.

Modeling the reaction volume is possible in various ways. In view of section 4, it seems reasonable assuming that free linkers can react with binding sites, if the distance between the linker center $\boldsymbol{x}_{cl,c}$ and the binding site ranges in the interval $[(R_{cl} - \Delta R_{cl})/2; (R_{cl} + \Delta R_{cl})/2]$. Singly bound linkers on the other hand can bind to another binding site only if the distance of this binding site and the one they are already attached to ranges in the interval $[R_{cl} - \Delta R_{cl}; R_{cl} + \Delta R_{cl}]$. By means of these two distance criteria one can decide whether a linker is in the reaction volume of a binding site. If so, the calculation of the binding probability between both is simply possible by (5.1) for a simulation time step of length Δt.

This model can be extended easily by additional geometric constraints refining the definition of the reaction volume. A comprehensive discussion of such constraints would go beyond the scope of this thesis, however, at least one example seems worth being discussed: it is well-known that certain types of linkers can connect only filaments in certain relative orientations. The linker fascin, e.g., can link only almost parallel filaments [19], whereas the linker alpha-actinin is flexible and rather insensitive towards the orientation of the linked filaments [19]. This can be modeled by a simple orientation constraint: singly bound linkers are assumed to be in the reaction volume of a free binding site only if the angle between the filament on which this binding site is situated and the filament to which the linker is already attached to ranges in the interval $[\phi - \Delta\phi; \phi + \Delta\phi]$. Here ϕ may be considered as preferred binding angle and $\Delta\phi$ as tolerance around it. The angle between the filaments can be computed in a finite element model either from the triads representing the cross section orientation of the filaments or alternatively from the tangents to the three dimensional curves representing their neutral lines. Both ways are expected to lead to almost identical results as shear deformation is usually negligible due to the high slenderness ratios of typical biopolymers.

For simulations, the parameters $k_{react,on}$ and $k_{react,off}$ have to be specified. Various data sources can be used to this end. The most important one are experiments such as presented in [38, 69] where the on- and off-rates k_{on} and k_{off} of the bimolecular reaction

$$L + F \underset{k_{off}}{\overset{k_{on}}{\rightleftharpoons}} LF \tag{5.3}$$

are determined. Here LF is the species of linkers bound to a filament binding site. Denoting the molar concentration of a species by [.], the number of binding and unbinding events per unit time and volume is given by definition of the on- and off-rates by $k_{on}[L][F]$ and $k_{off}[LF]$, respectively [46]. From the experimentally determined k_{on}, one can immediately compute the parameter $k_{react,on}$ required in simulations. In view of (5.1), the expected number of binding events per time and filament binding site is given by the on-rate $k_{react,on}$ times the number of linkers in the reaction volume of a certain binding site, which is $[L]V_{react}$. To get the total number of binding events per volume, one has to multiply this term with the concentration of filament binding sites per volume, i.e., with $[F]$, which leads to

$$k_{react,on}[L]V_{react}[F] = k_{on}[L][F] \tag{5.4}$$

and thus

$$k_{react,on} = k_{on}/V_{react}. \tag{5.5}$$

With

$$k_{react,off} = k_{off}, \tag{5.6}$$

simulation parameters can then directly be determined from the experimentally measured on- and off-rates of the bimolecular reaction (5.3). It is emphasized that in order to get a simulation parameter $k_{react,on}$ consistent to the experimentally measured k_{on}, not the real reaction volume is required in (5.5), but just the one used in the simulations.

In case that experimental results are available only for either k_{on} or k_{off}, the respective other rate constant can be computed according to [46] by

$$\frac{k_{react,on}}{k_{react,off}} = \exp\left(-\frac{\Delta G_{L+F\rightarrow LF}}{k_B T}\right) \tag{5.7}$$

if at least the binding energy $\Delta G_{L+F\rightarrow LF}$ is known. If no experimental data is available for a certain linker-filament combination, MD simulations are another data source for on- and off-rates or binding energies.

In the end of this section, it seems worth comparing the above model for chemical interactions between linkers and filaments with previously published ones and discussing possible extensions.

In [54, 55] a similar model for chemical interactions between filaments and linkers is proposed. There, however, chemical bonds are assumed not to form with some probability p_{on}, but rather always if the linker is in the reaction volume of the filament and both have the proper relative orientation. The definition of the proper relative orientation for the reaction to happen requires some geometric parameters and tolerances. These are hard to determine in practice by experiments or MD simulations, which is a serious drawback of this approach. Furthermore, this model assumes that motion of filaments and linkers can be simulated by a micromechanical model sufficiently exactly down to the length and time scale relevant for chemical reactions. In reality, however, chemical reactions often happen on much a faster time scale and are furthermore affected by geometric or electrostatic properties on much a smaller length scale than considered in a micromechanical model. These potential problems of the approach pursued in [54, 55] were the motivation for the development of a new numerical model for chemical interactions between linkers and filaments in this thesis whose parameters can be determined straight forward from experimental data and which does not require the precise resolution of any events on length and time scales relevant for the chemical reaction process itself.

In future work, especially three extensions for the model introduced in this thesis may form interesting avenues of research:

In reality, the probability of unbinding increases significantly according to Bell's formula [46], if a chemical bond is loaded by forces or moments. This effect is not captured by the above model, where bond life time is assumed not to depend on the load transmitted by the bond. Especially, for biopolymer networks in the nonlinear regime, this effect may play an important role so that an extension of the above model incorporating Bell's formula may be useful in the future. In practice, this is possible easily by making the off-rate for doubly bound linkers dependent on the their internal forces and moments according to Bell's formula.

Another important point is the position of the binding sites. Currently $h = h_{bind}$ is assumed, i.e., the mechanical discretization length is set equal to the chemical one. In practice, however, one may be interested in choosing different parameters for both. For example, actin filaments exhibit binding sites on every monomer, i.e., at a distance of $7nm$, whereas the length scale relevant for mechanical deformation is rather of the order of magnitude of the persistence length L_p, which is more than one thousand times longer. Thus for the simulation of actin, it is desirable choosing h and h_{bind} vastly different, which is impossible if chemical binding sites are equivalent to finite element nodes. A simple remedy would be allowing for the formation of chemical bonds also apart from the nodes of the finite element discretization. This can be realized easily and in a mathematically well-founded way for a finite element discretization of a continuum model by means of Lagrange multipliers tying the finite elements representing the linkers to the finite elements representing the filaments at arbitrary points. It is emphasized that for bead-spring models as used in [54, 55] similar methods could be employed for distinguishing between mechanical and chemical discretization length, but that the ad-hoc character of the bead-spring model is expected to be a significant obstacle on the way to a mathematically well-founded treatment of this issue.

A third fruitful avenue of future research might be the exploration of additional constraints for the definition of the reaction volume besides just distance and filament orientation. In reality, binding sites are situated on one side of the filament so that bonds to free linkers may be impossible if these are on the opposite side of the filament owing to the filament backbone forming a solid barrier between binding site and linker. This effect as well as geometric details of the position of the binding sites on the filaments depending on the filament type could be accounted for by advanced orientation constraints in the future. It is emphasized that already in [54, 55] it was tried to account for the geometry of the binding sites in a similarly detailed manner by means of a Frenet-Serret frame, but that the formalism developed there is actually mathematically incorrect in case of general deformation, because of the singularity of the Frenet-Serret frame for straight filaments. Detailed modeling of the geometry of filament binding sites distinguishing between different directions orthogonal to the filament backbone is indeed in general possible only by means of a filament discretization providing material triads such as a finite element discretization or an especially enriched bead-spring discretization [16, 17].

5.2 Contact interactions

Mechanical contact between filaments and linkers poses kinematic constraints to filament and linker motion which can be accounted for as usual in finite element simulations [95]. In the equations of motion (3.5) and (4.1), contact forces can be accounted for by deterministic external forces. As linkers are typically much smaller than filaments, the volume of free and singly bound linkers may either be neglected completely in contact computations or modeled as ball around the linker center or binding site to which the linker is attached. Doubly bound linkers are represented by beam elements and their volume can be accounted for in contact computations accordingly. If free and singly bound linkers are neglected, contact can be modeled exclusively as what is referred to in finite element textbooks and articles as beam contact. In principle, the methods described there can be directly applied to biopolymer networks. For this thesis, a common penalty and augmented Lagrange method for beam contact were tested. The tests confirmed the in principal suitability of these methods for simulations of biopolymer networks, but revealed at the same time several deficiencies of these algorithms. For example, the correct detection of contact and observation of the kinematic constraints imposed by contact interactions is not straightforward with standard algorithms: because of the high slenderness ratio of biopolymers (e.g., around 10^3 for actin), the deformation a filament segment experiences within one time step may be significantly larger than its diameter. Standard contact algorithms may therefore sometimes not even detect any contact if two filaments simply completely pass through each other within one time step without overlapping in any iteration step in between. The development of reliable and efficient remedies for such problems goes beyond the scope of this thesis, but is definitely a promising avenue of future research. Because of the above problems, in section 6 contact interactions are considered only in the performance comparison in section 6.2.2 in order to make the simulation conducted there comparable with the one presented in [55]. All other examples in this section are selected in such a way that the neglection of contact interactions – which are in physics textbooks and articles usually referred to as 'excluded volume effects' – is a physically reasonable simplification as is explained in the following:

In studies of single polymers, contact interactions play a role only if the polymer is flexible enough for self-contact. This is expected to be the case only for so-called flexible polymers whose length L is much larger than their persistence length L_p, whereas for semi-flexible polymers with $L \approx L_p$ and stiff polymers with $L << L_p$ self-contact is not expected. All single filament examples in section 6.1 deal with semi-flexible or stiff polymers so that the neglection of contact interactions is a reasonable simplification.

In the example in section 6.2.1, the viscoelasticity of biopolymer networks is examined in the small deformation regime. The networks studied there have a homogeneous-isotropic architecture without any spots with extraordinarily high filament or linker density so that there are only few points where filaments come close to each other. At the same time, the linker density and length are chosen high and large enough in order to make sure that at these points filaments typically form a crosslink over the distnace $R_{cl} = 0.1$ before they come close enought to each other for contact, which could happen only at a distance comparable to the filament diameter $d \approx 7\text{e}{-3}$. Therefore also in the example in section 6.2.1 the neglection of contact interactions seems justified for the time being.

Finally, for the equilibrium thermodynamics of networks consisting of (infinitesimally) thin filaments and linkers, contact interactions do interestingly not play any role at all: in thermodynamic equilibrium, the probability of a certain network configuration depends only on its free energy, and for infinitesimally thin filaments the difference between the free energy of a system with and without excluded volume effects is almost surely equal to zero. Thus simulations lead to the same result with and without excluded volume effects, but faster in the latter case, because the rearrangement of the network into some specific equilibrium architecture happens faster without the kinematic constraints imposed by contact interactions. Therefore the neglection of these interactions is not only justified for the example discussed in section 6.2.3, but even advisable.

This way, for all examples in 6 where contact is neglected, this can be justified physically. However, yet one should not forget that a variety of phenomena in biopolymer networks are crucially governed by contact interactions. Therefore the development of improved algorithms for a standard incorporation of contact mechanics in simulations of biopolymer networks is definitely an issue worth being addressed in the near future.

5.3 Long-range electrostatic interactions

Both filaments and linkers in biopolymer networks may exhibit an electric charge. For actin filaments, e.g., the linear charge density is $4e/nm$ [45]. This charge may on the one hand affect the effective stiffness of filaments as discussed in section 3.1.1. In more complex cases, it may on the other hand cause long-range interactions between different filaments and linkers or just different segments of one and the same filament or linker. Additionally, the electric charge may entail complex ionic patterns in the surrounding fluid shielding it partially.

A detailed model of electrostatic effects beyond just simple effective stiffnesses would go beyond the scope of this thesis, and for all examples presented in section 6, it is assumed that the effects of electrostatic charge can be captured with sufficient accuracy by effective stiffnesses only. The excellent agreement between experimental data and simulations conducted under this premise in section 6.1 gives an a posteriori justification of this assumption for single filaments. For biopolymer networks, the situation is more complicated. So far, no evidence has been presented that electrostatic forces play a major role for their mechanics ifself. However, diffusion of charged particles [67] through networks or the network architecture in the presence of certain linker types [8] may be significantly affected by electrostatic effects beyond just an altered filament stiffness. Therefore, for the time being and for the examples presented in 6, the incorporation of electrostatic effects by means of simple effective stiffnesses seems reasonable, but more detailed models are yet expected to be a fruitful field for future research.

6 Examples

In the following section, a series of examples will be presented for validation and verification of the above introduced approach for the simulation of biopolymer networks. To this end, first examples with single filaments and other rod-like continua immersed into a thermal bath are discussed in section 6.1. These can be considered as test cases for the theory developed in section 3. Then in section 6.2, results will be presented for the simulation of whole biopolymer networks on the basis of the theory developed in sections 3, 4 and 5. In this section, all numerical values are given in terms of the basis units micrometer, second, miligram and Kelvin if no other units are indicated explicitly. By default, temperature is set in the following examples to $T = 296.15$, thermal energy to $k_BT \approx 4.0889\text{e}{-3}$, which is equivalent to room temperature, fluid viscosity to $\eta = 1\text{e}{-3}$, which is equivalent to the one of water at room temperature, the fluid velocity fields to $\boldsymbol{v} = \mathbf{0}$ and $\boldsymbol{\omega} = \mathbf{0}$, and filament parameters are taken from appendix C. As PTC parameters in three dimensions $c^{i\{1\}}_{PTC,trans} = 0$, $c^{i\{1\}}_{PTC,rot} = 0.145$, and $\lambda_{PTC} = 6.0$ are chosen. In general, simulations start with straight filaments. Theories in polymer physics, however, often assume an equilibrated configuration as starting point, which is a configuration where filaments have already undergone a stochastic bending deformation characteristic for the respective temperature. For very short filaments such as considered in section 6.1.1.1 and section 6.1.2.1, this point can be neglected as these can be considered effectively as stiff rods. However, in all other examples simulation data is analyzed only after an initial equilibration time $\tau_{bend} \approx (\gamma_{t\perp}/EJ_2)(L/\pi)^4$, which is the characteristic time constant of the filament's slowest bending eigenmode and therefore the span on time filaments need to reach a configuration characteristic for thermal equilibrium.

6.1 Single Filaments and rod-like continua

6.1.1 Examples in two dimensions

6.1.1.1 Diffusion of short actin filaments

In [62] quasi-two-dimensional diffusion of short actin filaments of length L and diameter d in a narrow gap between two plates filled with an aqueous solution of viscosity $\eta = 0.89\text{e}{-3}$ is studied. The experimentally measured translational and rotational diffusion coefficients $D_{2D,t,exp}$ and $D_{2D,r,exp}$ are according to (B.13) in appendix B.1.4 expected to satisfy

$$D_{2D,t,exp} = \frac{k_BT\,[3ln(L/d) + 0.658]}{8\pi\eta_{t,exp}L} \tag{6.1a}$$

$$D_{2D,r,exp} = \frac{3k_BT\,[ln(L/d) - 0.447]}{\pi\eta_{r,exp}L^3} \tag{6.1b}$$

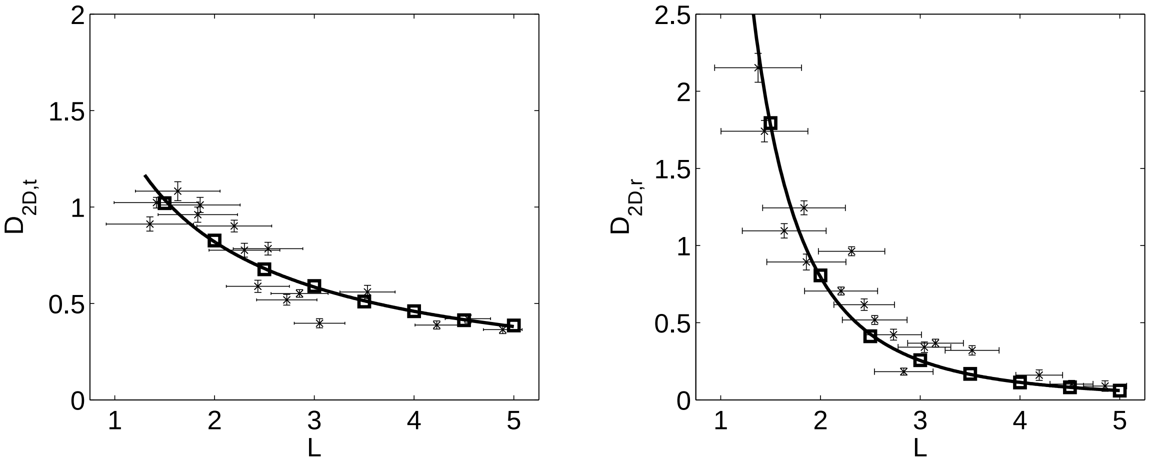

Figure 6.1: Translational (left) and rotational (right) diffusion coefficients gained by theory (continued line), simulation (squares) and experiment (crosses with error bars)[7]

with $\eta = \eta_{t,exp} = \eta_{r,exp}$. However, as discussed in [62], the 'apparent' viscosities $\eta_{t,exp}$ and $\eta_{r,exp}$ in the experiment do not satisfy the latter condition as the drag forces on the filaments deviate from the ones expected in an ideal two-dimensional setting owing to the finite size of the gap to which the polymers are confined. Therefore experimentally $\eta = 0.89\text{e}{-3}$, $\eta_{t,exp} = 1.71\text{e}{-3}$ and $\eta_{r,exp} = 3.11\text{e}{-3}$ are observed, where the latter two coefficients result from a least-mean-square fit of (6.1) to the measured diffusion coefficients presented in figure 3 in [62] (note that in [62] erroneously the numerical value $\eta_{r,exp} = 2.62\text{e}{-3}$ was given).

The diffusion experiment in [62] can be simulated determining the friction coefficients with (3.20) and (3.25) on the basis of the experimentally observed 'apparent' viscosities. This leads to

$$\gamma_{t\|} = \frac{4\pi}{(3ln(L/d) + 0.658)/\eta_{t,exp} - (ln(L/d) - 0.447)/\eta_{r,exp}}. \tag{6.2a}$$

$$\gamma_{t\perp} = \frac{4\pi\eta_{r,exp}}{ln(L/d) - 0.447}. \tag{6.2b}$$

Simulation time step size is set to $\Delta t = 5\text{e}{-4}$, and total simulation time to $t_{max} = 5$. Averaging the trajectories and rotations of filaments over ten thousand time steps, respectively, a translational and rotational diffusion coefficient can be determined using the average square displacement and rotation increments at the filament center within each time step and applying (B.10) from appendix B.1.3. Figure 6.1 compares the diffusion coefficients in the simulations with those according to (6.1a) and (6.1b) and the experimentally observed ones. Obviously, theoretical, experimental and computational results are in excellent agreement.

For these results, the filaments were discretized in the simulations with one single linear finite element only. Yet both the translational and rotational diffusion coefficient were captured correctly in the simulation for the reasons already discussed in section 3.2.3.2. The fact that elastic deformation can be captured by one single finite element only roughly is of minor importance

---

[7] Reprinted Fig. with permission (and modified axis labels) from [29]. ©2010 by the American Physical Society

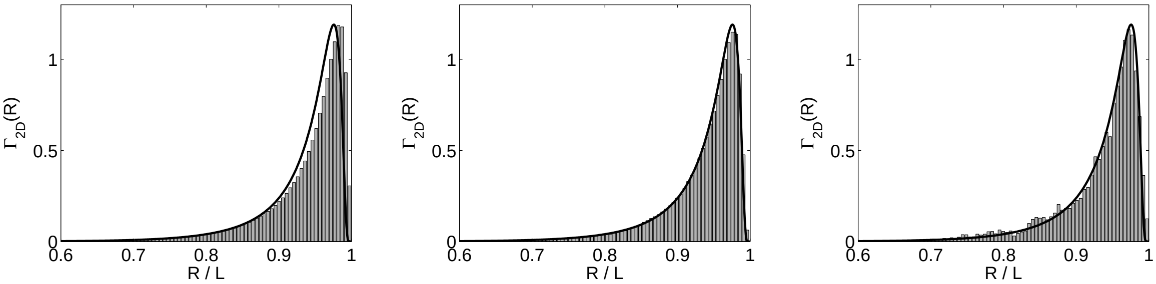

Figure 6.2: RDF gained from finite element simulation with $n_{ele} = 10$, $\Delta t = 1\text{e}{-3}$ (left) and $n_{ele} = 40$, $\Delta t = 1\text{e}{-4}$ (middle) compared with experimental data from [37] (right). The analytical solution according to (6.3) is represented by continued black lines, respectively, and simulation and experimental results are illustrated by the grey histrograms[8]

at this point since all actin filaments considered in the experiment in [62] are short enough to be modeled as quasi-rigid.

6.1.1.2 Radial distribution function of actin filaments with free ends

As a semiflexible polymer of contour length L undergoes thermal undulations due to its stochastic excitation in the thermal bath, its effective end-to-end distance $R(t)$ is practically always smaller than L and changes continuously. Obviously, different end-to-end distances arise with different probabilities. Their probability distribution is usually referred to as radial distribution function (RDF) and reads in two dimensions according to [93]

$$\mathcal{G}_{2D}(R) = \frac{1}{\mathcal{N}_{2D}} \sum_{n=0}^{\infty} \frac{(2n)! P_{3/2}\left(2\frac{n+0.25}{\sqrt{\mathcal{M}_{2D}(R)}}\right)}{(2^n n!)^2 \mathcal{M}_{2D}(R)^{5/4} \exp\left[\frac{(n+0.25)^2}{\mathcal{M}_{2D}(R)}\right]}, \tag{6.3}$$

where $P_{3/2}(.)$ is a parabolic cylinder function, $\mathcal{M}_{2D}(R) = 2(1-R/L)L_p/L$ with the persistence length $L_p = EJ_2/(k_B T)$, and $\mathcal{N}_{2D}$ ensures a normalized distribution. Equation (6.3) has been verified experimentally in [37] by an optical measurement of the frequency of occurence of different end-to-end distances for phalloidin-stabilized actin filaments of length $L = 13.4$ confined by two plates to quasi-two-dimensional motion. Defining the normalized RDF

$$\Gamma_{2D}(R) = \frac{\mathcal{G}_{2D}(R)R}{\int_{R=0}^{R=L} \mathcal{G}_{2D}(R)RdR}, \tag{6.4}$$

the experimental results of [37] are compared in Fig. 6.2 with the theoretical prediction according to (6.3) and with finite element simulations with $n_{ele} = 10$ and $n_{ele} = 40$ elements, respectively. Apparently, the simulation results excellently agree both with the theoretical prediction and the experiments already for $n_{ele} = 40$ elements and a time step size $\Delta t = 1\text{e}{-4}$.

---

[8] Reprinted Fig. with permission (and modified axis labels) from [28]. ©2009 by the American Physical Society

6.1.1.3 Tangent correlation function of actin filaments

Because of their stochastic loading, polymers undergo a continuous stochastic bending deformation. Assuming free boundaries at either end of the polymer, the variance of the stochastic bending moment increases from zero at $\xi = 0$ strictly with ξ. Therefore the correlation between the orientation of the tangent vector at $\xi = 0$ and some other point ξ decreases strictly with ξ. As shown in [46], this effect can be quantified by means of the so-called tangent correlation function $\vartheta(\xi)$, which is the mean value of the cosine of the angle between the polymer backbone at $\xi = 0$ and some other point ξ. The tangent correlation function can be computed in two dimensions analytically by

$$\vartheta_{2D}(\xi) = \langle \cos|\theta(\xi) - \theta(0)| \rangle = \exp\left(-\frac{\xi}{2L_p}\right) \tag{6.5}$$

where $\langle . \rangle$ denotes here as also in the following an ensemble average over an infinitely large ensemble of polymers, and $L_p = EJ_2/(k_B T)$ is the persistence length. In [37], this theoretical prediction was verified by an experiment with phalloidin-stabilized actin filaments confined by two plates to quasi-two-dimensional motion. The results of this experiment are compared in this section with simulations with two different friction models: in the first model, $\gamma_{t\|} = 2\pi\eta$ and $\gamma_{t\perp} = 4\pi\eta$ are chosen, which corresponds to the values given in appendix C. In the second model isotropic friction coefficients $\gamma_{t\perp} = \gamma_{t\|} = 4\pi\eta$ are applied so that all noise-induced drift terms are zero and no attention has to be paid to the issue of stochastic integral conventions. For both models the discrete damping matrix and stochastic force vector can be computed by means of different numerical quadrature rules. Gauss-Legendre quadrature leads to what is called in structural engineering a consistent damping matrix. Alternatively, one may employ for example nodal quadrature giving a lumped damping matrix [47]. One can easily show that for isotropic friction coefficients and linear finite elements nodal quadrature leads to exactly the same discrete damping matrix as applied in bead-spring simulations. An interesting consequence of this consideration is that the isotropic damping model used in bead-spring simulations can not only be derived by means of physical intuition, i.e., the idea that a polymer can be interpreted as a chain of small beads. Rather it can also be derived from a continuum model by means of luming techniques. The tangent correlation function (6.5) is obviously independent on the friction model. Indeed this is observed also in computer simulations where a consistent isotropic, a consistent anisotropic and a lumped isotropic damping matrix lead to the same results as shown in Figure 6.3 for polymers of length $L = 10$. Each polymer was discretized with 40 linear finite elements in space and time steps of the size $\Delta t = 1\mathrm{e}{-5}$. Simulation data from 90.000 and 12.000 equidistant sample points in time are averaged in the left and right plot of Figure 6.3, respectively. Between subsequent sample points in time the distance was $10^3\Delta t$. The increasing deviation of the simulation output from the analytical solution for increasing ξ in the right plot results from the increasing variance of the stochastic bending moment and disappears for larger numbers of sample points allowing for a better approximation of the mean value in (6.5). This can be seen for the case of an anisotropic consistent damping matrix by comparing the simulation results depicted in the left and right plot in Fig. 6.3. Altogether the agreement between simulation results, theoretical prediction and experimental data shown in this figure is remarkable.

The focus of this section does not lie on a discussion of the computational performance of the finite element method developed in this thesis. Yet some brief remarks about this issue are

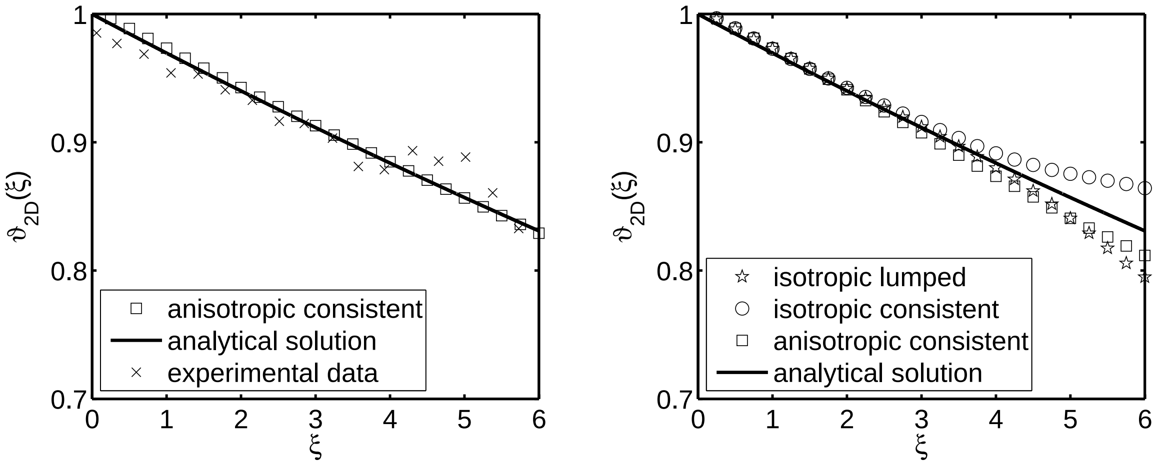

Figure 6.3: Comparison between simulation with anisotropic consistent friction model, analytical solution according to (6.5) and experimental data from [37] (left), comparison between simulations with isotropic lumped, isotropic consistent and anisotropic consistent damping matrix and analytical solution (6.5) (right)[9]

instructive. In explicit time integration schemes, which are at the moment most commonly used for bead-spring models, the time step size has to be smaller or equal to the smallest characteristic time constant in the system. In practice this is typically the time constant of the stretching eigenmode between two adjacent beads in a bead-spring model or two adjacent nodes in a finite element model. With the discretization length $h = L/40 = 0.25$ applied in this example, it can be computed as

$$\tau_{stretch} = \frac{\gamma_{t\|} h^2}{\pi^2 EA} = 9.1\mathrm{e}-10 \approx 1\mathrm{e}-9. \tag{6.6}$$

In opposition to that, the finite element simulations with implicit Euler scheme were conducted for this example with a time step size $\Delta t = 1\mathrm{e}{-5}$, which is ten thousand times larger. And even this time step size was chosen only for the sake of accuracy of the simulations – for numerical stability already $\Delta t = 1\mathrm{e}{-4}$ was sufficient. Although not only time step size, but also computational cost per time step is larger for an implicit Euler scheme, the first effect dominates over the second one, and the overall reduction of computational cost in practice is tremendous as pointed out in more detail in section 6.2.2. In fact, the computational cost of an explicit Euler scheme for examples like the one considered in this section is often too high to run the simulations with the physically correct parameters. Especially in bead-spring simulations with explicit time integration, often a wrong stretching stiffness is used in order to enable larger time steps assuming that this will affect the simulation results not significantly [54]. Such a modus operandi is possible, of course, only if the properties of the simulated system are known already at least to a certain extent from experiments and theories, which makes fully predictive simulations difficult or even impossible. Therefore in computational polymer physics an implicit Euler scheme as proposed in section 3.2 has great advantages over the explicit Euler scheme most commonly used so far.

---

[9] Reprinted Fig. with permission (and modified axis labels and markers) from [29]. ©2010 by the American Physical Society

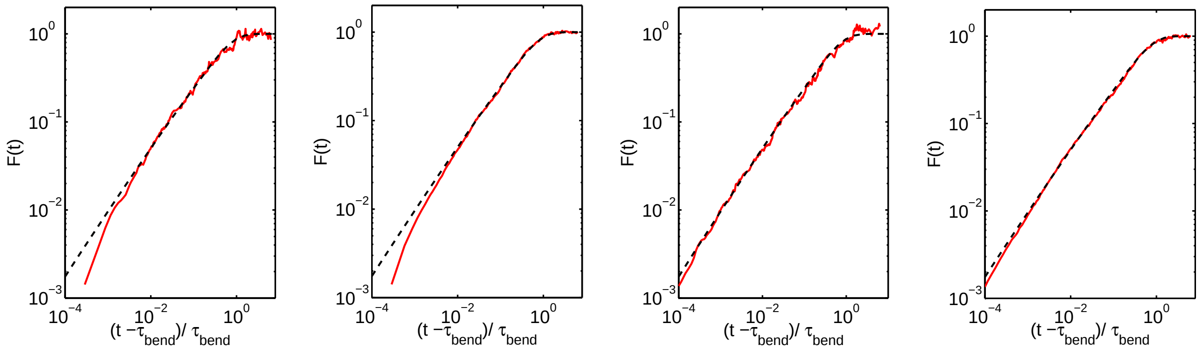

Figure 6.4: Analytical solution of normalized MSD (dashed line) compared to finite element simulation (continued line) with (from left to right): $h = 0.5, \Delta t = 1\text{e}{-2}, n_{sample} = 400$ and $h = 0.5, \Delta t = 1\text{e}{-2}, n_{sample} = 4000$ and $h = 0.25, \Delta t = 1\text{e}{-3}, n_{sample} = 400$ and $h = 0.25, \Delta t = 1\text{e}{-3}, n_{sample} = 4000$[10]

6.1.1.4 Mean-square-difference of end-to-end distance of polymer

The distance $R(t)$ between the end points of a polymer changes continuously over time t due to the stochastic thermal loads the polymer is subject to. One may characterize the dynamics of $R(t)$ by means of a normalized mean-square difference (MSD) of the end-to-end distance, which can be defined for two given points in time t^* and $t \geq t^*$ according to [41] by

$$F(t) = \frac{90L_p^2}{L^4}\langle [R(t) - R(t^*)]^2 \rangle. \tag{6.7}$$

For $t = t^*$, the MSD obviously equals zero and increases in time as the stochastic thermal loads continously deform the polymer and change the end-to-end distance. At later points in time, $[R(t) - R(t^*)]^2$ may either increase or decrease in time. Roughly speaking, it is the more likely to increase the more similar the polymer configuration at t^* is to the one at t and vice versa. Therefore the MSD goes into saturation for large $t^* - t$ when the shapes of the polymers in the observed ensemble sufficiently differ from their inital state at t^*. For polymers in two dimensions with hinged ends, i.e., ends fixed in one coordinate direction, but free in the other one and also free to rotate, a way to compute the MSD analytically was presented in [41] for the stiff limit $L/L_p << 1$. Here L is the length of the polymers and L_p their persistence length. In this section, the MSD observed in finite element simulations is compared to this analytical solution for actin-phalloidin polymers of contour length $L = 10$ at a thermal energy $k_B T = 4\text{e}{-5}$ for $t^* = \tau_{bend}$.

Fig. 6.4 shows how the MSD observed in finite element simulations converges towards the analytical solution if the discretization length h in space and Δt in time are refined and the mean value in (6.7) is approximated by averaging over an ensemble with an increasing number n_{sample} of polymers. For $h = 0.25, \Delta t = 1\text{e}{-3}, n_{sample} = 4000$ excellent agreement between the finite element simulation and the theoretical prediction is observed over more than four orders of magnitude in time.

---

[10] Reprinted Fig. with permission (and modified axis labels) from [28]. ©2009 by the American Physical Society

type	Δt	$D_{t,exp}$	$D_{t,sim}$	$\frac{\lvert D_{t,sim}-D_{t,exp}\rvert}{D_{t,exp}}$	$D_{r\perp,exp}$	$D_{r\perp,sim}$	$\frac{\lvert D_{r\perp,sim}-D_{r\perp,exp}\rvert}{D_{r\perp,exp}}$
DNA 12bp	$5\text{e}{-10}$	$1.34\text{e}2$	$1.41\text{e}2$	4.70%	$2.60\text{e}7$	$2.76\text{e}7$	5.97%
DNA 20bp	$1\text{e}{-9}$	$1.09\text{e}2$	$1.09\text{e}2$	0.37%	$1.03\text{e}7$	$1.02\text{e}7$	0.87%
TMV	$5\text{e}{-6}$	4.50	4.52	0.55%	312	314	0.79%

Table 6.1: Comparison of diffusion coefficients observed in simulations and experiments[11]

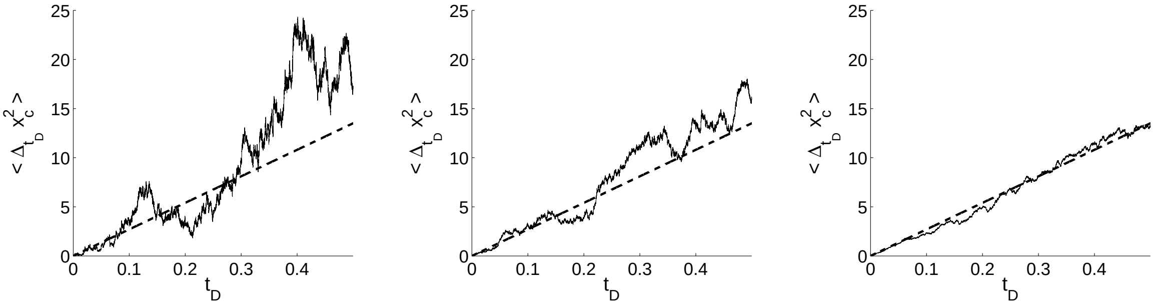

Figure 6.5: Mean square displacement $\Delta_{t_D} x_c^2$ of TMV over time t_D averaged over 1 (left), 5 (middle) and 25 (right) realizations converges towards prediction $6D_{3D,t,exp}t_D$ (dashed line) according to (B.10)[12]

6.1.2 Examples in three dimensions

6.1.2.1 Diffusion of rod-like particles

The diffusion of rod-like particles is highly important in a variety of biological and chemical processes. For example, short DNA or actin filaments, certain viruses as well as several synthetic polymers in the production of fibers can be modeled as rod-like particles, i.e., as rod-like continua short enough to neglect elastic deformation and to concentrate on the rigid-body modes only. In Table 6.1, the translational and orthogonal rotational diffusion coefficients $D_{t,exp}$ and $D_{r\perp,exp}$ measured experimentally in [75] for short DNA (12 and 20 base pairs) and Tobacco Mosaic Virusses (TMV) are compared with their counterparts $D_{t,sim}$ and $D_{r\perp,sim}$ observed in finite element simulations using (B.10) with $t_D = \Delta t$ and averaging over 10^5 successive time steps. In all simulations, the rod-like particles were discretized with one finite element only for the same reasons as in section 6.1.1.1

As can be seen in Table 6.1, the relative error between the simulated diffusion coefficients and the experimentally measured ones is less than 6% even for very short DNA, where complex hydrodynamic interactions close to both ends of the particle become especially important and where hence the classic theories for the friction coefficients of rods are expected to have the greatest difficulties. For longer rod-like particles, the error remains even below 1%. For Table 6.1, the simulated diffusion coefficients were computed averaging motion increments of one particle over a large number of time steps. Fig. 6.5 demonstrates that due to the ergodicity of the diffusion process the same results can be gained when averaging for an arbitrary span on time $t_D > 0$ over an increasing number of independently simulated particles.

---

[11] Reprinted Tab. with permission (and minor changes in notation) from [30]. ©2012 by John Wiley & Sons, Ltd.

[12] Reprinted Fig. with permission (and modified axis labels) from [30]. ©2012 by John Wiley & Sons, Ltd.

	$L_{p,eff}$	$\langle R^2 \rangle$	$\langle R^2_{sim} \rangle$	$\left(\langle R^2 \rangle - \langle R^2_{sim} \rangle\right) / \langle R^2 \rangle$	n_{step}	n_{real}
$J_2 = J_3/4$	6.4793	63.563	58.367	-0.081729	534511	40
$J_2 = J_3$	16.198	82.243	80.808	-0.01744	193828	16
$J_2 = 4J_3$	25.917	88.289	85.678	-0.029581	384350	16

Table 6.2: Effective persistence length $L_{p,eff}$ according to (6.9), analytical mean-square end-to-end distance $\langle R^2 \rangle$ according to (6.8) and simulated mean-square end-to-end distance $\langle R^2_{sim} \rangle$ where simulation results are averaged over n_{step} sample points with a time lag of 0.01 in altogether n_{real} realizations for different ratios of the bending stiffnesses J_2 and J_3[13]

6.1.2.2 Radial distribution function with anisotropic bending stiffness

It is well-known that certain biopolymers such as DNA exhibit an anisotropic bending stiffness, which has interesting consequences for their behaviour in biological systems. As pointed out already in [4], anisotropic bending stiffness cannot be captured by ordinary bead-spring models, but rather requires models with material triads such as finite beam elements. To examine the influence of anisotropic bending stiffness to the statistical mechanics of semiflexible polymers, simulations are conducted for which all parameters are adopted from phalloidin-stabilized actin filaments except for the moment of inertia of area J_2 for which three different values are tested: equal to, four times smaller than, and four times larger than J_3. Theoretical considerations [51] reveal that the mean-square end-to-end distance $\langle R^2 \rangle$ in case of anisotropic bending stiffness is

$$\langle R^2 \rangle = 2L_{p,eff} \left[L - L_{p,eff} \left(1 - e^{-L/L_{p,eff}} \right) \right] \tag{6.8}$$

with the effective persistence length

$$L_{p,eff} = \frac{2J_2 J_3}{(J_2 + J_3) k_B T}. \tag{6.9}$$

Neglecting torsion, the probability distribution itself of the end-to-end distance R can in three dimensions for $J_2 = J_3$ be proven [93] to be

$$\mathcal{G}_{3D}(R) = \frac{1}{\mathcal{N}_3} \sum_{l=1}^{\infty} \frac{1}{\mathcal{M}_{3D}(R)^{3/2}} \exp\left[\frac{(l-0.5)^2}{\mathcal{M}_{3D}(R)} \right] H_2 \left(\frac{l-0.5}{\sqrt{\mathcal{M}_{3D}(R)}} \right), \tag{6.10}$$

where $H_2(.)$ is the second Hermite polynomial, $\mathcal{M}_{3D}(R) = (1 - R/L) L_{p,eff}/L$ and $\mathcal{N}_{3D}$ ensures a normalized distribution. Using the normalized distribution

$$\Gamma_{3D}(R) = \frac{\mathcal{G}_{3D}(R) R}{\int_{R=0}^{R=L} \mathcal{G}_{3D}(R) R dR}, \tag{6.11}$$

one can compare the simulation results with the above described three different combinations of J_2 and J_3 with each other and with the analytical solution from [93] (see Fig. 6.6). For the isotropic case, simulations were conducted both with and without torsion. To switch off torsion, simply the stochastic moments were set to zero, which automatically leads to a zero torsion in a rod with isotropic bending stiffness, straight initial configuration, and no external moments.

---

[13] Reprinted Tab. with permission (and minor changes in notation) from [30]. ©2012 by John Wiley & Sons, Ltd.

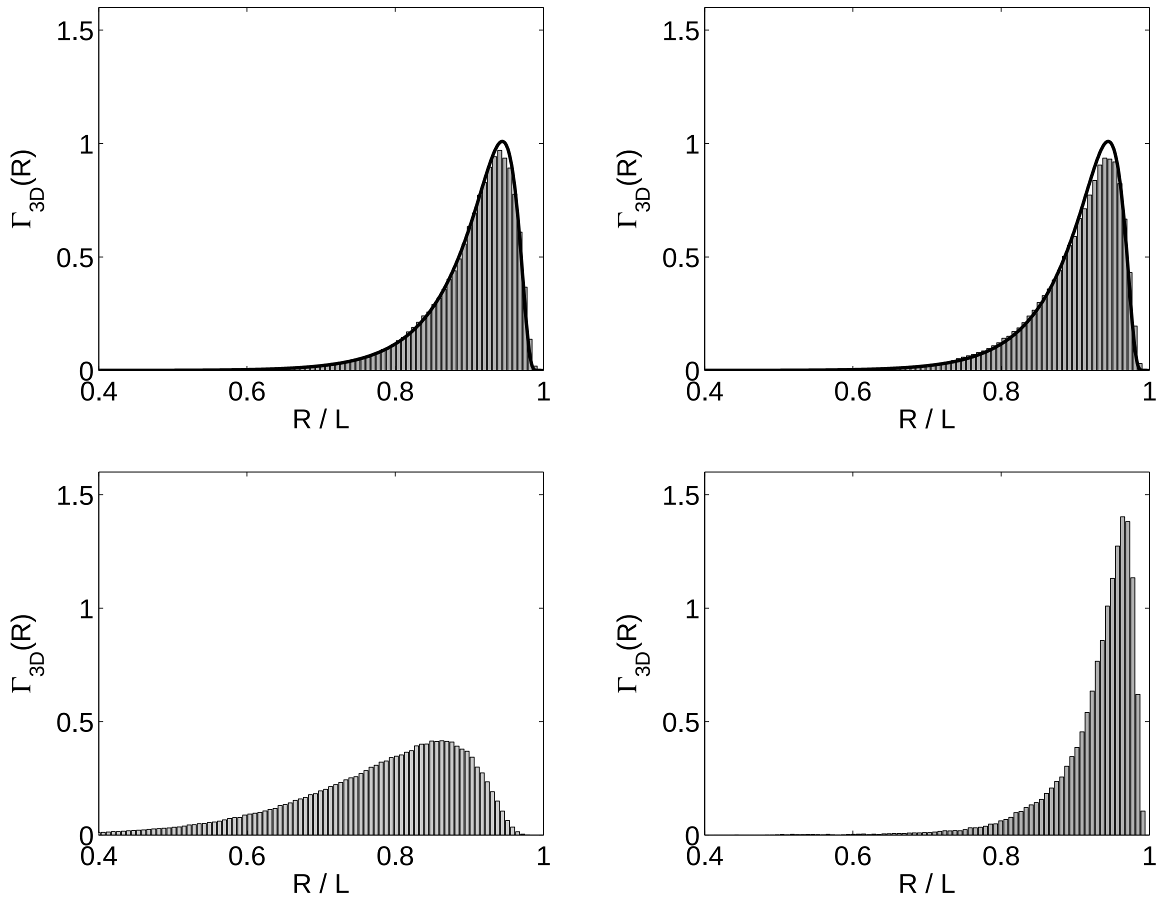

Figure 6.6: Normalized probability density $\Gamma_{3D}(R)$ of the end-to-end distance R computed with finite element simulations (histograms) for $J_2 = J_3$ (top) with (left) and without (right) torsion compared to analytical solution (6.10) (black line) and for $J_2 = J_3/4$ (bottom left) and $J_2 = 4J_3$ (bottom right) with torsion[14]

As expected in the light of the discussion in [51], no perceptible difference is observed for $J_2 = J_3$ between the case with and without torsion. In either case, the simulation results excellently agree with the analytical solution (6.10). Table 6.2 compares the theoretical mean-square end-to-end distances predicted by (6.8) to the mean-square end-to-end distances $\langle R^2_{sim} \rangle$ observed in finite element simulations with torsion. Again, the simulation results excellently agree with the analytical predictions. Clearly, as compared to the isotropic case $J_2 = J_3$, an anisotropic weakening of the bending stiffness by setting $J_2 = J_3/4$ makes much greater a difference than an anisotropic strengthening of the bending stiffness by setting $J_2 = 4J_3$. Again this is in accordance with the discussion in [51] according to which the weaker one of the two principal bending stiffnesses dominates the end-to-end distance similar to a system of two springs in series whose total stiffness is dominated by the softer one of the two springs.

---

[14] Reprinted Fig. with permission (and modified axis labels) from [30]. ©2012 by John Wiley & Sons, Ltd.

6.1.2.3 Tangent correlation function of actin filaments

As discussed in section 6.1.1.3 for the two-dimensional case, also in three dimensions the tangent correlation function can be used for a characterization of the stochastic bending of polymers due to stochastic loads. According to [46], it is given in three dimensions by

$$\vartheta_{3D}(\xi) = \exp\left(-\frac{\xi}{L_p}\right) \tag{6.12}$$

for a polymer with zero torsion deformation. To the author's knowledge, so far no analytic expression in closed form has been derived for the tangent correlation function in three dimensions in the case of a general nonlinear deformation including stochastic torsion. Even for special cases such as a polymer with fixed ends, only recently a tangent correlation function including torsion has been derived [85]. In this example, the effect of stochastic torsion on the tangent correlation function is examined by means of finite element simulations of phalloidin-stabilized actin filaments of length $L = 10$. The filament dynamics is discretized with 40 finite elements and a time step size $\Delta t = 1\text{e}{-5}$.

In Fig. 6.7, the tangent correlation functions observed in finite element simulations with and without stochastic torsion moment are depicted. To switch off torsion, again just the stochastic torsion moment was set to zero as already in section 6.1.2.2. As expected, the result of a computer simulation without stochastic torsion moment accurately fits the function (6.12). Interestingly, the same holds true if a stochastic torsion moment consistent to (3.29b) is incorporated: also then no perceptible difference between the simulated tangent correlation function and the function (6.12) is observed. To understand this, one has to realize that stochastic torsion in polymers happens on much a faster time scale than stochastic bending: bending and torsion stiffness of a rod are typically of the same order of magnitude, whereas the ratio between the respective damping coefficients is according to (3.26) in the order of magnitude of $(L/d)^2$. Thus the effect of torsion to the tangent correlation function is assumed by many theorists to be small due to the high slenderness ratio polymers typically exhibit. This is indeed confirmed by Fig. 6.7.

At the end of this section, it seems worth commenting on an interesting detail: In Fig. 6.7, the coincidence of the tangent correlation function in a finite element simulation with (6.12) both with and without a stochastic torsion moment is demonstrated. However, as torsion always remains zero in an initially straight beam-like continuum with zero Neumann boundary conditions and zero internal loads on the torsional degrees of freedom, the same result is obviously expected also in case that not only the stochastic torsion moment is set to zero, but also the torsion stiffness. Thus modeling a polymer as a rod with zero torsion load and stiffness would already capture essential properties of its Brownian dynamics such as its orientation correlation. This insight may explain why the classic bead-spring model, which is not capable of capturing torsion, has succeeded so much in polymer physics over decades. On the other hand, it immediately leads to the idea of the development of a finite element formulation for a torsion-free rod, which is more efficient than classic bead-spring models and which therefore could be established as a simple and cheap standard alternative to finite beam elements in case that torsion does not matter. For biopolymers like actin for which the existence of a significant torsion stiffness has already been demonstrated experimentally [90, 96], such a computer model would always remain unphysical to a certain extent. However, explicit experimental evidence of a significant torsion stiffness has by far not yet been proposed for all physically and technically interesting

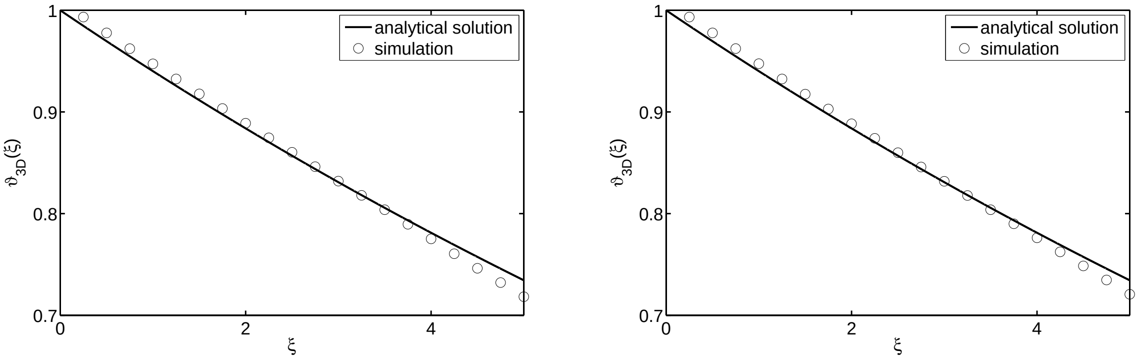

Figure 6.7: Tangent correlation functions in finite element simulations (circles) with (left) and without (right) stochastic torsion compared to the theoretical prediction (continued line) according to (6.12)[15].

micromechanical rod-like structures. Rather one may imagine that effects such as the ionic motion discussed in section 3.1.1 can lead to cases where the torsion stiffness can be neglected compared to the bending stiffness. For these cases, a torsion-free finite element formulation might be not only more efficient, but also physically more correct than common beam elements.

6.2 Biopolymer networks

6.2.1 Viscoelasticity of Actin-rigor-HMM networks with glutaraldehyde

The cytoskeleton in biological cells is a biopolymer network mainly consisting of actin filaments, intermediate filaments and microtubules. In order to explore the physical foundations of the cytoskeleton, often pure actin networks are studied as model systems with different kinds of linkers. The viscoelastic properties of such networks have attracted significant attention in the last years (cf. [63] for recent references). Obviously, the computational analysis of the viscoelasticity of actin networks is an important application for the model developed in this thesis. A comprehensive and general numerical study of the viscoelasticity of actin networks goes by far beyond the scope of this thesis. However, in this section at least the principal capability of the simulation model introduced above to capture this viscoelasticity on a micromechanical scale will be demonstrated. To this end, the storage modulus G^{*} and loss modulus G^{**} of an actin-rigor-HMM(Heavy MeroMyosin) network with glutaraldehyde measured experimentally [65] are compared to the ones observed in computer simulations. The simulation parameters for actin filaments are taken from Table C.1 and C.2 with the following exceptions: the damping coefficients except for $\gamma_{r\|}$ are computed with (3.26) assuming a reduced viscotiy $\eta = 5.5\mathrm{e}{-5}$ instead of $\eta = 1\mathrm{e}{-3}$, which accounts for the effectively reduced drag forces on filaments owing to hydrodynamic interactions in the network. Finally, the parallel rotation damping constant

---

[15] Reprinted Fig. with permission (and modified axis labels) from [30]. ©2012 by John Wiley & Sons, Ltd.

$\gamma_{r\|} = 4.0\text{e}{-5}$ and the cross section $A = 1.9\text{e}{-7}$ are chosen in order to avoid numerical problems as discussed in more detail in the end of this section. Filament length is set to $L = 3$. The linker parameters are set to $E_{cl} = 2.56\text{e}6$, $I_{2,cl} = 4.49\text{e}{-11}$, $I_{3,cl} = 4.49\text{e}{-11}$, $J_{cl} = 8.98\text{e}{-11}$, $A_{cl} = 2.37\text{e}{-5}$, $R_{cl} = 0.1$, $\Delta R_{cl} = 0.02$. These parameters were chosen just heuristically as not much data about the stiffness of rigor-HMM is available from experiments or MD simulations. It is underlined that R_{cl} is chosen 2.5 times larger than indicated in Table 4.1 in order to compensate for the fact that the distance between the filament binding sites in the simulation is $h = 0.125$ and therefore also much larger than in reality. Chemical interactions between filaments and linkers are governed by the parameters $\phi = \pi/4$, $\Delta\phi = \pi/4$, $k_{react,on} = 1\text{e}13$, and $k_{react,off} = 2$. The latter on- and off-rates are used only in the beginning of the simulations until the altogether $n_{cl} = 1400$ linkers in the simulation volume have formed a great number of crosslinks between the filaments. Subsequently, both are set to zero so that no further chemical bonds are formed nor destroyed. This way, the effect of glutaraldehyde is mimicked which prevents chemical bonds between actin and rigor-HMM from breaking up so that in the beginning a great number of chemical bonds is rapidly formed which then remains stable. The overly high on-rate in the beginning is used in order to accelerate the formation of chemical bonds so that the network reaches an equilibrium configuration in a shorter span on time.

The computer simulation is performed with a time step size $\Delta t = 2.5\text{e}{-3}$ in the cubic simulation volume $[0;4] \times [0;4] \times [0;4]$. In x_1- and x_2-direction, periodic boundary conditions are applied. In x_3-direction, a sinosoidal shear deformation $\boldsymbol{u}$ is imposed to the network by a Dirichlet condition with $u_2 = u_3 = 0$ and

$$u_1(\boldsymbol{x}, t) = \begin{cases} 0.08 \sin 2\pi f t & \text{if } x_3 = 5 \\ 0 & \text{if } x_3 = 0, \end{cases} \tag{6.13}$$

where f is the oscillation frequency of the shear deformation. This shear deformation entails in the background fluid the velocity fields

$$\boldsymbol{v} = \frac{\dot{u}_1}{4} \begin{pmatrix} 0 & 0 & 1 \\ 0 & 0 & 0 \\ 0 & 0 & 0 \end{pmatrix} \boldsymbol{x}. \quad \boldsymbol{\omega} = \boldsymbol{0}. \tag{6.14}$$

Fig. 6.8 shows excellent agreement between experiments and computer simulations up to $10Hz$. For frequencies higher than $10Hz$, no experimental data is available. Fig. 6.8 clearly demonstrates the capacity of the micromechanical model developed in this thesis to capture macroscopic material properties of biopolymer networks such as their viscoelasticity. It is underlined that previously published models are not suitable for the low frequency regime examined in this example owing to their tremendous computational cost. For example, the model used in [55] enabled simulations only down to a load frequency of $f = 1Hz$ and even this only at an excessive computational cost (cf. section 6.2.2). In opposition to that, with the simulation model developed in this thesis computational studies are possible down to a load frequency $f = 0.01Hz$. This is especially important, because many biologically relevant processes in biopolymer networks happen on the length scale $1\mu m - 10\mu m$ and time scale $10s - 10^3 s$.

The filament cross section was chosen abnormally small and the filament parallel rotational friction coefficient abnormally large in this example. The reason for this is that too small parallel rotational friction coefficients together with too large axial stiffnesses sometimes lead to

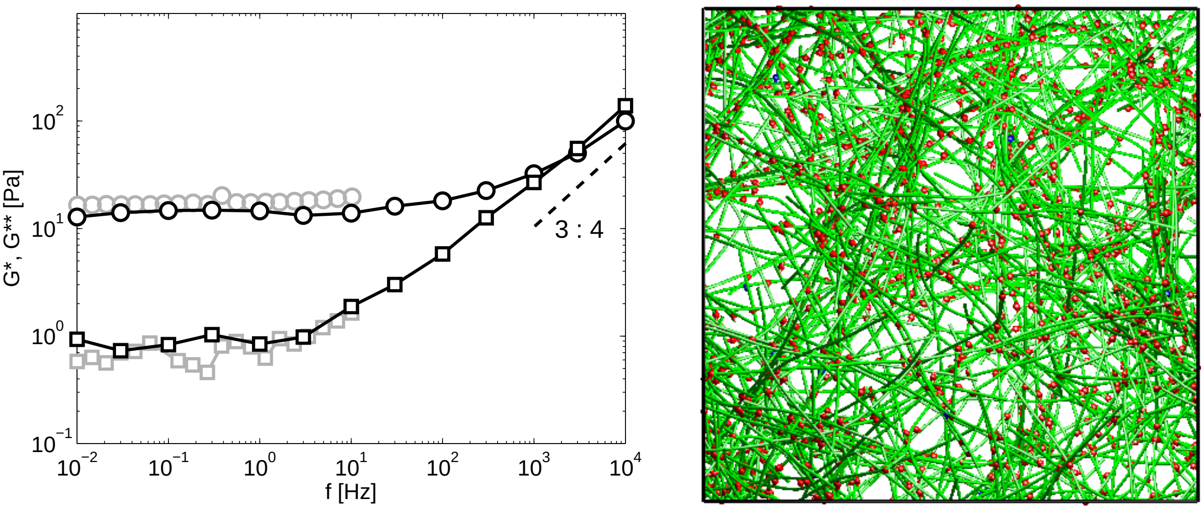

Figure 6.8: Comparison (left) between storage (circles) and loss (squares) modulus observed in simulations (black, [26]) and experiments (grey, [65]); simulated actin-HMM network with glutaraldehyde (right)

numerical problems, especially failure of the Newton-Raphson iterations. The reason for this is possibly that the problem described in section 3.4.3 is alleviated by PTC, but not yet completely solved. The parameter changes applied in this section are not expected to affect the viscoelasticity of the network perceptibly because they do not affect filament bending which is assumed to dominate the network mechanics in the small deformation regime. However, they underline that the development of better beam elements, e.g., of fully non-linear geometrically exact Euler-Bernoulli beam elements, which naturally separate torsion and stretching, or also improvements of the PTC algorithm are rewarding avenues of future research.

6.2.2 Computational performance

Since the 1960s so-called bead-spring models are applied in computational polymer physics for brownian dynamics (BD) simulations, usually together with an explicit Euler time integration scheme. In [54, 55], this approach is employed for micromechanical computer simulations of actin networks. In this section, the efficiency of this approach and the finite element approach developed in this thesis are compared. The simulation of a $12\mu M$ actin network in a cube with edge length 2.8 over the span on time $t_{max} = 1$ is reported in [55] to take approximately 16 days on a single core of an Intel Xeon $2.66GHz$ CPU with a classical bead-spring model. A system with identical physical parameters was simulated with the finite element method developed in this thesis. There, the discretization length h was chosen equal to the one of the bead-spring discretization employed in [55]. The parallel rotational friction coefficient and the Poisson ratio, which do not exist in bead-spring discretizations, were set to $\gamma_{r\|} = 7.3\text{e}{-4}$ and $\nu = 0.3$, and excluded volume effects were considered by means of an augmented Lagrange method with overlap tolerance $5\text{e}{-4}$. On a single core of an Intel Core2 Quad Q6600 2.40GHz CPU, which has – according to public standard benchmarks such as Geekbench – the same performance as the processor employed in [55], the finite element simulation took only 325 minutes and was therefore 71 times – i.e., roughly two orders of magnitude – faster than the bead-spring simulation shown in [55]. The superior performance of the finite element method is even underlined by the fact that in [55] a code tailor-made for bead-spring simulations of biopolymer networks was employed whereas the above finite element simulation was conducted in the multipurpose in-house code BACI of the Institute for Computational Mechanics of the Technische Universität München. Moreover it is emphasized that the above stated difference of two orders of magnitude in efficiency is a conservative estimate yet for another reason: for the comparison the finite element simulations were run with the same discretization length as the bead-spring model in [55]. This neglects, however, that finite elements provide a much higher accuracy at a given discretization length than bead-spring models, which is shown in the right plot of Fig. 6.9. Typically, for a performance comparison between different methods one runs simulations not with the same discretization length, but each method with the discretization length required to achieve a certain given accuracy. If one did so in a comparison between finite elements and bead-spring models, this would even significantly increase the efficiency gain found for finite elements.

To a great extent, the low computational cost of the finite element simulation can definitely be explained by the fact that the implicit Euler scheme allows for a time step size $4.86e5$ times larger than the explicit scheme used in [55]. Therefore an important question is whether a bead-spring model with the same implicit Euler scheme might not be even more efficient due to the simplicity of bead-spring models as compared to finite element models. Fig. 6.9 demonstrates, however, that the computational cost of a discretization with beam-I elements is comparable to the one of a bead-spring discretization. Using an implicit time integration scheme, only beam-II elements have a higher computational cost than bead-spring models, and even there the difference is only a factor of 4. At the same time, Fig. 6.9 reveals that the accuracy of a finite element discretization is by a factor of 4 higher than of a bead-spring discretization. This makes beam-I elements 4 times more accurate than bead-spring models at the same computational cost and with the same discretization length and it compensates half of the higher computational cost of beam-II elements. At the same time, finite elements offer a variety of additional benefits such as material triads allowing for a consistent torsion model and a detailed model of the geometry of chemical binding sites. In addition to that, it is underlined that here only finite elements based on Reissner's beam theory are discussed. However, owing to the high slenderness ratios of many biopolymers, nonlinear Euler-Bernoulli beam elements are actually expected to be even more accurate and efficient – the only reason why such elements are not considered in this thesis is that to the author's knowledge no fully nonlinear geometrically exact Euler-Bernoulli beam element has been developed and published so far. Altogether, these arguments clearly reveal that finite elements are by far more suitable for the spatial discretization of filaments in biopolymer networks and have especially much a greater potential in the future than bead-spring models.

6.2.3 Structural polymorphism of crosslinked actin networks

6.2.3.1 Numerical Study

Crosslinked networks consisting of the same kind of filaments were found in experiments to exhibit vastly different architectures depending on the type and concentration of linkers forming the crosslinks between the filaments. This structural polymorphism has been observed in a great number of experiments, and so far four different kinds of network architectures have been found

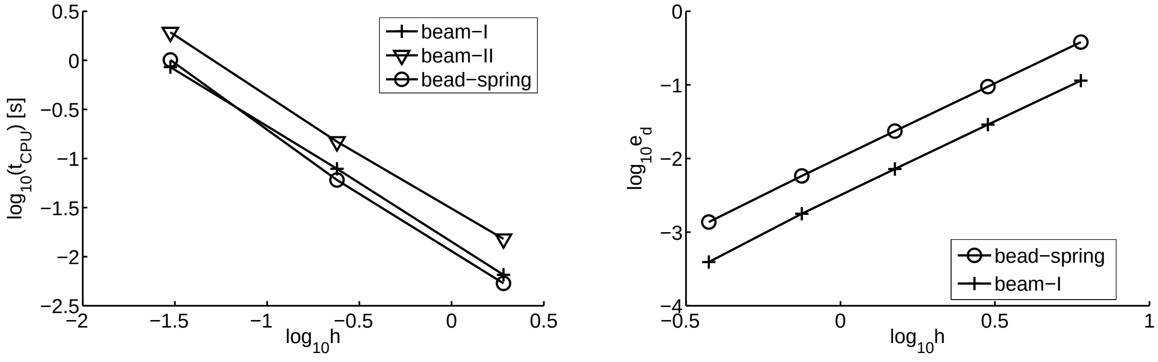

Figure 6.9: CPU time t_{CPU} for simulation of single, free actin filament with time step size $\Delta t =$ 1e-5 and spatial discretization length h over total time $t_{max} = 10$ with beam-I elements, beam-II elements and bead-spring model, respectively (left); convergence of the displacement error e_d at the beam center with finite element and bead-spring discretization for a simply supported beam with central point force, error norm in numerical experiments similar for beam-I and beam-II elements and only for beam-I elements depicted (right)

in actin networks: isotropic-homogeneous networks, bundles, clusters and layers (cf. Figure 2.1). To date, however, only little has been known about which properties of the linkers govern the formation of these different architectures. Theoretical studies such as [9] significantly contributed to the understanding of the underlying physical concepts, but could not explain, e.g., the experimentally observed clusters, nor clarify, which physical properties of linkers, such as stiffness, length and binding behaviour, matter for the structural polymorphism and which do not.

Filaments and linkers are characterized according to sections 3 and 4 by their stiffness, length, and friction coefficients respectively. In networks, also their respective densities play an important role. Chemical reactions between filaments and linkers are according to section 5.1 characterized by the preferred binding angle ϕ, its tolerance $\Delta\phi$, the on-rate $k_{react,on}$, and the off-rate $k_{react,off}$. In the following, the discussion of the structural polymorphism is limited to so-called equilibrium phases, i.e., the structures into which biopolymer networks develop by thermodynamically driven self-organization after a sufficiently long time. In thermal equilibrium, the probability of system states depends only on their free energy. As the free energy is independent on the friction coefficients of a system, friction coefficients cannot affect the structural polymorphism of biopolymer networks in thermal equilibrium. In extensive computational studies with different combinations of the remaining parameters, four principal network architectures were found: homogeneous-isotropic networks, clusters, bundles and layers. These are exactly the same network structures found also in experiments so far (cf. Fig. 6.10).

In order to gain insight especially into the physics of biopolymer networks consisting of actin or actin-like filaments, default parameters for filaments and linkers are chosen as already in section 6.2.1 with the following difference: the default linker cross section is chosen to be $A_{cl} = 4.75\text{e}{-6}$ and the default parameters for chemical linker-filament-bonds are chosen to be $k_{on,react} = 90$, $k_{off,react} = 3$, $\Delta\phi = \pi/16$. Note that this is equivalent to the binding energy $\Delta G_{L+F\rightarrow LF} = 3.4 k_B T$, which guarantees at the temperature T moderate probabilities for both binding and unbinding. With these parameters, first of all a numerical study was conducted

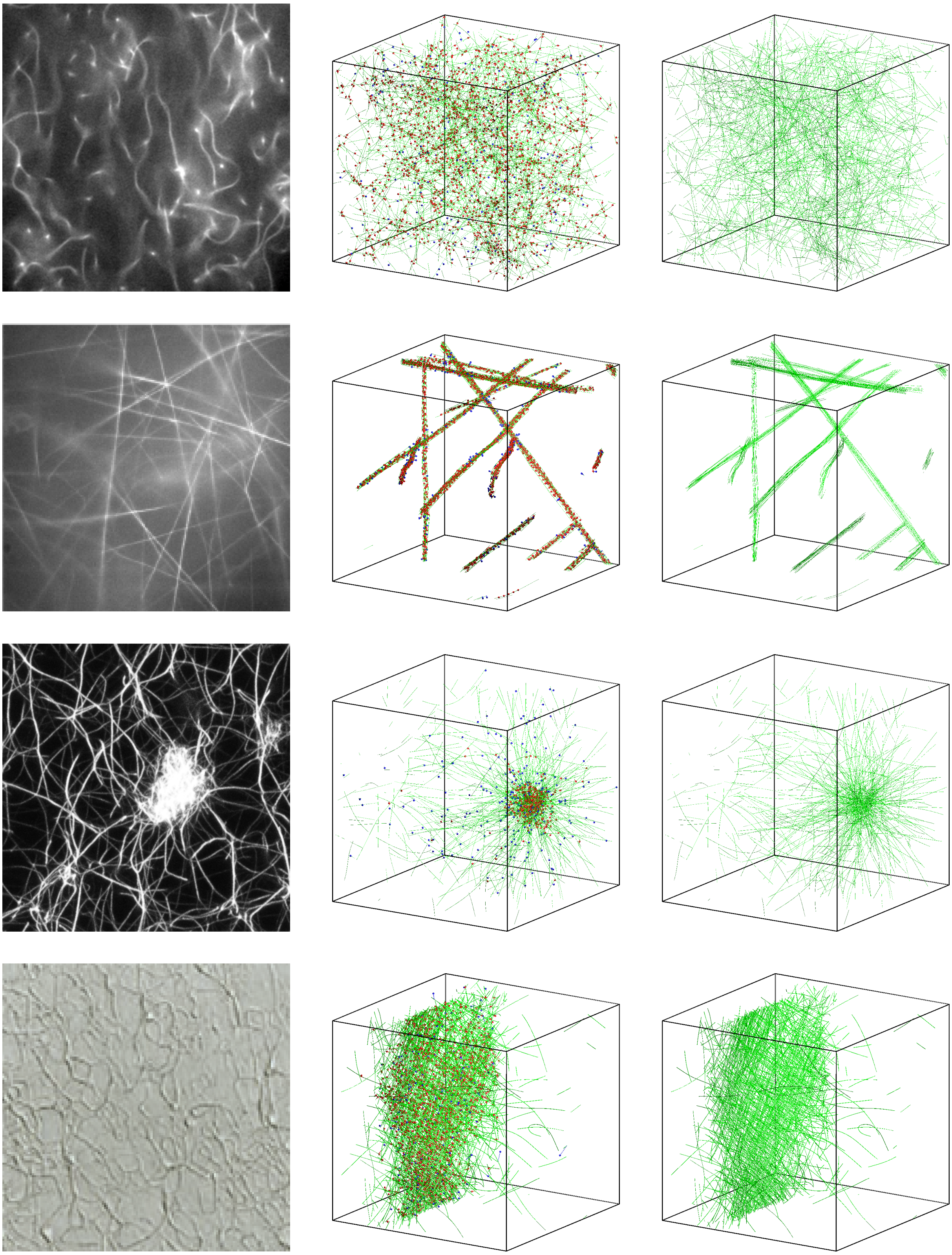

Figure 6.10: Biopolymer networks in vitro (left, [6],[64][1],[6],[94][3]) and in simulations [26] depicted with (middle) and without (right) linkers: homogeneous-isotropic network, bundle network, cluster network, layer network (top down)

for the influence of filament concentration, linker concentration and preferred binding angle ϕ whose results are depicted in Fig. 6.11 and 6.12. Filament concentration can be characterized by the total length ρ_{fil} of all filaments per simulated volume, and linker concentration by the number n_{cl} of linkers in the simulated volume. In the parameter study, the filament concentrations $\rho_{fil} = 3.33$, $\rho_{fil} = 6.66$, $\rho_{fil} = 13.3$ and $\rho_{fil} = 26.6$ were considered, which correspond to actin networks with a molar density of $1\mu M$, $2\mu M$, $4\mu M$ and $8\mu M$, respectively. All simulations were conducted in a cube with simple periodic boundary conditions and edge length 5.

The qualitative main results of this numerical study can be summed up as follows:

(I) At low linker concentrations networks are always homogeneous-isotropic.

(II) For preferred binding angles $\phi \leq \pi/4$ a bundle phase forms for high linker concentrations.

(III) For preferred binding angles $\phi \geq \pi/4$ a layer phase forms for high linker concentrations and a cluster phase may arise at intermediate linker concentrations depending on ϕ and the filament concentration.

(IV) For preferred binding angles around $\pi/3$ and $\pi/2$, the layer phase has a hexagonal and quadratic symmetry, respectively.

(V) All phase transitions happen abruptly, i.e., are supposed to be 1^{st} order transitions except for the transition between bundle and layer phase for variations of ϕ, which seems to happen smoothly via an intermediate state of flat, layer-like bundles and therefore to be a 2^{nd} order phase transition.

In addition to these major qualitative results, some interesting quantitative observations can be made in Fig. 6.11: for small concentrations, the critical linker concentration for aggregation of the homogeneous-isotropic phase into some denser phase - be it a bundle, cluster or layer phase - first strongly decreases with increasing filament concentration, but seems to reach a minimum around $\rho_{fil} = 13.3$ and to subsequently slightly increase again. Thereby the peak of the aggregation concentration moves towards smaller binding angles ϕ and the cluster region grows.

Some of the above results can be understood immediately by means of simple considerations: a higher number of linkers naturally entails a higher number of linkers bound to filaments and therefore also of crosslinked filaments. An increase of the number of linkers is therefore expected to go along with a rearrangement of the filaments into a configuration geometrically allowing an increasing number of crosslinked filaments. Such a configuration is anyway an aggregated state, because only there filaments are close enough to each other to be connected by linkers. In that aggregated state, filaments have to be arranged almost parallel in order to allow for the formation of crosslinks for small ϕ, which leads to a bundle phase. For larger ϕ, however, layers with quadratic or hexagonal symmetry offer for a fixed number of filaments the greatest number of points where these can be crosslinked. Although by such simple considerations a first intuitive understanding for the phase diagram observed in the numerical study can be developed, a detailed theory explaining the other qualitative observations and especially the quantiative ones has not yet been worked out and may be the subject of future work.

In other numerical studies, the effects of linker length, filament length, linker stiffness, and filament persistence length were examined. In none of them, linker stiffness was found to have

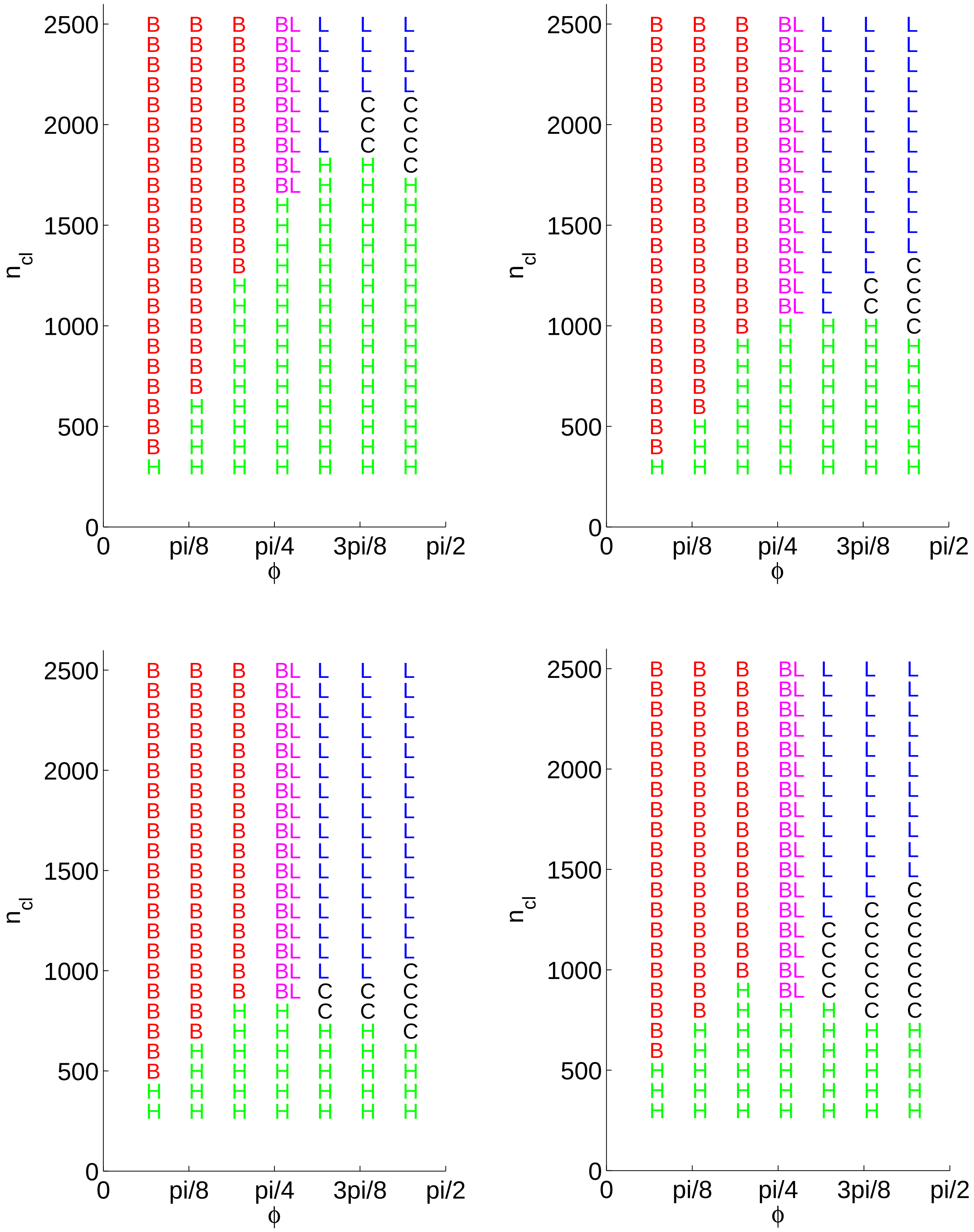

Figure 6.11: Phase diagram for biopolymer networks with filament concentrations $\rho_{fil} = 3.33$, $\rho_{fil} = 6.66$, $\rho_{fil} = 13.3$ and $\rho_{fil} = 26.6$ (from left to right, top down), where B indicates a bundle phase, L a layer phase, BL an intermediate phase of flat and layer-like bundles, C a cluster phase and H a homogeneous-isotropic phase

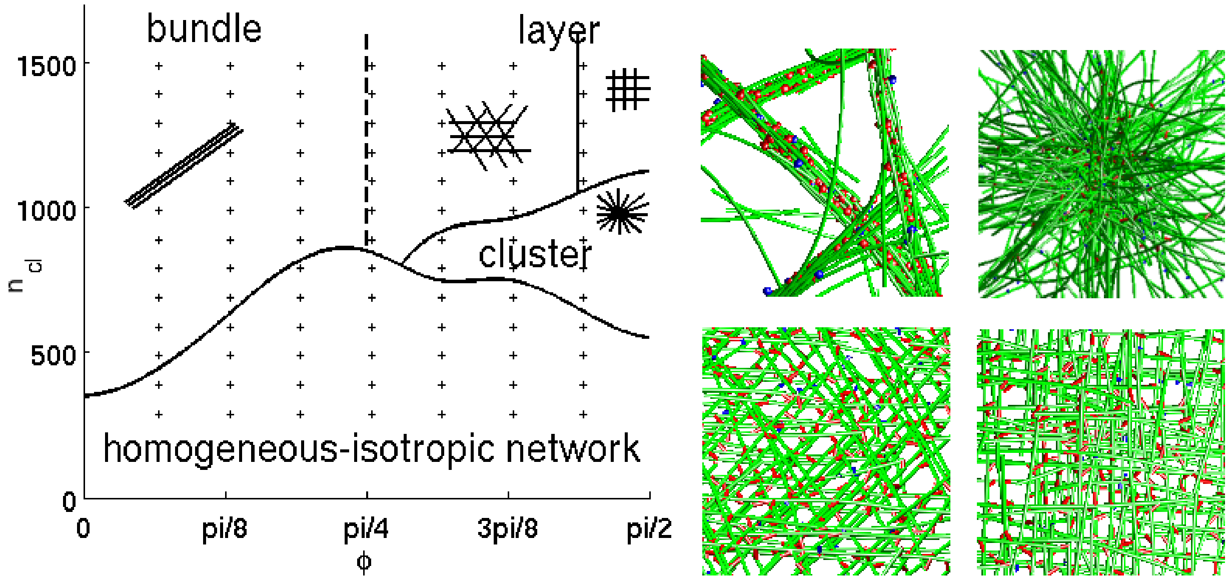

Figure 6.12: Phase diagram for filament concentration $\rho_{fil} = 13.3$ depending on the number of linkers n_{cl} and the preferred binding angle ϕ (left); simulated bundles, cluster, hexagonal layer, quadratic layer (right, from left to right, top down)

any perceptible effect on the network architecture as long as it was varied in a physically reasonable range, i.e., in a range making sure that length changes of linkers remained moderate under the forces linkers were subject to in the network (not more than some percent). Filament length and persistence length affected the borders in the phase diagram quantitatively, but none of the above five qualitative numerical results. A similar effect was observed for linker length, but with an additional special feature: for linker lengths much smaller than the distance h_{bind} between two binding sites on the filaments, the required number of linkers for aggregation of the network grows rapidly. At some point finally, no aggregation takes place at all, because the critical linker concentration for aggregation has risen beyond a point where the great number of linkers makes them decorate all filament binding sites as singly bound linkers so that no crosslinks between different filaments can be formed any longer. Detailed phase diagrams describing the effect of linker length, filament length, linker stiffness, and filament persistence length may be gained easily in the future in a similar way as the diagrams presented in Fig. 6.11.

6.2.3.2 Discussion

In this section, we will briefly discuss the limitations of the results presented in section 6.2.3.1 as well as some promising avenues of future research.

As mentioned already in section 5.2, contact interactions were neglected in the above study. As a consequence its validity is limited to the equilibrium thermodynamics of networks with (infinitesimally) thin filaments. Although the effect of a finite filament and linker volume to the thermodynamic equiblibrium states of polymer networks has not yet been studied numerically, it can be estimated at least roughly by some theoretical considerations: in the isotropic-homogeneous networks considered, the average distances between filaments and linkers are large due to their small volume fraction. If filaments yet come close to each other, already at moderate linker densities the formation of a crosslink is more likely than mechanical contact due to the much higher interaction range R_{cl} of linkers as compared to the filament diameter d. Thus, only at very low linker densities the homogeneous-isotropic phase might be affected significantly by contact interactions. However, this is not expected either because filament volume fraction and diameter in the networks considered are too small for, e.g., the formation of a nematic phase (cf. [9]). As the isotropic-homogeneous phase, also the layer phase is not assumed to be affected perceptibly by contact interactions. Rather contact interactions are expected to just make sure that the spacing between the filaments in the layer is nowhere smaller than the filament diameter which is easily possible without any major change of the layer architecture. In cluster and bundle phases, contact interactions naturally play a larger role owing to the high density of filaments there. Postprocessing of the simulation data in section 6.2.3.1 shows, however, that the mesh size in the cluster centers there is typically still much larger than the diameter of actin filaments so that the statements about the cluster phase in this section are not expected to change much if contact interactions are accounted for in future studies. Anyway, the same postprocessing of simulation data reveals also that in the bundles the spacing between the filaments is often much smaller than the diameter of actin filaments. Thus for bundles, significant changes in the arrangement of the filaments are expected if contact interactions with realistic filament diameters are included in the simulation. Owing to the orientation constraints of the linkers, one may assume, however, that contact interactions play a role in the first place for the question how filaments are arranged in the bundles rather than for the question whether bundles are formed at all.

The numerical study in section 6.2.3.1 is based on the comparatively simple linker model described in sections 2.3, 2.4, 4 and 5.1. Future work may address the issue of structural polymorphism on the basis of much more detailed linker models as discussed briefly in the end of section 5.1. Such more detailed linker models are especially expected to enable studies of the filament arrangement in bundles depending on certain geometric properties, e.g., of the filament binding sites. Furthermore, studies with active linker molecules (motor proteins) may give insight into the mechanisms in the cytoskeleton governing cell migration.

Finally, it seems worth underlining two general points about the study in section 6.2.3.1. First, a study of this kind can help finding out of a given set of linker properties those which matter for the structural polymorphism of crosslinked polymer networks. However, it can never be used in order to prove that only these properties play an important or even the most important role in real polymer networks, because certain linker properties relevant in practice may simply lack in the set of parameters considered. It is underlined therefore that the insights gained in numerical studies of crosslinked networks have to be analyzed and examined carefully in close cooperation with experimentalists and theorists in order to avoid false conclusions. The parameter set used in section 6.2.3.1 is in accordance with hypotheses and assumptions underlying to state-of-the-art publications in biophysics and polymer physics. However, it is worth keeping the above point in mind and trying out also alternative sets of linker parameters in the future . For example, one might consider the requirement that linkers can connect filaments only if the connected filaments exhibit a certain axial strain or curvature. This way, one might account for the fact that certain binding sites may be hidden and not capable of forming chemcial bonds if the filament is not deformed in a certain way.

The second point which should be underlined at the end of this section is the in general limited reliability of statements about equilibrium configurations in networks. In the numerical study in section 6.2.3.1, configurations were assumed to be equilibrium configurations if the network had reached a state where no further significant changes of the network architecture were observed. For certain structures, some additional tests were conducted. For example, it was tested whether the cluster formed independently on the filament configuration at the simulation start by trying out an isotropic-homogeneous and a layer starting configuration. Yet even with such additional tests, it is impossible proving in a strict sense that the observed configurations are equilibrium configurations and not only stagnated intermediate configurations which are trapped in non-equilibrium, e.g., owing to a local minimum of free energy which the networks could not leave within the finite span on time simulated. Although this general flaw of numerical studies of thermodynamic systems should always be kept in mind, it is underlined that experimental and theoretical methods suffer from the same deficiency: usually, it is hard to say whether an experimental system has already reached a global minimum of free energy or just a local one, and determining the global minimum of free energy of complex systems analytically is often not possible either. Hence this second point is rather a general one to be kept in mind when investigating equilibrium states than a point applying only to the numerical study presented in section 6.2.3.1. In the light of this discussion, is is especially worth paying more attention to the cluster phase in the future: whereas simulations suggest that the cluster phase is an equilibrium phase, in experiments clusters have already been observed to dissolve when the temperature was increased, which would rather make assume that clusters are only kinetically trapped non-equilibrium structures. To decide how these two observations fit together, further analysis – if possible also on the basis of theoretical free energy considerations – is definitely required.

7 Conclusions and Outlook

7.1 Conclusions

In this thesis, a new approach for the analysis of biopolymer networks based on a micromechanical continuum model is proposed. To this end, three main constituents of biopolymer networks – filaments, linkers and fluid – are distinguished and modeled as continua, respectively. The mechanics of filaments is assumed to dominate the mechanics of the networks, and thus only coarse models are employed for linkers and fluid.

Linkers are modeled as rod-like continua. However, in practice their deformation is simulated explicitly by means of finite truss or beam elements only if they connect two filament binding sites and affect therefore the network mechanics significantly. Otherwise only the position of their center is kept track of by a simple diffusion equation.

The fluid is modeled as a continuum on the basis of the incompressible linearized Navier-Stokes equations. Detailed fluid-structure interactions are thereby not considered. Rather the fluid velocity field is computed in the absence of filaments and linkers, and the friction which these experience is then computed by certain friction coefficients and their velocity relative to the fluid.

Most attention is payed to the filaments. For them, a completely new numerical method is developed, a finite element method for rod-like continua embedded into a thermal bath. To the author's knowledge this is the first method for the simulation of polymers in a thermal bath, which is derived from first principles of statistical and Newtonian mechanics in a mathematically stringent way. It surpasses, however, state-of-the-art methods not only by its consistent theoretical foundation, but also by its great flexibility and high efficiency. For example the introduced finite element method can deal with torsion in three dimensions without problems (cf. section 3.1.1.1) and allows for distinguishing between different directions perpendicular to the filament axes in a proper manner (cf. section 5.1), whereas the highly popular classical bead-spring models lack this capabilities.

In a variety of examples, excellent agreement between computer simulations based on the approach developed in this thesis, experimental results, and theoretical predictions is shown both for computer simulations of single filaments and complete biopolymer networks. Moreover, the capacity of the approach to address questions to which theorists and experimentalists have not yet found answers is demonstrated by the example of the so-called structural polymorphism of biopolymer networks. By means of parameter studies, the computer model developed in this thesis allows for the first time examining systematically the influence of certain properties of the crosslinker molecules to this polymorphism. Especially, it reveals the conditions under which cluster-shaped thermodynamic equilibrium phases arise in crosslinked biopolymer networks, which has not yet been described before in literature.

The method for the simulation of biopolymer networks developed in this thesis is approximately two orders of magnitude faster than state-of-the-art methods - and it is emphasized that this is still a conservative estimate, because in the performance study presented in section 6.2.2 the improved accuracy of finite beam elements as compared to bead-spring models with the same discretization length has not even been factored in when determining this difference in computational efficiency. Therefore the finite element method developed in this thesis has the potential to completely substitute a series of methods in computational biosciences in the medium term, especially those based on bead-spring models, which may be considered a de-facto standard in computational polymer physics since the 1960s. In view of the computational resources currently available, the method developed in this thesis is practically the first one allowing for simulations of biopolymer networks on the biologically most relevant length scale $1\mu m - 10\mu m$ and time scale $10s - 10^3s$.

Many of the concepts and arguments developed in this thesis are general enough to be easily transferred to or combined with other numerical methods recently published in computational engineering and biosciences. For example, the theory developed in section 3 can be applied straight forward not only together with finite elements, but virtually with any Galerkin method. Thus one might replace in the future finite elements in the spatial discretization by novel methods such as NURBS [18] or maximum-entropy approximation schemes [5, 24, 25, 27] for higher accuracy and lower computational cost. And not only more powerful numerical methods for the spatial discretization can be employed in the future, but also other beam theories. Due to the typically very high slenderness ratio of biopolymers, the application of the Euler-Bernoulli beam theory instead of Reissner's beam theory may decrease the computational cost and at the same time increase the accuracy of the model. In this thesis Reissner's beam theory was actually employed only, because to the author's knowledge no fully-nonlinear geometrically exact Euler-Bernoulli beam element has been published so far. The development of such an element and its application in simulations of biopolymer networks is expected to be a promising avenue of future research.

It is emphasized that the finite element method for Brownian dynamics simulations developed in this thesis can be implemented easily as an add-on in already existing simulation codes. To this end, basically only the evaluation of the discrete stochastic and viscous force and moment vectors has to be programmed, which is expected to be possible within a couple of hours. Therefore this method can be used easily for a variety of projects where biopolymer networks are simulated with finite elements [1, 44, 49, 66, 74].

Moreover, its stringent theoretical foundation is in general expected to facilitate model extensions of any kind. Especially, a more complex fluid model accounting possibly also for fluid-structure interactions or the incorporation of electrostatic potentials may be accomplished in future work. Also atomistic-to-continuum coupling methods may be used in order to enrich the model by more information about atomistic processes.

The high efficiency, reliability, flexibility and extensibility, the computer model developed in this thesis exhibits in several test cases and examples give rise to the hope that it can serve as a valuable tool for biophysicists, bioengineers and biomedical engineers dealing with the mechanics of cells and tissue, for material scientists working on the development of new bio-inspired materials and also for engineers in several other fields. In the following section, a brief outlook is given to a choice of potential future application fields.

7.2 Outlook

In this section, a couple of potential future applications of the computer model developed in this thesis are decribed. By no means, the following sections are intended to be a complete list and comprehensive description of such applications, but rather they may serve as a source of inspiration for future research and help establishing connections to various fields of modern research.

7.2.1 Tissue engineering

Biological tissue consists of cells and the extracellular matrix. The mechanics of cells is crucially governed by their cytoskeleton, which is a biopolymer network mainly consisting of actin, microtubules and intermediate filaments. The extracellular matrix on the other hand is a biopolymer network itself. Hence, the success of tissue engineering techniques depends to a large extent on two different types of biopolymer networks. Obviously, micromechanical computer simulations of such networks may therefore help developing new tissue engineering techniques and designing new devices in this field. Virtual tissue engineering is therefore expected to be a major application field of the computer model developed in this thesis.

7.2.2 Computer-aided design of synthetics

In [67] it was shown that filtering of particles in polymer networks is often not only governed by geometric constraints, such as particle size, but rather by a complex interplay between geometric constraints, electrostatic forces and stochastic thermal forces. As organisms in nature may exploit this principle in order to protect themselves against toxic species or pathogens, so may mankind do. To this end, taylor-made synthetics with optimized filtering properties have to be developed. Using to this end micromechanical computer models of polymer networks together with common optimization algorithms instead of trial-and-error-experiments is expected to allow for significant savings of time and money in this field.

7.2.3 Design of micromechanical devices

The design of micromechanical devices relies in many respects still to a surprisingly large extent on design principles developed originally for macroscopic machines. For example, joints, fixtures, gear boxes or clamps are often constructed in a way which is based on deterministic Newtonian mechanics. On very small length scales where stochastic thermal forces have significant impact, however, smart exploitation of the principles of statistical mechanics may open up simpler and better ways to solve certain problems. A major difficulty for human beings to find such innovative solutions is certainly the fact that in daily life human beings are confronted rather with deterministic than statistical mechanics. The micromechanical computer model for the simulation of Brownian dynamics developed in this thesis is actually general enough to apply also to non-biological rod-like microstructures. Thus this model can serve also for the simulation of artificial micro devices in a stochastic environment. Such simulations may help designers to develop a natural feeling for design principles on this length scale, and together with optimization algorithms they may even help to find automatically optimized solutions to design problems in micro devices exploiting the principles of statistical mechanics in the design of their components.

Another more straight forward way to make use of the simulation method developed in this thesis for the design of micro devices is using it for simulating the Brownian dynamics of polymers in micro-fluidic devices in order to optimize these devices. This approach would be similar to the one presented in [52, 53], but more efficient due to the higher efficiency of the finite element approach developed in this thesis as compared to classical bead-spring models.

7.2.4 Development of bio-inspired design principles in classical engineering

Biological systems often harness environmental conditions in a smart way and rely to a surprising extent on self-organization. In opposition to that, man-made machines are usually rather shielded from their environment and constructed, maintained and finally disposed by interventions of man rather than by self-organisation. Biosciences gain more and more insight into the design principles of natural systems and a major challenge for engineering science is now understanding whether and to which extent these principles could be established as new design principles also in machine design. For example the structural polymorphism of biopolymer networks studied in section 6.2 is governed by the principle of free energy driving self-organization of polymer networks into certain architectures by means of a purely stochastic energy source, the thermal bath. Also in certain man-made machines self-organization of building elements by means of a stochastic energy sources might allow for significant improvements in efficiency and reliability. For example wind power plants are subject to ever changing loads and at the same time stochastic vibrations. A self-organization of the position of special fixtures in such power plants according to a principle similar to the one of the minimum of free energy in statistical mechanics might be exploited to create adaptive structures with optimal bearing strengthes depending on the load they are subject to. This way, the micromechanical computer model of biopolymer networks could after minor modifications be exploited for the development of new design principles in classical engineering. The great importance of biopolymer networks in biological systems makes assume that they where carefully optimized by evolution. This gives rise to the hope that their computer-aided analysis can reveal many more such ideas for new design concepts in engineering which man has never thought of so far.

A Mathematics

A.1 Finite Rotations

In this appendix, a brief introduction into the mathematics of finite rotations and Cosserat continua is given. The target of this appendix is by no means a comprehensive treatment of this subject, for which the reader is referred to articles such as [83, 84] or textbooks such as [22]. Rather just a brief summary of some facts is presented here, which may be helpful for the reader not yet familiar with this field.

Finite rotations can be expressed in $m_t \in \{2; 3\}$ dimensinos by an angle vector $\boldsymbol{\theta} \in \mathbb{R}^{m_r}$ with $m_r = \binom{m_t}{2}$ or equivalently by a rotation matrix $\boldsymbol{R}(\boldsymbol{\theta}) \in \mathbb{R}^{m_t \times m_t}$ whose i-the column is the i-th cartesian coordinate axis $\boldsymbol{e}_i$ rotated by the angle $\boldsymbol{\theta}$. $\boldsymbol{R}(\boldsymbol{\theta})$ can be computed by Rodrigues' formula

$$\boldsymbol{R}(\boldsymbol{\theta}) = \mathbf{1} + \frac{\sin\theta}{\theta}\boldsymbol{S}(\boldsymbol{\theta}) + \frac{1-\cos\theta}{\theta^2}\boldsymbol{S}(\boldsymbol{\theta})\boldsymbol{S}(\boldsymbol{\theta}) = \exp\left(\boldsymbol{S}(\boldsymbol{\theta})\right), \tag{A.1}$$

with the so-called spin matrix $\boldsymbol{S}(\boldsymbol{\theta})$, which is in three dimensions given by

$$\boldsymbol{S}_{3D}(\boldsymbol{\theta}) = \begin{pmatrix} 0 & -\theta_3 & \theta_2 \\ \theta_3 & 0 & -\theta_1 \\ -\theta_2 & \theta_1 & 0 \end{pmatrix} \tag{A.2}$$

and in two dimensions by

$$\boldsymbol{S}_{2D}(\boldsymbol{\theta}) = \begin{pmatrix} 0 & -\boldsymbol{\theta} \\ \boldsymbol{\theta} & 0 \end{pmatrix}. \tag{A.3}$$

Obviously, $\boldsymbol{S}(\boldsymbol{\theta})$ satisfies

$$\boldsymbol{S}(\boldsymbol{\theta})^T = -\boldsymbol{S}(\boldsymbol{\theta}), \tag{A.4}$$

and it can be shown that the variation of $\boldsymbol{R}(\boldsymbol{\theta})$ resulting from a variation $\delta\boldsymbol{\theta}$ is

$$\delta\boldsymbol{R}(\delta\boldsymbol{\theta}) = \boldsymbol{S}(\delta\boldsymbol{\theta})\boldsymbol{R}(\boldsymbol{\theta}). \tag{A.5}$$

In this thesis, the symbols $\boldsymbol{S}$ and $\boldsymbol{R}$ are reserved for spin matrices and rotation matrices exclusively. Mathematically, rotation matrices are elements of the special orthogonal group $SO(m_t)$, which is often exploited in theoretical considerations of rotations. In beam mechanics the i-th principal axis of the beam cross section can be represented by the i-th column vector of $\boldsymbol{R}$. This leads to the idea of a Cosserat continuum, where to each point a position $\boldsymbol{x}$ and an independent rotation are assigned. For calculations, the rotation can then be expressed either by a rotation

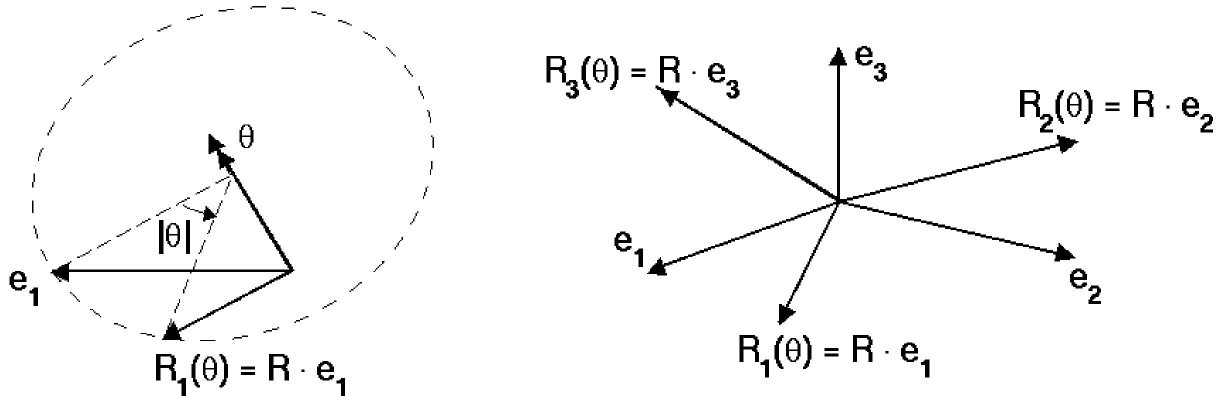

Figure A.1: The unit direction vector and L_2-norm of the rotation vector $\boldsymbol{\theta}$ define the rotation axis and absolute value of the rotation angle, respectively (left); the rotation matrix $\boldsymbol{R}$ can be interpreted as a frame with axes $\boldsymbol{R}_i$ which are the i-th cartesian coordinate axis rotated by $\boldsymbol{R}$, respectively (right)[16].

matrix $\boldsymbol{R}$ or equivalently a rotation vector $\boldsymbol{\theta}$. Usually, in numerical methods for Cosserat continua both representations are used together: the degrees of freedom of the system are defined using rotation vectors as the application of rotation matrices (or alternatively quaternions [22]) would go along with larger equation systems without any additional information. Updates of configurations in three dimensions, however, are performed by means of rotation matrices (or equivalently quaternions) owing to the non-additivity of rotation vectors in three dimensions.

A.1.1 Finite Rotations in three dimensions

In three dimensions, $\boldsymbol{\theta}$ is a three dimensional vector which points parallel to the axis of the rotation and whose absolute value is the angle of the counterclockwise rotation about this axis (see Fig. A.1). Difficulties in handling finite rotations in three dimensions arise from the fact that a compound rotation of two subsequent rotations $\boldsymbol{\theta}$ and $\boldsymbol{\theta}^*$ is not given by their sum. Thus in three dimensions, the rotations $\boldsymbol{\theta}$ and $\boldsymbol{\theta}^*$ can be written as three dimensional vectors, but an addition of these vectors in the common way does not make sense. Because of this non-additivity, $\boldsymbol{\theta}$ and $\boldsymbol{\theta}^*$ are often referred to as 'pseudo-vectors'. For dealing with compound rotations in three dimensions conveniently, one does not consider the rotation pseudo-vectors, but rather the related rotation matrices because the rotation matrix of the compound rotation can be shown to be the matrix-matrix product $\boldsymbol{R}(\boldsymbol{\theta}^*)\boldsymbol{R}(\boldsymbol{\theta})$. The rotation pseudo-vectors remain non-additive even in case of infinitesimal rotation increments to finite rotations so that even for variations one has to distinguish between an additive variation $\delta_a\boldsymbol{\theta}$ and a non-additive one $\delta\boldsymbol{\theta}$. These are related to each other by

$$\boldsymbol{R}(\boldsymbol{\theta} + \delta_a\boldsymbol{\theta}) = \boldsymbol{R}(\delta\boldsymbol{\theta})\boldsymbol{R}(\boldsymbol{\theta}), \tag{A.6}$$

i.e., $\delta_a\boldsymbol{\theta}$ is the quantity to be added to $\boldsymbol{\theta}$ in order to obtain the same compound rotation as by rotating from $\boldsymbol{\theta}$ by the infinitesimal angle $\delta\boldsymbol{\theta}$. Elementary calculus reveals

---

[16] Reprinted Fig. with permission from [30]. ©2012 by John Wiley & Sons, Ltd.

$$\delta_a \boldsymbol{\theta} = \boldsymbol{T}(\boldsymbol{\theta})\delta\boldsymbol{\theta} \tag{A.7}$$

with the so-called inverse exponential map

$$\boldsymbol{T}(\boldsymbol{\theta}) = \frac{\boldsymbol{\theta}\boldsymbol{\theta}^T}{\theta^2} + \frac{\theta/2}{\tan(\theta/2)}\left(\mathbf{1} - \frac{\boldsymbol{\theta}\boldsymbol{\theta}^T}{\theta^2}\right) - \boldsymbol{S}(\boldsymbol{\theta}). \tag{A.8}$$

The symbol $\boldsymbol{T}$ is reserved in this thesis for the inverse exponential map exclusively. At the end of this introduction into finite rotations in three dimensions, it is worth mentioning that in three dimensions the spin matrix satisfies

$$\boldsymbol{S}(\boldsymbol{\theta})\boldsymbol{y} = -\boldsymbol{S}(\boldsymbol{y})\boldsymbol{\theta}, \forall \boldsymbol{y} \in \mathbb{R}^3, \tag{A.9}$$

A.1.2 Finite Rotations in two dimensions

In two dimensions, $\boldsymbol{\theta}$ is a scalar describing the counterclockwise rotation in the considered plane. As it is additive, finite rotations can usually be handled very easily. Especially, formula (A.1) simplifies significantly to

$$\boldsymbol{R}(\boldsymbol{\theta}) = \begin{pmatrix} \cos\boldsymbol{\theta} & -\sin\boldsymbol{\theta} \\ \sin\boldsymbol{\theta} & \cos\boldsymbol{\theta} \end{pmatrix} \tag{A.10}$$

so that the variation of the rotation matrix is simply

$$\delta\boldsymbol{R}(\boldsymbol{\theta}) = \frac{\partial\boldsymbol{R}(\boldsymbol{\theta})}{\partial\boldsymbol{\theta}}\delta\boldsymbol{\theta} = \begin{pmatrix} -\sin\boldsymbol{\theta} & -\cos\boldsymbol{\theta} \\ \cos\boldsymbol{\theta} & -\sin\boldsymbol{\theta} \end{pmatrix}\delta\boldsymbol{\theta}. \tag{A.11}$$

A.2 Wiener process and white noise

The Wiener process is a stochastic process of paramount importance in statistical physics and also many other field of theoretical physics and applied mathematics. In this appendix a brief introduction is given into the definition and properties of this process and its derivative, the so-called white noise. By no means this appendix is intended to present a rigorous mathematical treatment, for which the reader is referred to standard textbooks such as [56, 57]. Rather it just tries to give a brief summary of important definitions and properties, in order to help the reader not yet familiar with Wiener processes in understanding their importance for statistical physics.

A scalar stochastic process $\mathcal{S}$ assigns to each point in time $t \geq 0$ a random variable $\mathcal{S}(t)$. The standard Wiener process $\mathcal{W}$ is an almost surely continuous stochastic process with the following properties:

(I) $\mathcal{W}(0) = 0$,

(II) $\mathcal{W}(t) - \mathcal{W}(t^*) = \mathcal{Z}(0, \sqrt{t - t^*}) \quad \forall t \geq t^* \geq 0$,

(III) $\mathcal{W}(t) - \mathcal{W}(t^*)$ and $\mathcal{W}(s) - \mathcal{W}(s^*)$ are independent for any $0 \leq t < t^* \leq s < s^*$.

Here $\mathcal{Z}(0, \sqrt{t-t^*})$ is a Gaussian random number with zero mean and standard deviation $\sqrt{t-t^*}$. This means that the standard Wiener process starts at zero and develops then between subsequent points in time by pairwise independent Gaussian random increments. Obviously, the Wiener process is symmetric and has the mean value $\langle \mathcal{W}(t) \rangle = 0$. In Fig. A.2 three realizations of a Wiener process are shown. Apparently, they are continous, but from their jagged shape one can see also another important property which can be shown also mathematically: Wiener processes are almost surely nowhere differentiable. However, whereas it is impossible to define their time derivative in an ordinary way, one can yet define it in a generalized sense. This generalized time derivative $\dot{\mathcal{W}}(t)$ is called white noise. Defining the time step size Δt and the increment $\Delta \mathcal{W}$ of the Wiener process in this span on time, one can approximate the white noise by

$$\dot{\mathcal{W}}(t) \approx \frac{\Delta \mathcal{W}}{\Delta t}. \tag{A.12}$$

Considering the case $\Delta t \to 0$, the white noise becomes due to property (II) of the Wiener process a Gaussian random variable with mean value zero. Because of property (III) the value of the white noise at two distinct points in time t and t^* is independent even if both points in time are arbitrarily close to each other (as long as $t \neq t^*$). This can be expressed also as

$$\left\langle \dot{\mathcal{W}}(t) \right\rangle = 0, \tag{A.13a}$$

$$\left\langle \dot{\mathcal{W}}(t) \dot{\mathcal{W}}(t^*) \right\rangle = \delta_{tt^*}. \tag{A.13b}$$

From property (II) we know $\langle |\mathcal{W}(t)| \rangle \sim \Delta t^{1/2}$ so that the approximation in (A.12) has a singularity of order a half as Δt goes to zero. The fact that this singularity is properly captured by the Dirac-function in (A.13) can be seen by integrating (A.13b) for $t = t^*$ in an interval of size Δt. With the approximation (A.12), property (II) and the well-known properties of the Dirac-function, it follows that this integral takes on the value one on either side of (A.13b).

As discussed in section 3.1.4 and appendix B.1.1 of this thesis, (A.13) is satisfied (with a constant prefactor in (A.13b) and in general in higher dimensions) also by the stochastic excitation force in a thermal bath. The Wiener process and its generalized derivative, the white noise, are therefore tailor-made mathematical tools to describe the mechanics of bodies immersed into a thermal bath.

A.3 Stochastic integrals and differential equations

This appendix gives a brief summary of the common conventions for stochastic integrals. To this end, we consider an ordinary stochastic differential equation of the unknown function $\boldsymbol{x} : t \in \mathbb{R} \mapsto \boldsymbol{x}(t) \in \mathbb{R}^m$ in incremental form

$$d\boldsymbol{x} = \boldsymbol{A}(\boldsymbol{x}(t))dt + \boldsymbol{B}(\boldsymbol{x}(t))d\boldsymbol{\mathcal{W}}. \tag{A.14}$$

Here $\boldsymbol{\mathcal{W}}(t) \in \mathbb{R}^{m_\mathcal{W}}$ is a multidimensional Wiener process, $\boldsymbol{A}(\boldsymbol{x}(t)) \in \mathbb{R}^m$ the so-called drift term and $\boldsymbol{B}(\boldsymbol{x}(t)) \in \mathbb{R}^{m \times m_\mathcal{W}}$ a multiplicative noise term. Assuming $\boldsymbol{x}(t = 0) = \boldsymbol{0}$ we may rewrite (A.14) in an integral form as

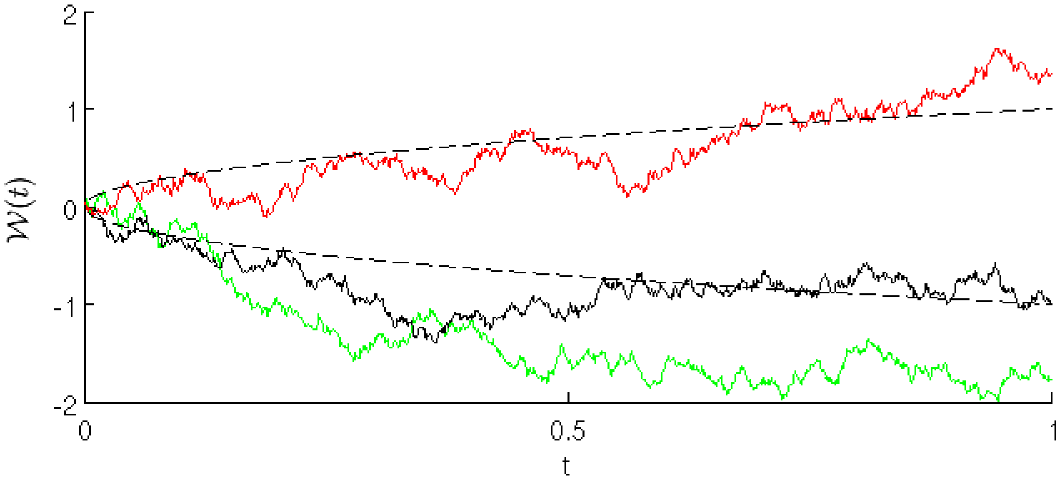

Figure A.2: Different realizations of a standard Wiener process $\mathcal{W}(t)$ together with standard deviation (dashed line)

$$\boldsymbol{x}(t_{max}) = \int_0^{t_{max}} \boldsymbol{A}(\boldsymbol{x}(t))dt + \int_0^{t_{max}} \boldsymbol{B}(\boldsymbol{x}(t))d\boldsymbol{\mathcal{W}}. \tag{A.15}$$

In (A.15), there arise both a deterministic integral with respect to increments dt in time and an integral with respect to increments $d\boldsymbol{\mathcal{W}}$ of the Wiener process. To define the latter integral properly, we divide the time t_{max} uniformly into i_{max} time intervals of length $\Delta t = \frac{t_{max}}{i_{max}}$ and define related increments of the Wiener process $\Delta\boldsymbol{\mathcal{W}}_i = \boldsymbol{\mathcal{W}}((i+1)\Delta t) - \boldsymbol{\mathcal{W}}(i\Delta t)$ with $i \in \{0, 1, 2, \ldots, i_{max}-1\}$. Then integral (A.15) may be defined by

$$\boldsymbol{x}(t_{max}) = \lim_{i_{max}\to\infty} \sum_{i=0}^{i_{max}-1} \boldsymbol{A}\left(\boldsymbol{x}((i+\alpha)\Delta t)\right)\Delta t + \lim_{i_{max}\to\infty} \sum_{i=1}^{i_{max}-1} \boldsymbol{B}(\boldsymbol{x}\left((i+\beta)\Delta t)\right)\Delta\boldsymbol{\mathcal{W}}_i \tag{A.16}$$

with some constant parameters $0 \leq \alpha \leq 1$, $0 \leq \beta \leq 1$. The parameters α and β determine the point in time at which the drift and noise term are evaluated in each time interval, respectively. In deterministic calculus, the value of an integral does not depend on the precise evaluation point in the limit of infinitely small intervals. However, in stochastic calculus one can prove that the value of $\boldsymbol{x}(t_{max})$ in (A.16) does in fact not depend on α, but surprisingly on β [57]. Thus (A.14) and (A.15) define a stochastic differential equation only together with a value β. In principle, any choice is possible. However, there are three specific values of β which are especially common [87] and often written using a special notation of (A.14). Choosing $\beta = 0$ we write

$$d\boldsymbol{x} = \boldsymbol{A}(\boldsymbol{x})dt + \boldsymbol{B}(\boldsymbol{x}) \cdot d\boldsymbol{\mathcal{W}} \tag{A.17}$$

and call (A.17) an Itō or left-point stochastic differential equation and the related stochastic integrals are called forward integrals. With $\beta = 0.5$ we write

$$d\boldsymbol{x} = \boldsymbol{A}(\boldsymbol{x})dt + \boldsymbol{B}(\boldsymbol{x}) \circ d\boldsymbol{\mathcal{W}} \tag{A.18}$$

and call (A.18) a Stratonovich or mid-point stochastic differential equation and the related integral a Stratonovich integral. Finally, with $\beta = 1$ we write

$$d\boldsymbol{x} = \boldsymbol{A}(\boldsymbol{x})dt + \boldsymbol{B}(\boldsymbol{x}) \bullet d\boldsymbol{\mathcal{W}} \tag{A.19}$$

and call (A.19) a right-point stochastic differential equation and the related integral a backward integral. Note that all the three dot operators in (A.17), (A.18), and (A.19) denote a matrix-vector product between the matrix $\boldsymbol{B}(\boldsymbol{x})$ and the vectorial Wiener process increments $d\boldsymbol{\mathcal{W}}$ just with different values of β. The result of a stochastic integral depends on the evaluation point of the noise term, i.e. β. However, the equations with respect to different evaluation points may be transformed into each other. Let us consider two stochastic processes $\boldsymbol{x}^{\beta_1}$ and $\boldsymbol{x}^{\beta_2}$, which are defined by the SDEs

$$d\boldsymbol{x}^{\beta_1} = \boldsymbol{A}^{\beta_1}(\boldsymbol{x})dt + \boldsymbol{B}^{\beta_1}(\boldsymbol{x})d\boldsymbol{\mathcal{W}}, \tag{A.20}$$

$$d\boldsymbol{x}^{\beta_2} = \boldsymbol{A}^{\beta_2}(\boldsymbol{x})dt + \boldsymbol{B}^{\beta_2}(\boldsymbol{x})d\boldsymbol{\mathcal{W}}, \tag{A.21}$$

where $0 \leq \beta_1, \beta_2 \leq 1$ define the evaluation point of the noise term in an integral form of (A.20) and (A.21) similar to (A.16). According to [56], both stochastic processes are equivalent despite the different integral conventions employed if the following equations are true

$$\begin{aligned}
\boldsymbol{A}^{\beta_2}(\boldsymbol{x}) &= \boldsymbol{A}^{\beta_1}(\boldsymbol{x}) + (\beta_1 - \beta_2)\sum_{j,k} B^{\beta_2}_{j,k}(\boldsymbol{x})\frac{\partial \boldsymbol{B}^{\beta_2}_k(\boldsymbol{x})}{\partial x_j}, && \text{(A.22)}\\
\boldsymbol{B}^{\beta_1}(\boldsymbol{x}) &= \boldsymbol{B}^{\beta_2}(\boldsymbol{x}), && \text{(A.23)}\\
\boldsymbol{x}^{\beta_1}(0) &= \boldsymbol{x}^{\beta_2}(0). && \text{(A.24)}
\end{aligned}$$

Here $\boldsymbol{B}^{\beta_2}_k$ denotes the k-th column vector and $B^{\beta_2}_{i,k}$ the ik-element of the matrix $\boldsymbol{B}^{\beta_2}$. This means that each SDE with some integral convention can be written equivalently with another integral convention when changing the drift term. What has to be added when changing the integral convention depends only on the noise term and is therefore often referred to as noise-induced or spurious drift term. Note that the way integrals are defined in (A.16) corresponds to the numerical one-step-θ schemes used to approximate an integral by a finite sum. Thus, stochastic integrals according to (A.16) with $\beta = 0$, $\beta = 1/2$ and $\beta = 1$ can be numerically approximated directly by the explicit Euler scheme, the trapezoidal rule and the implicit Euler scheme, respectively. Sometimes in practice it may be necessary to solve an SDE with a certain value β using a one-step-θ scheme with $\theta \neq \beta$. For example, it may be necessary to solve a Stratonovich SDE with $\beta = 0.5$ with an explicit Euler scheme with $\theta = 0$. In that case, one first has to transform the SDE using (A.22) into an equivalent SDE with $\beta = \theta$. Then one can directly utilize the desired one-step-θ scheme for the numerical solution of the SDE.

A.4 Decomposition of damping matrices

In (3.29), prefactors $\boldsymbol{s}_t$ and $\boldsymbol{s}_r$ for the Wiener processes are required which satisfy $\boldsymbol{s}_t\boldsymbol{s}_t^T = \boldsymbol{c}_t$ and $\boldsymbol{s}_r\boldsymbol{s}_r^T = \boldsymbol{c}_r$, where $\boldsymbol{c}_t$ and $\boldsymbol{c}_r$ are the damping matrices from (3.15). In this thesis, only two different types of damping matrices are discussed in detail.

The first type is used in (3.18) and (3.19) and can be written in general in the form

$$\boldsymbol{c} = \boldsymbol{R}(\boldsymbol{\theta})\boldsymbol{c}_{loc}\boldsymbol{R}(\boldsymbol{\theta})^T, \tag{A.25}$$

whith a positive definite diagonal matrix $\boldsymbol{c}_{loc}$ with constant entries. Defining $\sqrt{\boldsymbol{c}_{loc}}$ as the diagonal matrix whose i-th diagonal entry is the square root of the i-th diagonal entry of $\boldsymbol{c}_{loc}$,

$$\boldsymbol{s} = \boldsymbol{R}(\boldsymbol{\theta})\sqrt{\boldsymbol{c}_{loc}} \tag{A.26}$$

satisfies $\boldsymbol{s}\boldsymbol{s}^T = \boldsymbol{c}$.

The second type of damping matrix applied in this thesis are damping matrices $\boldsymbol{c}_t$ according to (3.21). According to [72],

$$\boldsymbol{s}_t = \boldsymbol{1}\sqrt{\gamma_{t\perp}} + (\sqrt{\gamma_{t\|}} - \sqrt{\gamma_{t\perp}})\boldsymbol{x}' \otimes \boldsymbol{x}' \tag{A.27}$$

satisfies $\boldsymbol{s}_t\boldsymbol{s}_t^T = \boldsymbol{c}_t$. At the end of this appendix, it seems worth emphasizing that the above decompositions of the damping matrices are obviously not unique, but rather only one possibility to perform such a decomposition.

A.5 Variations of discrete stochastic and viscous force and moment vectors

For implicit time integration schemes, variations of the discrete stochastic and viscous force and moment vectors in (3.43), (3.44), (3.50) and (3.52) are required. Here we present formulas for their computation if damping is modeled by means of (3.18), (3.19) and (3.21). It is underlined that the following calculations are all based on property (II) required for finite beam elements in section 3.2.1. The symbols $\boldsymbol{S}$, $\boldsymbol{R}$ and $\boldsymbol{T}$ are used exclusively for spin matrices, rotation matrices and inverse exponential maps, respectively, as introduced in appendix A.1. When used without explicit indication of an argument in this appendix, their argument is always assumed to be the rotation vector $\boldsymbol{\theta}$ describing the orientation of the beam cross section at the considered parameter value ξ and point in time t^i. In order to simplify notation, the upper index i is dropped for all quantities referring to the point in time t^i. Moreover, relative translational and rotational velocities are defined as

$$\dot{\boldsymbol{x}}_{rel} = \dot{\boldsymbol{x}} - \boldsymbol{v} \tag{A.28}$$

$$\dot{\boldsymbol{\theta}}_{rel} = \dot{\boldsymbol{\theta}} - \boldsymbol{\omega}. \tag{A.29}$$

If the translational damping forces are computed on the basis of (3.21), the variation of the discrete stochastic and viscous force vectors are

$$
\begin{aligned}
\delta \boldsymbol{F}_{stoch} &= \sum_{IP} \left[\sqrt{\frac{2k_B T w_{IP}}{\Delta t}} \boldsymbol{W}_t \delta \boldsymbol{s}_t \boldsymbol{\mathcal{Z}}_{IP}(0,1) \right]_{\xi=\xi_{IP}} \\
&= \sum_{IP} \left[\frac{\sqrt{2k_B T w_{IP}}(\sqrt{\gamma_{t\parallel}} - \sqrt{\gamma_{t\perp}})}{\sqrt{\Delta t}} \boldsymbol{W}_t \left[\delta \left(\frac{\partial \boldsymbol{x}}{\partial \xi} \right) \otimes \frac{\partial \boldsymbol{x}}{\partial \xi} + \frac{\partial \boldsymbol{x}}{\partial \xi} \otimes \delta \left(\frac{\partial \boldsymbol{x}}{\partial \xi} \right) \right] \boldsymbol{\mathcal{Z}}_{IP}(0,1) \right]_{\xi=\xi_{IP}} \\
&= \sum_{IP} \left[\frac{\sqrt{2k_B T w_{IP}}(\sqrt{\gamma_{t\parallel}} - \sqrt{\gamma_{t\perp}})}{\sqrt{\Delta t}} \boldsymbol{W}_t \left((\boldsymbol{I}_t' \delta \boldsymbol{X}) \left(\frac{\partial \boldsymbol{x}}{\partial \xi} \right)^T + \frac{\partial \boldsymbol{x}}{\partial \xi} (\boldsymbol{I}_t' \delta \boldsymbol{X})^T \right) \boldsymbol{\mathcal{Z}}_{IP}(0,1) \right]_{\xi=\xi_{IP}} \\
&\approx \sum_{IP} \left[\frac{\sqrt{2k_B T w_{IP}}(\sqrt{\gamma_{t\parallel}} - \sqrt{\gamma_{t\perp}})}{\sqrt{\Delta t}} \boldsymbol{W}_t \left(\frac{\partial \boldsymbol{x}}{\partial \xi}^T \boldsymbol{\mathcal{Z}}_{IP}(0,1) + \frac{\partial \boldsymbol{x}}{\partial \xi} \boldsymbol{\mathcal{Z}}_{IP}^T(0,1) \right) \boldsymbol{I}_t' \right]_{\xi=\xi_{IP}} \delta \boldsymbol{X},
\end{aligned}
\tag{A.30}
$$

$$
\begin{aligned}
\delta \boldsymbol{F}_{visc} &= \int_0^L \boldsymbol{W}_t \left[\delta \boldsymbol{c}_t \dot{\boldsymbol{x}}_{rel} + \boldsymbol{c}_t \delta \dot{\boldsymbol{x}}_{rel} \right] d\xi \\
&= \int_0^L \boldsymbol{W}_t \left[\left(\gamma_{t\parallel} - \gamma_{t\perp} \right) \boldsymbol{I}_t' \delta \boldsymbol{X} \frac{\partial \boldsymbol{x}}{\partial \xi}^T \dot{\boldsymbol{x}}_{rel} + \left(\gamma_{t\parallel} - \gamma_{t\perp} \right) \frac{\partial \boldsymbol{x}}{\partial \xi} \otimes \dot{\boldsymbol{x}}_{rel} \boldsymbol{I}_t' \delta \boldsymbol{X} + \boldsymbol{c}_t \left(\frac{1}{\Delta t} - \frac{\partial \boldsymbol{v}}{\partial \boldsymbol{x}} \right) \boldsymbol{I}_t \delta \boldsymbol{X} \right] d\xi \\
&= \int_0^L \boldsymbol{W}_t \left[\left(\left(\gamma_{t\parallel} - \gamma_{t\perp} \right) \frac{\partial \boldsymbol{x}}{\partial \xi}^T \dot{\boldsymbol{x}}_{rel} + \left(\gamma_{t\parallel} - \gamma_{t\perp} \right) \frac{\partial \boldsymbol{x}}{\partial \xi} \otimes \dot{\boldsymbol{x}}_{rel} \right) \boldsymbol{I}_t' + \boldsymbol{c}_t \left(\frac{1}{\Delta t} - \frac{\partial \boldsymbol{v}}{\partial \boldsymbol{x}} \right) \boldsymbol{I}_t \right] d\xi \delta \boldsymbol{X}.
\end{aligned}
\tag{A.31}
$$

If instead (3.18a) or (3.19a) are used to compute the discrete viscous and stochastic force vectors, one has to distinguish between the two and three dimensional case owing to the great differences in the mathematical treatment of rotations there. In three dimensions, the variation of the discrete stochastic and viscous force vectors are

$$
\begin{aligned}
\delta \boldsymbol{F}_{stoch} &\approx \sum_{IP} \sqrt{\frac{2k_B T w_{IP}}{\Delta t}} \boldsymbol{W}_t \delta \boldsymbol{s}_t \boldsymbol{\mathcal{Z}}_{IP}(0,1) = \sum_{IP} \sqrt{\frac{2k_B T w_{IP}}{\Delta t}} \boldsymbol{W}_t \delta \boldsymbol{R} \sqrt{\boldsymbol{c}_{t,loc}} \boldsymbol{\mathcal{Z}}_{IP}(0,1) \\
&= -\sum_{IP} \sqrt{\frac{2k_B T w_{IP}}{\Delta t}} \boldsymbol{W}_t \boldsymbol{S}(\boldsymbol{R} \sqrt{\boldsymbol{c}_{t,loc}} \boldsymbol{\mathcal{Z}}_{IP}(0,1)) \boldsymbol{I}_r \delta \boldsymbol{\Theta}.
\end{aligned}
\tag{A.32}
$$

$$
\begin{aligned}
\delta \boldsymbol{F}_{visc} &= \int_0^L \boldsymbol{W}_t \left[\delta \boldsymbol{c}_t \dot{\boldsymbol{x}}_{rel} + \boldsymbol{c}_t \delta \dot{\boldsymbol{x}}_{rel} \right] d\xi \\
&= \int_0^L \boldsymbol{W}_t \left[\delta \boldsymbol{R} \boldsymbol{c}_{t,loc} \boldsymbol{R}^T \dot{\boldsymbol{x}}_{rel} + \boldsymbol{R} \boldsymbol{c}_{t,loc} \delta \boldsymbol{R}^T \dot{\boldsymbol{x}}_{rel} + \boldsymbol{c}_t \left(\frac{1}{\Delta t} - \frac{\partial \boldsymbol{v}}{\partial \boldsymbol{x}} \right) \boldsymbol{I}_t \delta \boldsymbol{X} \right] d\xi \\
&= \int_0^L \boldsymbol{W}_t \left[-\boldsymbol{S} \left(\boldsymbol{c}_t \dot{\boldsymbol{x}}_{rel} \right) + \boldsymbol{c}_t \boldsymbol{S} \left(\dot{\boldsymbol{x}}_{rel} \right) \right] \boldsymbol{I}_r d\xi \delta \boldsymbol{\Theta} + \int_0^L \boldsymbol{W}_t \boldsymbol{c}_t \left(\frac{1}{\Delta t} - \frac{\partial \boldsymbol{v}}{\partial \boldsymbol{x}} \right) \boldsymbol{I}_t d\xi \delta \boldsymbol{X}.
\end{aligned}
\tag{A.33}
$$

In two dimensions these variations are given by

$$
\begin{aligned}
\delta \boldsymbol{F}_{stoch} &\approx \sum_{IP} \sqrt{\frac{2k_B T w_{IP}}{\Delta t}} \boldsymbol{W}_t \delta \boldsymbol{s}_t \boldsymbol{\mathcal{Z}}_{IP}(0,1) = \sum_{IP} \sqrt{\frac{2k_B T w_{IP}}{\Delta t}} \boldsymbol{W}_t \delta \boldsymbol{R} \sqrt{\boldsymbol{c}_{t,loc}} \boldsymbol{\mathcal{Z}}_{IP}(0,1) \\
&= \sum_{IP} \sqrt{\frac{2k_B T w_{IP}}{\Delta t}} \boldsymbol{W}_t \frac{\partial \boldsymbol{R}}{\partial \boldsymbol{\theta}} \sqrt{\boldsymbol{c}_{t,loc}} \boldsymbol{\mathcal{Z}}_{IP}(0,1) \boldsymbol{I}_r \delta \Theta. \qquad \text{(A.34)}
\end{aligned}
$$

$$
\begin{aligned}
\delta \boldsymbol{F}_{visc} &= \int_0^L \boldsymbol{W}_t \left[\delta \boldsymbol{c}_t \dot{\boldsymbol{x}}_{rel} + \boldsymbol{c}_t \delta \dot{\boldsymbol{x}}_{rel} \right] d\xi \\
&= \int_0^L \boldsymbol{W}_t \left[\delta \boldsymbol{R} \boldsymbol{c}_{t,loc} \boldsymbol{R}^T \dot{\boldsymbol{x}}_{rel} + \boldsymbol{R} \boldsymbol{c}_{t,loc} \delta \boldsymbol{R}^T \dot{\boldsymbol{x}}_{rel} + \boldsymbol{c}_t \left(\frac{1}{\Delta t} - \frac{\partial \boldsymbol{v}}{\partial \boldsymbol{x}} \right) \boldsymbol{I}_t \delta \boldsymbol{X} \right] d\xi \\
&= \int_0^L \boldsymbol{W}_t \left[\frac{\partial \boldsymbol{R}}{\partial \boldsymbol{\theta}} \boldsymbol{c}_{t,loc} \boldsymbol{R}^T \dot{\boldsymbol{x}}_{rel} + \boldsymbol{R} \boldsymbol{c}_{t,loc} \frac{\partial \boldsymbol{R}^T}{\partial \boldsymbol{\theta}} \dot{\boldsymbol{x}}_{rel} \right] \boldsymbol{I}_r d\xi \delta \Theta + \qquad \text{(A.35)} \\
&+ \int_0^L \boldsymbol{W}_t \boldsymbol{c}_t \left(\frac{1}{\Delta t} - \frac{\partial \boldsymbol{v}}{\partial \boldsymbol{x}} \right) \boldsymbol{I}_t d\xi \delta \boldsymbol{X}. \qquad \text{(A.36)}
\end{aligned}
$$

For the computation of the variation of the discrete viscous and stochastic moment vectors in three dimensions, some preliminary considerations are helpful. We first recall that $\boldsymbol{\theta}^{i-1}$ is the rotation vector at the end of the preceeding time step, $\boldsymbol{\theta}$ the currently considered rotation vector, and $\Delta\boldsymbol{\theta}$ the increment between both with $\boldsymbol{R}(\boldsymbol{\theta}) = \boldsymbol{R}(\Delta\boldsymbol{\theta})\boldsymbol{R}(\boldsymbol{\theta}^{i-1})$. The variation $\delta\boldsymbol{\Delta\theta}$ leads to some modified increment $\boldsymbol{\Delta\theta}_{mod}$ satisfying by definition $\boldsymbol{R}(\boldsymbol{\Delta\theta}_{mod}) = \boldsymbol{R}(\delta\boldsymbol{\Delta\theta})\boldsymbol{R}(\boldsymbol{\Delta\theta})$. The variation $\delta\boldsymbol{\theta}$ on the other hand leads to some modified current rotation vector $\boldsymbol{\theta}_{mod}$ satisfying by definition $\boldsymbol{R}(\boldsymbol{\theta}_{mod}) = \boldsymbol{R}(\delta\boldsymbol{\theta})\boldsymbol{R}(\boldsymbol{\theta})$ and at the same time $\boldsymbol{R}(\boldsymbol{\theta}_{mod}) = \boldsymbol{R}(\Delta\boldsymbol{\theta}_{mod})\boldsymbol{R}(\boldsymbol{\theta}^{i-1})$. From the latter four equations, one can conclude $\boldsymbol{R}(\delta\boldsymbol{\Delta\theta}) = \boldsymbol{R}(\delta\boldsymbol{\theta})$ and thus with $|\delta\boldsymbol{\theta}| << \pi$ also $\delta\boldsymbol{\Delta\theta} = \delta\boldsymbol{\theta}$. Using this relation as well as the equations (A.4) to (A.5), the variation of the discrete viscous and stochastic moment vectors follows in three dimensions as

$$
\begin{aligned}
\delta \boldsymbol{M}_{visc} &= \int_0^L \boldsymbol{W}_r \left[\delta \boldsymbol{c}_r \dot{\boldsymbol{\theta}}_{rel} + \boldsymbol{c}_r \delta_a \left(\frac{\Delta \boldsymbol{\theta}}{\Delta t} \right) - \boldsymbol{c}_r \delta \boldsymbol{\omega} \right] d\xi \\
&= \int_0^L \boldsymbol{W}_r \left[\delta \boldsymbol{R} \boldsymbol{c}_{r,loc} \boldsymbol{R}^T \dot{\boldsymbol{\theta}}_{rel} + \boldsymbol{R} \boldsymbol{c}_{r,loc} \delta \boldsymbol{R}^T \dot{\boldsymbol{\theta}}_{rel} + \frac{\boldsymbol{c}_r}{\Delta t} \boldsymbol{T}(\Delta \boldsymbol{\theta}) \delta \boldsymbol{\Delta\theta} - \boldsymbol{c}_r \frac{\partial \boldsymbol{\omega}}{\partial \boldsymbol{x}} \delta \boldsymbol{x} \right] d\xi \\
&= \int_0^L \boldsymbol{W}_r \left[-\boldsymbol{S}\left(\boldsymbol{c}_r \dot{\boldsymbol{\theta}}_{rel} \right) + \boldsymbol{c}_r \boldsymbol{S}(\dot{\boldsymbol{\theta}}_{rel}) + \boldsymbol{c}_r \frac{1}{\Delta t} \boldsymbol{T}(\Delta \boldsymbol{\theta}) \right] \delta \boldsymbol{\theta} d\xi - \int_0^L \boldsymbol{W}_r \boldsymbol{c}_r \frac{\partial \boldsymbol{\omega}}{\partial \boldsymbol{x}} \delta \boldsymbol{x} d\xi \\
&= \int_0^L \boldsymbol{W}_r \left[-\boldsymbol{S}\left(\boldsymbol{c}_r \dot{\boldsymbol{\theta}}_{rel} \right) + \boldsymbol{c}_r \boldsymbol{S}(\dot{\boldsymbol{\theta}}_{rel}) + \boldsymbol{c}_r \frac{1}{\Delta t} \boldsymbol{T}(\Delta \boldsymbol{\theta}) \right] \boldsymbol{I}_r d\xi \delta \Theta - \int_0^L \boldsymbol{W}_r \boldsymbol{c}_r \frac{\partial \boldsymbol{\omega}}{\partial \boldsymbol{x}} \boldsymbol{I}_t d\xi \delta \boldsymbol{X},
\end{aligned}
\tag{A.37}
$$

$$\begin{aligned}\delta\boldsymbol{M}_{stoch} &\approx \sum_{IP}\sqrt{\frac{2k_BTw_{IP}}{\Delta t}}\boldsymbol{W}_r\delta\boldsymbol{s}_r\boldsymbol{\mathcal{Z}}_{IP}(0,1) = \sum_{IP}\sqrt{\frac{2k_BTw_{IP}}{\Delta t}}\boldsymbol{W}_r\delta\boldsymbol{R}\sqrt{\boldsymbol{c}_{r,loc}}\boldsymbol{\mathcal{Z}}_{IP}(0,1)\\ &= -\sum_{IP}\sqrt{\frac{2k_BTw_{IP}}{\Delta t}}\boldsymbol{W}_r\boldsymbol{S}(\boldsymbol{R}\sqrt{\boldsymbol{c}_{r,loc}}\boldsymbol{\mathcal{Z}}_{IP}(0,1))\boldsymbol{I}_r\delta\boldsymbol{\Theta}. \end{aligned} \tag{A.38}$$

In two dimensions, the variations of the discrete stochastic and viscous moments vectors are given by

$$\begin{aligned}\delta\boldsymbol{M}_{visc} &= \int_0^L \boldsymbol{W}_r\left[\delta\boldsymbol{c}_r\dot{\boldsymbol{\theta}}_{rel} + \boldsymbol{c}_r\delta_a\left(\frac{\Delta\boldsymbol{\theta}}{\Delta t}\right) - \boldsymbol{c}_r\delta\boldsymbol{\omega}\right]d\xi\\ &= \int_0^L \boldsymbol{W}_r\left[\frac{\partial\boldsymbol{R}}{\partial\boldsymbol{\theta}}\boldsymbol{c}_{r,loc}\boldsymbol{R}^T\dot{\boldsymbol{\theta}}_{rel} + \boldsymbol{R}\boldsymbol{c}_{r,loc}\frac{\partial\boldsymbol{R}^T}{\partial\boldsymbol{\theta}}\dot{\boldsymbol{\theta}}_{rel} + \frac{\boldsymbol{c}_r}{\Delta t}\right]\boldsymbol{I}_r d\xi\delta\boldsymbol{\Theta} - \int_0^L \boldsymbol{W}_r\boldsymbol{c}_r\frac{\partial\boldsymbol{\omega}}{\partial\boldsymbol{x}}\boldsymbol{I}_t d\xi\delta\boldsymbol{X}, \end{aligned} \tag{A.39}$$

$$\begin{aligned}\delta\boldsymbol{M}_{stoch} &\approx \sum_{IP}\sqrt{\frac{2k_BTw_{IP}}{\Delta t}}\boldsymbol{W}_r\delta\boldsymbol{s}_{rot}\boldsymbol{\mathcal{Z}}_{IP}(0,1) = \sum_{IP}\sqrt{\frac{2k_BTw_{IP}}{\Delta t}}\boldsymbol{W}_r\delta\boldsymbol{R}\sqrt{\boldsymbol{c}_{r,loc}}\boldsymbol{\mathcal{Z}}_{IP}(0,1)\\ &= \sum_{IP}\sqrt{\frac{2k_BTw_{IP}}{\Delta t}}\boldsymbol{W}_r\frac{\partial\boldsymbol{R}}{\partial\boldsymbol{\theta}}\sqrt{\boldsymbol{c}_{r,loc}}\boldsymbol{\mathcal{Z}}_{IP}(0,1)\boldsymbol{I}_r\delta\boldsymbol{\Theta}. \end{aligned} \tag{A.40}$$

B Mechanics of polymers and rod-like particles

B.1 Diffusion

B.1.1 Fluctuation-dissipation theorem

One of the most important theorems in statistical physics is the fluctuation-dissipation theorem. In the form relevant for Brownian dynamics simulations, it states a direct relation between stochastic excitation and damping in a thermal bath. The intention of this appendix is by no means a comprehensive or rigorous treatment of this theorem – for which the reader is referred to standard textbooks such as [88, 89] – but rather a short introduction for the reader not yet familiar with it. To this end, we derive the relation between stochastic excitation and damping for the simple case of a point-shaped particle with one degree of freedom y, negligible mass, and a damping coefficient ζ subject to a stochastic excitation f_{stoch}. The particle is assumed to be tethered to the origin $y = 0$ by a spring with stiffness k. For the reasons mentioned in section 3.1.4 we can assume that the stochastic force is a Gaussian random variable with zero mean value and correlation time, i.e.,

$$\langle f_{stoch} \rangle = 0, \tag{B.1a}$$

$$\langle f_{stoch}(t) f_{stoch}(t^*) \rangle = \nu \delta_{tt^*}, \tag{B.1b}$$

where ν is some unknown scalar constant characterizing the mean amplitude of the stochastic force, and $\langle . \rangle$ denotes a time average. From stochastic analysis it is well-known (cf. appendix A.2) that the above stated properties are equivalent to the ones of a white noise $\sqrt{\nu}\dot{\mathcal{W}}$, which is the generalized time derivative of the Wiener process $\sqrt{\nu}\mathcal{W}$. Therefore we can rewrite (B.1) as

$$f_{stoch}(t) = \sqrt{\nu}\dot{\mathcal{W}}. \tag{B.2}$$

The particle's equation of motion is then

$$ky + \zeta \dot{y} = \sqrt{\nu}\dot{\mathcal{W}}. \tag{B.3}$$

From thermodynamics it is known that each degree of freedom immersed into a thermal bath has the mean energy $k_B T/2$ where k_B is the Boltzmann constant and T the temperature of the bath. Because of the negligible mass of the particle, its energy is $ky^2/2$ which leads to the following two requirements:

(I) $\langle y^2 \rangle = k_B T/k$,

(II) $\langle d(y^2)/dt\rangle = 0$,

where the latter requirement means that on average the particle's energy is neither increasing nor decreasing. The stochastic excitation is feeding energy into a system immersed into a thermal bath and the viscous damping sucking energy out of it. This energy influx and outflux may be different at single points in time, but they have to be equal on time average so that the particle's average energy remains on the long term $k_BT/2$. The assumption of this equilibrium between energy gain by fluctuations and loss by dissipation is one of the central ideas behind the fluctuation-dissipation theorem and origin of its name. To see the relation between stochastic force and drag coefficient following from this assumption, we discretize the equation of motion (B.3) by time steps Δt between the points in time t^i and t^{i+1}. Denoting by an upper index i that a quantity is evaluated at $t^i = i\Delta t$ and defining the Wiener increment $\Delta\mathcal{W}^i = \mathcal{W}^{i+1} - \mathcal{W}^i$, we can rewrite (B.3) in a time discrete manner as

$$y^{i+1} = y^i\left(1 - \frac{\Delta tk}{\zeta}\right) + \frac{\sqrt{\nu}}{\zeta}\Delta\mathcal{W}^i. \tag{B.4}$$

Requirement (II) can then be rewritten by means of a discretization in time as

$$\begin{aligned}
0 = \langle d(y^2)/dt\rangle &= \lim_{\Delta t\to 0}\left\langle \frac{\left(y^{i+1}\right)^2 - \left(y^i\right)^2}{\Delta t}\right\rangle \\
&= \lim_{\Delta t\to 0}\left\langle \frac{\left(y^i\right)^2\left(\frac{\Delta^2 tk^2}{\zeta^2} - \frac{2\Delta tk}{\zeta}\right) + \frac{\nu}{\zeta^2}\Delta^2\mathcal{W}^i + \frac{\sqrt{\nu}}{\zeta}\Delta\mathcal{W}^i y^i\left(1 - \frac{\Delta tk}{\zeta}\right)}{\Delta t}\right\rangle \\
&= \lim_{\Delta t\to 0}\left\langle \frac{-\left(y^i\right)^2\frac{2\Delta tk}{\zeta} + \frac{\nu}{\zeta^2}\Delta^2\mathcal{W}^i}{\Delta t}\right\rangle,
\end{aligned} \tag{B.5}$$

where we expoited in the last transformation step that the Wiener increments are independent on the position y and both $\langle y\rangle = 0$ and $\langle\Delta\mathcal{W}^i\rangle = 0$ because of the symmetry of the problem and the Wiener process. Also we eliminated higher order terms of Δt, recalling that the Wiener increments are well-known from stochastic analysis to satiyfy $\langle\Delta^2\mathcal{W}\rangle = \Delta t$. For this reason and by means of requirement (I), we can transform (B.5) into

$$0 = -2k_BT + \frac{\nu}{\zeta} \tag{B.6}$$

and therefore

$$\nu = 2k_BT\zeta. \tag{B.7}$$

Recalling (B.1), this means that the variance of the stochastic force linearly depends on the damping coefficient ζ with a prefactor $2k_BT$. This is actually the typical way, the fluctuation-dissipation theorem is written in the context of Brownian dynamics. The above consideration can easily be generalized to systems with more than one degree of freedom. In that case y becomes a vector and ζ a damping matrix. It is interesting to see that the stochastic force depends on the viscous damping constant, but not on the elastic spring constant. Physically, this result can easily be understood: the stochastic excitation of a particle is a consequence of thermal fluctuations in the surrounding bath. These fluctuations are not expected to depend on whether the particle is tethered by a spring somewhere. There are only three major differences between the example considered in this appendix and the case considered in section 3.1.4: first, in this appendix only a scalar system is considered, second, its elasticity is characterized by a simple spring constant rather than by the equation of an elastic continuum, and third, in this appendix a point-shaped particle is considered instead of a continuum. The first two differences are only of minor importance as the considerations in this appendix can easily be generalized to higher dimensions, and the elastic properties of the system obviously do not matter anyway. As to the third difference, one has to realize that the particle dealt with in this appendix is comparable to a point in the continuum considered in section 3.1.4. Therefore the stochastic line loads in section 3.1.4 can be computed by the multidimensional version of (B.1) by simply adding an additional Dirac-function making sure the independence of the line load at different points in the continuum. It is worth mentioning that the fluctuation-dissipation theorem forms the basis for the description of the diffusion of a particle in a thermal bath as shown in appendix B.1.2.

In the end of this section, it is again emphasized that the above considerations should only be taken as a brief examplification of the fluctuation-dissipation theorem rather than a rigorous proof. For a rigorous and more general derivation the reader is referred to standard textbooks on statistical physics.

B.1.2 General concept of diffusion

Let the configuration of some object, which we will refer to as particle in the following, be described by a vector $\boldsymbol{y} \in \mathbb{R}^m$ with m independent components. The particle is immersed into a thermal bath at termperature T, and the friction coefficient for its i-th degree of freedom is ζ_i. All external forces as well as the fluid velocity field are assumed to be zero so that the particle motion is governed only by the viscous damping and stochastic excitation of the thermal bath. According to the laws of statistical mechanics [32] the particle's equation of motion is under these conditions given componentwise by

$$y_i = \sqrt{\frac{2k_B T}{\zeta_i}} \mathcal{W}_i \tag{B.8}$$

where $\boldsymbol{\mathcal{W}}$ is an m-dimensional Wiener process, and $\mathcal{W}_i$ its i-th component. Note that (B.8) directly follows from (B.3) in appendix B.1.1 for the special case of a non-tethered particle, i.e., $k = 0$ in (B.3), by integrating equation (B.3) in time.

The motion described by (B.8) is usually referred to as diffusion. It describes a stochastic motion, which makes initial concentration peaks around a certain point in space in a swarm of particles governed by this equation of motion dissolve over time by spreading out the particles stochastically in the configuration space ('diffundere', Latin for 'spread out'). Diffusion can be characterized by a so-called diffusion constant D. It is the ratio between the mean square distance $\Delta^2_{t_D} y$ an ensemble of particles will cover in the span on time t_D divided by t_D, a factor of two and the number of dimensions m:

$$D = \frac{\langle \Delta_{t_D}^2 y \rangle}{2mt_D} = \frac{k_B T}{m} \sum_{i=1}^{m} \zeta_i^{-1}. \tag{B.9}$$

The normalization factor m makes sure that the diffusion constant remains the same regardless whether one single degree of freedom is considered or several identical ones. This way, the diffusion constant is independent on the number of dimensions itself, but rather depends only the average friction the particle is experiencing in the considered degrees of freedom. The second transformation step in (B.9) is possible, because the Wiener process $\mathcal{W}(t)$ satisfies by definition $\mathcal{W}(t_D) \otimes \mathcal{W}(t_D) = t_D \mathbf{1}$, where $\mathbf{1}$ is an $m \times m$ identity matrix.

B.1.3 Diffusion of rod-like particles

In this section, we consider the diffusion of straight, rigid, rod-like particles with circular cross section in m_t dimensions. For such particles, a translation of the center over a distance $\Delta_{t_D} x_c$, a rotation about their own axis by an angle $\Delta_{t_D} \theta_{c\|}$, and a rotation orthogonal to their own axis by an angle $\Delta_{t_D} \theta_{c\perp}$ happen independently, and thus also the respective diffusion processes. It is emphasized that the said increments can be superimposed commutatively to one and the same total motion so that they can be determined uniquely if the position at the beginning and at the end of the span on time t_D are known. It is worth mentioning that $\Delta_{t_D} \theta_{c\|}$ and $\Delta_{t_D} \theta_{c\perp}$ can be imagined similarly to the velocities illustrated in Fig. 3.2.

The diffusion coefficients for translation and rotation orthogonal to the rod axis can be defined with (B.9) in $m_t \in \{2; 3\}$ dimensions immediately as

$$D_t = \frac{\langle \Delta_{t_D}^2 x_c \rangle}{2m_t t_D}, \tag{B.10a}$$

$$D_{r\perp} = \frac{\langle \Delta_{t_D}^2 \theta_{c\perp} \rangle}{2(m_t - 1)t_D}. \tag{B.10b}$$

A rotation about the rod axis itself can happen only in three dimensions and there the respective diffusion coefficient is defined as

$$D_{r\|} = \frac{\langle \Delta_{t_D}^2 \theta_{c\|} \rangle}{2t_D}. \tag{B.10c}$$

Note that rotation orthogonal to the rod axis happens always in $(m_t - 1)$ degrees of freedom, which has to be accounted for by the factor $(m_t - 1)$ in the denominator. Defining friction coefficients $\zeta_{t\|}$, $\zeta_{t\perp}$, $\zeta_{r\|}$ and $\zeta_{r\perp}$ for translation parallel and orthogonal to the rod axis as well as rotation about and orthogonal to the rod axis (as also used in (3.16)), (B.10) can be transformed using (B.9) to

$$D_t = \frac{k_B T}{m_t} \left(\frac{1}{\zeta_{t\|}} + \frac{m_t - 1}{\zeta_{t\perp}} \right), \tag{B.11a}$$

$$D_{r\perp} = \frac{k_B T}{\zeta_{r\perp}}, \tag{B.11b}$$

$$D_{r\|} = \frac{k_B T}{\zeta_{r\|}}. \tag{B.11c}$$

The formulae (B.11) are special cases of the so-called Einstein relationship which says that diffusion coefficients can be computed in general as the ratio of the thermal energy k_BT and the effective friction coefficient.

For distinguishing in this thesis between diffusion coefficients in two and three dimensions, the indices '$3D$' for three dimensions and '$2D$' for two dimensions are used, e.g., in $D_{3D,r\perp}$ and $D_{2D,r\perp}$.

B.1.4 Computation of diffusion coefficients of rod-like particles

Diffusion coefficients can be determined in various ways, especially by experiments, analytical analysis or computer simulations. For a particle of length L and diameter d embedded into a fluid of viscosity η and temperature T, the diffusion coefficients can be computed with the Boltzmann constant k_B according to [75] in three dimensions by

$$D_{3D,t} = \frac{1}{3}\frac{k_BT\,[\ln(L/d) + 0.312 + 0.565/(L/d) - 0.1/(L/d)^2]}{\pi\eta L}, \tag{B.12a}$$

$$D_{3D,r\perp} = 3\frac{k_BT\,[\ln(L/d) - 0.662 + 0.917/(L/d) - 0.05/(L/d)^2]}{\pi\eta L^3}, \tag{B.12b}$$

$$D_{3D,r\parallel} = \frac{4k_BT(L/d)^2}{3.84\pi\eta L^3(1 + 0.677/(L/d) - 0.183/(L/d)^2)}. \tag{B.12c}$$

In two dimensions diffusion coefficients are given according to [62] by

$$D_{2D,t} = \frac{k_BT\,[3ln(L/d) + 0.658]}{8\pi\eta L} \tag{B.13a}$$

$$D_{2D,r\perp} = \frac{3k_BT\,[ln(L/d) - 0.447]}{\pi\eta L^3}. \tag{B.13b}$$

B.2 Relation between dihedral torsion and Frenet-Serret torsion

In this appendix the relation between dihedral torsion and Frenet-Serret torsion is discussed. Dihedral torsion is often employed in MD simulations in order to measure torsion in molecules whereas Frenet-Serret torsion is predominantly used in differential geometry in order to characterize smooth curves. We consider a curve $\boldsymbol{x}(\xi)$ of length L in $\mathbb{R}^3$ with curve parameter $\xi \in [0; L]$, which is discretized by n_n nodes $\xi^{[k]} := k\Delta\xi, k \in \{1, \dots, n_n\}$ in the parameter space with $\Delta\xi = L/(n_n - 1)$. These nodes correspond to nodes $\boldsymbol{x}^{[k]} := \boldsymbol{x}(k\Delta\xi), k \in \{1, \dots, n_n\}$ in the physical space. If no three successive nodes in the discretization are colinear, we can define the so-called dihedral angle $\psi^{[k]}$ at all nodes $\boldsymbol{x}^{[k]}, 2 \leq k \leq n_n - 3$ as

$$\psi^{[k]} = \arccos\frac{[(\boldsymbol{x}_{k+2} - \boldsymbol{x}_{k+1})\times(\boldsymbol{x}_{k+3} - \boldsymbol{x}_{k+2})]\cdot[(\boldsymbol{x}_k - \boldsymbol{x}_{k-1})\times(\boldsymbol{x}_{k+1} - \boldsymbol{x}_k)]}{|(\boldsymbol{x}_{k+2} - \boldsymbol{x}_{k+1})\times(\boldsymbol{x}_{k+3} - \boldsymbol{x}_{k+2})|\,|(\boldsymbol{x}_k - \boldsymbol{x}_{k-1})\times(\boldsymbol{x}_{k+1} - \boldsymbol{x}_k)|}. \tag{B.14}$$

The dihedral torsion at $\boldsymbol{x}^{[k]}$ is defined as

$$\tau_D^{[k]} = \frac{\psi^{[k]}}{\Delta\xi}. \tag{B.15}$$

We assume in the following that the Frenet-Serret torsion is properly defined at all points of the curve by

$$\tau_{FS}(\xi) = \frac{\det\left(\boldsymbol{x}'(\xi), \boldsymbol{x}''(\xi), \boldsymbol{x}'''(\xi)\right)}{|\boldsymbol{x}'(\xi) \times \boldsymbol{x}''(\xi)|^2}. \tag{B.16}$$

This means $|\boldsymbol{x}'(\xi) \times \boldsymbol{x}''(\xi)| > 0$ and thus $|\boldsymbol{x}'(\xi)| > 0$ and $|\boldsymbol{x}''(\xi)| > 0$ for all $\xi \in [0; L]$. Hence in a discretization with $\Delta\xi \rightarrow 0$ no three successive nodes are colinear, and the dihedral torsion is given at all nodes $\boldsymbol{x}^{[k]}, 2 \leq k \leq n_n - 3$ by

$$\tau_D^{[k]} = \lim_{\Delta\xi \rightarrow 0} \frac{\psi^{[k]}}{\Delta\xi}. \tag{B.17}$$

Equation (B.17) can be simplified in two steps. First, $\psi^{[k]}$ can be expressed by (B.14), and the argument of the $\arccos$-function in (B.14) can be approximated in terms of $\boldsymbol{x}(k\Delta\xi)$, $\boldsymbol{x}'(k\Delta\xi)$, $\boldsymbol{x}''(k\Delta\xi)$ and $\boldsymbol{x}'''(k\Delta\xi)$ neglecting higher order terms of the Taylor expansion. Second, the function $\arccos(y), y \in \mathbb{R}$ can be expressed by the series

$$\arccos(y) = \frac{\pi}{2} - \sum_{n=0}^{\infty} \frac{(2n-1)!!}{2n!!} \frac{y^{2n+1}}{2n+1}. \tag{B.18}$$

After lengthy calculations, these two steps allow for rewriting (B.17) as

$$\tau_D^{[k]} = \frac{|\boldsymbol{x}'(\xi)|^2 \det\left(\boldsymbol{x}'(\xi), \boldsymbol{x}''(\xi), \boldsymbol{x}'''(\xi)\right)}{|\boldsymbol{x}'(\xi) \times \boldsymbol{x}''(\xi)|^2} + O(\Delta\xi^2) = |\boldsymbol{x}'(\xi)|^2 \tau_{FS}(k\Delta\xi) + O(\Delta\xi^2). \tag{B.19}$$

Thus the dihedral torsion is a discrete linear approximation of the Frenet-Serret torsion if the axial strain of the curve is zero. The latter condition is often approximately (but almost never exactly) satisfied for rod-like continua with high slenderness ratio as there the axial stiffness is usually much larger than the bending stiffness. In that sense, the dihedral torsion may be considered a geometrically inexact linear approximation of the Frenet-Serret torsion.

C Simulation parameters for certain biopolymers and rod-like particles

In this appendix, numerical parameters for the simulation of certain rod-like structures are provided in Table C.1 and C.2, and a brief discussion where these parameters are taken from is included. All numerical values are given in terms of the basis units micrometer, second, miligram and Kelvin. The Poisson ratio ν may be chosen heuristically, because on the one hand to the authors' knowledge no experimental data is available from which it could be concluded, and on the other hand no significant shear deformation and thus no significant influence of the Poisson ratio is expected for the rod-like structures considered in this appendix. For the computation of the geometric parameters a circular cross section is assumed, which is not exactly true for, e.g., DNA or TMV, but a sufficient approximation for the scope of this thesis.

DNA: the strand diameter of DNA is well-known to be $2\text{e}{-3}$ and the length of a single base pair to be $3.4\text{e}{-4}$. This allows for computing the moment of inertia of area and the polar moment of inertia of area and the length of a DNA segment with a certain number of base pairs (bp). Then Young's modulus can be concluded from the persistence length provided in [92]. The friction coefficients of DNA can be computed with (3.25) and (B.12).

TMV: diameter, length and Young's modulus of TMV are taken from [20, 34]. Cross section, moment of inertia of area and polar moment of inertia of area are computed from the diameter assuming a circular cross section. The friction coefficients of TMV can be computed with (3.25) and (B.12).

Actin: actin filaments are usually employed either alone, stabilized with phalloidin, as combination actin-tropomyosin or as actin-tropomyosin stabilized with phalloidin. The cross section of pure actin is according to [46] given by $A = 1.9\text{e}{-5}$. Phalloidin is assumed not to change the geometry (cross section, moment of inertia of area), whereas tropomyosin is supposed to increase the cross section by a factor of 1.22 [46]. Assuming a circular cross section, this enables a direct computation of the moments of interia of area. Young's modulus for actin-phalloidin can be computed from this data and the persistence length 16.1 given in [37]. For all other cases Young's modulus can be adopted from [46]. As actin filaments of various lengths are used in practice, friction coefficients provided in this appendix are computed according to (3.20) and (3.26), i.e., without length dependent correction terms. Poisson's ratio is chosen heuristically in all simulations in the interval $[0.3; 0.5]$. No perceptible difference in the results could be found for different values from this interval.

type	d	L	A	J_2, J_3	J_r
DNA 12bp	$2.0\text{e}{-3}$	$4.1\text{e}{-3}$	$3.1\text{e}{-6}$	$7.9\text{e}{-13}$	$1.6\text{e}{-12}$
DNA 20bp	$2.0\text{e}{-3}$	$6.8\text{e}{-3}$	$3.1\text{e}{-6}$	$7.9\text{e}{-13}$	$1.6\text{e}{-12}$
TMV	$1.8\text{e}{-2}$	$3.0\text{e}{-1}$	$2.5\text{e}{-4}$	$5.2\text{e}{-9}$	$1.0\text{e}{-8}$
actin alone	$4.9\text{e}{-3}$	–	$1.9\text{e}{-5}$	$2.8\text{e}{-11}$	$5.7\text{e}{-11}$
actin with phalloidin	$4.9\text{e}{-3}$	–	$1.9\text{e}{-5}$	$2.8\text{e}{-11}$	$5.7\text{e}{-11}$
actin-tropomyosin	$5.4\text{e}{-3}$	–	$2.3\text{e}{-5}$	$4.2\text{e}{-11}$	$8.3\text{e}{-11}$
actin-tropomyosin with phalloidin	$5.4\text{e}{-3}$	–	$2.3\text{e}{-5}$	$4.2\text{e}{-11}$	$8.3\text{e}{-11}$

Table C.1: Numerical parameters of the geometry of different rod-like microstructures

type	E	ν	$\gamma_{t\perp}$	$\gamma_{t\|}$	$\gamma_{r\perp}$	$\gamma_{r\|}$
DNA 12bp	0.2e9	0.5	$2.56\text{e}{-2}$	$3.03\text{e}{-3}$	0	$1.55\text{e}{-8}$
DNA 20bp	0.2e9	0.5	$1.52\text{e}{-2}$	$2.45\text{e}{-3}$	0	$1.42\text{e}{-8}$
TMV	1.1e9	0.5	$5.70\text{e}{-3}$	$1.53\text{e}{-3}$	0	$1.62\text{e}{-6}$
actin alone	1.3e9	$[0.3; 0.5]$	$1.26\text{e}{-2}$	$6.28\text{e}{-3}$	0	$7.57\text{e}{-8}$
actin with phalloidin	2.3e9	$[0.3; 0.5]$	$1.26\text{e}{-2}$	$6.28\text{e}{-3}$	0	$7.57\text{e}{-8}$
actin-tropomyosin	2.0e9	$[0.3; 0.5]$	$1.26\text{e}{-2}$	$6.28\text{e}{-3}$	0	$9.20\text{e}{-8}$
actin-tropomysoin with phalloidin	2.8e9	$[0.3; 0.5]$	$1.26\text{e}{-2}$	$6.28\text{e}{-3}$	0	$9.20\text{e}{-8}$

Table C.2: Numerical parameters of the elasticity and hydrodynamics of different rod-like microstructures, where a fluid viscosity $\eta = 1\text{e}{-3}$ is assumed

Bibliography

[1] J.A. Åström, P.B.S. Kumar, *Strain hardening, avalanches, and strain softening in dense cross-linked actin networks*, Phys. Rev. E **77** (2008) 051913.

[2] R. Adami, D. Choquet, E. Grazi, *Rhodamine phalloidin f-actin*, European Journal of Biochemistry **263** (1999) 270–275.

[3] E.J. Allen, S.J. Novosel, Z. Zhang, *Finite element and difference approximation of some linear stochastic partial differential equations*, Stochastics and Stochastic Reports **64** (1998) 117–142.

[4] S. Allison, R. Austin, M. Hogan, *Bending and twisting dynamics of short linear dnas. analysis of the triplet anisotropy decay of a 209 base pair fragment by brownian simulation*, J. Chem. Phys. **90** (1989) 3843–3854.

[5] M. Arroyo, M. Ortiz, *Local maximum-entropy approximation schemes: a seamless bridge between finite elements and meshfree methods*, Int J Numer Meth Eng **65** (2005) 2167–2202.

[6] A.R. Bausch, Technische Universität München, images provided by and presented with kind permission of.

[7] J.R. Blundell, E.M. Terentjev, *The influence of disorder on deformations in semi-flexible networks*, Proc R Soc A (2011) rspa.2010.0600v1–rspa20100600.

[8] I. Borukhov, R. Bruinsma, *Raft instability of biopolymer gels.*, Phys Rev Lett **87** (2001) 158101.

[9] I. Borukhov, R.F. Bruinsma, W.M. Gelbart, A.J. Liu, *Structural polymorphism of the cytoskeleton: A model of linker-assisted filament aggregation*, PNAS **102** (2005) 3673–3678.

[10] R. Buckdahn, E. Pardoux, *Monotonicity methods for white noise driven quasilinear spdes*, Progress in Probability **22** (1990) 219.

[11] M. Bulacu, E. van der Giessen, *Effect of bending and torsion rigidity on self-diffusion in polymer melts: A molecular-dynamics study*, J. Chem. Phys. **123** (2005) 114901–13.

[12] C. Bustamante, S.B. Smith, J. Liphardt, D. Smith, *Single-molecule studies of dna mechanics*, Current Opinion in Structural Biology **10** (2000) 279–285.

[13] L. CASTELLANI, G. OFFER, A. ELLIOTT, E.J. O'BRIEN, *Structure of filamin and the f-actin-heavy merofilamin complex*, Journal of Muscle Research and Cell Motility **2** (1981) 193–202.

[14] P.L. CHANDRAN, M.R.K. MOFRAD, *Rods-on-string idealization captures semiflexible filament dynamics*, Phys. Rev. E **79** (2009) 011906.

[15] P.L. CHANDRAN, M.R.K. MOFRAD, *Averaged implicit hydrodynamic model of semiflexible filaments*, Phys. Rev. E **81** (2010) 031920.

[16] G. CHIRICO, *Torsional-bending infinitesimal dynamics of a dna chain*, Biopolymers **38** (1996) 801–811.

[17] G. CHIRICO, J. LANGOWSKI, *Kinetics of dna supercoiling studied by brownian dynamics simulation*, Biopolymers **34** (1994) 415–433.

[18] J.A. COTTRELLI, T.J.R. HUGHES, Y. BAZILEVES, *Isogeometric analysis: toward integration of CAD and FEA*, John Wiley and Sons, 2009.

[19] D.S. COURSON, R.S. ROCK, *Actin crosslink assembly and disassembly mechanics for alpha-actinin and fascin*, Journal of Biological Chemistry **285** (2010) 26350–26357.

[20] A.N. CREAGER, K.B.G. SCHOLTHOF, V. CITOVSKY, H.B. SCHOLTHOF, *Tobacco mosaic virus: Pioneering research for a century*, Plant Cell **11** (1999) 301–308.

[21] M.A. CRISFIELD, *Non-linear Finite Element Analysis of Solids and Structures, Volume 1: Essentials*, John Wiley & Sons, Chichester, 2003.

[22] M.A. CRISFIELD, *Non-linear Finite Element Analysis of Solids and Structures, Volume 2: Advanced Topics*, Wiley, Chichester, 2003.

[23] M.A. CRISFIELD, G. JELENIC, *Objectivity of strain measures in the geometrically exact three-dimensional beam theory and its finite-element implementation*, Proceedings of the Royal Society of London. Series A: Mathematical, Physical and Engineering Sciences **455** (1999) 1125–1147.

[24] C. CYRON, K. NISSEN, V. GRAVEMEIER, W. WALL, *Stable meshfree methods in fluid mechanics based on green's functions*, Computational Mechanics **46** (2010) 287 – 300.

[25] C.J. CYRON, M. ARROYO, M. ORTIZ, *Smooth, second order, non-negative meshfree approximants selected by maximum entropy*, Int J Numer Meth Eng **79** (2009) 1605–1632.

[26] C.J. CYRON, K.W. MÜLLER, O. LIELEG, A.R. BAUSCH, W.A. WALL, *Micromechanical simulations of biopolymer networks with finite elements*, J. Comput. Phys. **(submitted)**.

[27] C.J. CYRON, K. NISSEN, V. GRAVEMEIER, W.A. WALL, *Information flux maximum-entropy approximation schemes for convection-diffusion problems*, Int. J. Numer. Meth. Fluids **64** (2010) 1180–1200.

[28] C.J. CYRON, W.A. WALL, *Finite-element approach to brownian dynamics of polymers*, Phys. Rev. E **80** (2009) 066704–.

[29] C.J. CYRON, W.A. WALL, *Consistent finite element approach to brownian polymer dynamics with anisotropic friction*, Phys. Rev. E **82** (2010) 066705–.

[30] C.J. CYRON, W.A. WALL, *Numerical method for the simulation of the brownian dynamics of rod-like microstructures with three dimensional nonlinear beam elements*, Int J Numer Meth Eng **(accepted)**.

[31] J.M. DEUTSCH, *Internal dissipation of a polymer*, Phys. Rev. E **81** (2010) 061804.

[32] M. DOI, S.F. EDWARDS, *The theory of polymer dynamics*, Clarendon Press, Oxford, 1994.

[33] D.L. ERMAK, J.A. MCCAMMON, *Brownian dynamics with hydrodynamic interactions*, J. Chem. Phys. **69** (1978) 1352–1360.

[34] M. FALVO, S. WASHBURN, R. SUPERFINE, M. FINCH, F. BROOKS, V. CHI, R. TAYLOR, *Manipulation of individual viruses: friction and mechanical properties.*, Biophys J **72** (1997) 1396–403.

[35] M. FIXMAN, *Implicit algorithm for brownian dynamics of polymers*, Macromolecules **19** (1986) 1195–1204.

[36] M.W. GEE, C.T. KELLEY, R.B. LEHOUCQ, *Pseudo-transient continuation for nonlinear transient elasticity*, Int J Numer Meth Eng **78** (2009) 1209–1219.

[37] L.L. GOFF, O. HALLATSCHEK, E. FREY, F. AMBLARD, *Tracer studies on f-actin fluctuations*, Phys. Rev. Lett. **89** (2002) 258101.

[38] W. GOLDMANN, G. ISENBERG, *Analysis of filamin and [alpha]-actinin binding to actin by the stopped flow method*, FEBS Letters **336** (1993) 408–410.

[39] J. GOLJI, R. COLLINS, M.R.K. MOFRAD, *Molecular mechanics of the α-actinin rod domain: Bending, torsional, and extensional behavior*, PLoS Comput Biol **5** (2009) e1000389.

[40] P.S. GRASSIA, E.J. HINCH, L.C. NITSCHE, *Computer simulations of brownian motion of complex systems*, Journal of Fluid Mechanics **282** (1995) 373–403.

[41] O. HALLATSCHEK, *Semiflexible polymer dynamics*, Shaker Verlag, Aachen, 2004.

[42] O. HALLATSCHEK, E. FREY, K. KROY, *Tension dynamics in semiflexible polymers. i. coarse-grained equations of motion*, Phys. Rev. E **75** (2007) 031905–14.

[43] E.H. HAUGE, A. MARTIN-LÖF, *Fluctuating hydrodynamics and brownian motion*, Journal of Statistical Physics **7** (1973) 259–281.

[44] C. HEUSSINGER, E. FREY, *Force distributions and force chains in random stiff fiber networks*, The European Physical Journal E - Soft Matter **24** (2007) 47–53.

[45] M. HOSEK, J.X. TANG, *Polymer-induced bundling of f actin and the depletion force*, Phys. Rev. E **69** (2004) 051907.

[46] J. HOWARD, *Mechanics of Motor Proteins and the Cytoskeleton*, Sinauer Associates, Sunderland, 2001.

[47] T.J.R. HUGHES, *Finite Element Method - Linear Static and Dynamic Finite Element Analysis*, Prentice Hall, Englewood Cliffs, 2000.

[48] E.M. HUISMAN, C. STORM, G.T. BARKEMA, *Frequency-dependent stiffening of semiflexible networks: A dynamical nonaffine to affine transition*, Phys. Rev. E **82** (2010) 061902.

[49] E.M. HUISMAN, T. VAN DILLEN, P.R. ONCK, E. VAN DER GIESSEN, *Three-dimensional cross-linked f-actin networks: Relation between network architecture and mechanical behavior*, Phys. Rev. Lett. **99** (2007) 208103–4.

[50] G. JELENIC, M.A. CRISFIELD, *Geometrically exact 3d beam theory: implementation of a strain-invariant finite element for statics and dynamics*, Comput. methods Appl. Mech. Engrg **171** (1999) 141–171.

[51] D.A. KESSLER, Y. RABIN, *Effect of curvature and twist on the conformations of a fluctuating ribbon*, J. Chem. Phys. **118** (2003) 897–904.

[52] J.M. KIM, P.S. DOYLE, *A brownian dynamics-finite element method for simulating dna electrophoresis in nonhomogeneous electric fields*, The Journal of Chemical Physics **125** (2006) 074906.

[53] J.M. KIM, P.S. DOYLE, *Design and numerical simulation of a dna electrophoretic stretching device.*, Lab on a Chip **7** (2007) 213–225.

[54] T. KIM, W. HWANG, R. KAMM, *Computational analysis of a cross-linked actin-like network*, Experimental Mechanics **49** (2009) 91–104.

[55] T. KIM, W. HWANG, H. LEE, R.D. KAMM, *Computational analysis of viscoelastic properties of crosslinked actin networks*, PLoS Comput Biol **5** (2009) e1000439.

[56] P.E. KLOEDEN, *Numerical Solution of SDE Through Computer Experiments*, Springer, Berlin, 2003.

[57] P.E. KLOEDEN, E. PLATEN, *Numerical Solution of Stochastic Differential Equations*, Springer, Berlin, 1999.

[58] K.S. KOLAHI, M.R. MOFRAD, *Molecular mechanics of filamin's rod domain*, Biophys J **94** (2008) 1075–1083.

[59] R. KUPFERMAN, G.A. PAVLIOTIS, A.M. STUART, *Ito versus stratonovich white-noise limits for systems with inertia and colored multiplicative noise*, Phys. Rev. E **70** (2004) 036120.

[60] P. Lançon, G. Batrouni, L. Lobry, N. Ostrowsky, *Drift without flux: Brownian walker with a space-dependent diffusion coefficient*, Europhysics Letters **54** (2001) 28–34.

[61] A.W.C. Lau, T.C. Lubensky, *State-dependent diffusion: Thermodynamic consistency and its path integral formulation*, Phys. Rev. E **76** (2007) 011123.

[62] G. Li, J.X. Tang, *Diffusion of actin filaments within a thin layer between two walls*, Phys. Rev. E **69** (2004) 061921.

[63] O. Lieleg, M.M.A.E. Claessens, A.R. Bausch, *Structure and dynamics of cross-linked actin networks*, Soft Matter **6** (2010) 218–225.

[64] O. Lieleg, M.M.A.E. Claessens, C. Heussinger, E. Frey, A.R. Bausch, *Mechanics of bundled semiflexible polymer networks*, Phys. Rev. Lett. **99** (2007) 088102, http://prl.aps.org/abstract/PRL/v99/i8/e088102, *as regards images reprinted from this article, readers may view, browse, and/or download material for temporary copying purposes only, provided these uses are for noncommercial personal purposes. Except as provided by law, this material may not be further reproduced, distributed, transmitted, modified, adapted, performed, displayed, published, or sold in whole or part, without prior written permission from the American Phyiscal Society.*

[65] O. Lieleg, M.M.A.E. Claessens, Y. Luan, A.R. Bausch, *Transient binding and dissipation in cross-linked actin networks*, Phys. Rev. Lett. **101** (2008) 108101.

[66] O. Lieleg, K.M. Schmoller, C.J. Cyron, Y. Luan, W.A. Wall, A.R. Bausch, *Structural polymorphism in heterogeneous cytoskeletal networks.*, Soft Matter **5** (2009) 1796–1803.

[67] O. Lieleg, I. Vladescu, K. Ribbeck, *Characterization of particle translocation through mucin hydrogels*, Biophys J **98** (2010) 1782–1789.

[68] X. Liu, G.H. Pollack, *Mechanics of f-actin characterized with microfabricated cantilevers*, Biophys J **83** (2002) 2705–2715.

[69] S.B. Marston, *The rates of formation and dissociation of actin-myosin complexes. effects of solvent, temperature, nucleotide binding and head-head interactions.*, Biochem. J. **203** (1982) 453–460.

[70] M. Matsuo, S.i. Sasa, *Stochastic energetics of non-uniform temperature systems*, Physica A: Statistical Mechanics and its Applications **276** (2000) 188–200.

[71] R. Meyer, U. Aebi, *Bundling of actin filaments by alpha-actinin depends on its molecular length.*, J Cell Biol **110** (1990) 2013–24.

[72] A. Montesi, D. Morse, M. Pasquali, J. Chem. Phys. **122** (2005) 084903.

[73] T. Nishizaka, R. Seo, H. Tadakuma, K. Kinosita, S. Ishiwata, *Characterization of single actomyosin rigor bonds: Load dependence of lifetime and mechanical properties*, Biophys J **79** (2000) 962–974.

[74] P.R. Onck, T. Koeman, T. van Dillen, E. van der Giessen, *Alternative explanation of stiffening in cross-linked semiflexible networks*, Phys. Rev. Lett. **95** (2005) 178102.

[75] A. Ortega, J.G. de la Torre, *Hydrodynamic properties of rodlike and disklike particles in dilute solution*, J. Chem. Phys. **119** (2003) 9914–9919.

[76] J.S. Palmer, M.C. Boyce, *Constitutive modeling of the stress-strain behavior of f-actin filament networks*, Acta Biomaterialia **4** (2008) 597–612.

[77] I. Romero, *The interpolation of rotations and its application to finite element models of geometrically exact rods*, Computational Mechanics **34** (2004) 121–133.

[78] A. Rössler, *Second order runge–kutta methods for itō stochastic differential equations*, SIAM J. Numer. Anal. **47** (2009) 1713–1738.

[79] J. Rotne, S. Prager, *Variational treatment of hydrodynamic interaction in polymers*, J. Chem. Phys. **50** (1969) 4831–4837.

[80] V. Schaller, C. Weber, C. Semmrich, E. Frey, A.R. Bausch, *Polar patterns of driven filaments*, Nature **467** (2010) 73–77.

[81] K. Sekimoto, *Temporal coarse graining for systems of brownian particles with non-constant temperature*, Journal of the Physical Society of Japan **68** (1999) 1448–1449.

[82] H. Shin, K.R.P. Drew, J.R. Bartles, G.C.L. Wong, G.M. Grason, *Cooperativity and frustration in protein-mediated parallel actin bundles*, Phys. Rev. Lett. **103** (2009) 238102.

[83] J.C. Simo, L. Vu-Quoc, *A three dimensional finite strain rod model part ii: Computational aspects*, Comput. methods Appl. Mech. Engrg **58** (1986) 79–116.

[84] J.C. Simo, L. Vu-Quoc, *On the dynamics in space of rods undergoing large motions – a geometrically exact approach*, Comput. methods Appl. Mech. Engrg **66** (1988) 125–161.

[85] A.J. Spakowitz, *Wormlike chain statistics with twist and fixed ends*, EPL (Europhysics Letters) **73** (2006) 684.

[86] R. Tharmann, *Mechanical properties of complex cytoskeleton networks*, Ph.D. thesis, Technische Universität München (2007).

[87] T. Tian, K. Burrage, *Implicit taylor methods for stiff stochastic differential equations*, Applied Numerical Mathematics **38** (2001) 167–185.

[88] M. Toda, R. Kubo, N. Saito, *Statistical physics I: equilibrium statistical mechanics*, Springer, Berlin, 1983.

[89] M. Toda, R. Kubo, N. Saito, *Statistical physics II: nonequilibrium statistical mechanics*, Springer, Berlin, 1992.

[90] Y. TSUDA, H. YASUTAKE, A. ISHIJIMA, T. YANAGIDA, *Torsional rigidity of single actin filaments and actin–actin bond breaking force under torsion measured directly by in vitroÃćÂĂÂĽmicromanipulation*, PNAS **93** (1996) 12937–12942.

[91] J.B. WALSH, *Finite element methods for parabolic stochastic pde's*, Potential Analysis **23** (2005) 1–43.

[92] M. WANG, H. YIN, R. LANDICK, J. GELLES, S. BLOCK, *Stretching dna with optical tweezers*, Biophys J **72** (1997) 1335–1346.

[93] J. WILHELM, E. FREY, *Radial distribution function of semiflexible polymers*, Phys. Rev. Lett. **77** (1996) 2581 – 2584.

[94] G.C.L. WONG, J.X. TANG, A. LIN, Y. LI, P.A. JANMEY, C.R. SAFINYA, *Hierarchical self-assembly of f-actin and cationic lipid complexes: Stacked three-layer tubule networks*, Science **288** (2000) 2035–2039.

[95] P. WRIGGERS, *Computational Contact Mechanics*, Wiley, New York, 2002.

[96] R. YASUDA, H. MIYATA, K. KINOSITA, JR, *Direct measurement of the torsional rigidity of single actin filaments*, Journal of Molecular Biology **263** (1996) 227–236.